

Boron Nitride and Semiconducting Diamond; Interface Formation and Electronic States

by

Jesse M. Brown

A Dissertation Presented in Partial Fulfillment
of the Requirements for the degree
Doctor of Philosophy

Approved November 2021 by the
Graduate Supervisory Committee:

Robert Nemanich, Chair
Ricardo Alarcon
Stuart Lindsay
Anna Zaniewski

ARIZONA STATE UNIVERSITY

December 2021

ABSTRACT

Cubic boron nitride (c-BN), hexagonal boron nitride (h-BN), and semiconducting diamond all have physical properties that make them ideal materials for applications in high power high frequency electronics, as well as radiation detectors. However, there is limited research on c-BN thin films and controlling the growth of c-BN or h-BN, as they both have unique and interesting properties. This dissertation focuses in part on the deposition of c-BN via plasma enhanced chemical vapor deposition (PECVD) on boron doped diamond. *In-Situ* X-ray photoelectron spectroscopy (XPS) is used to characterize the boron nitride thin films thickness and the ratio of h-BN to c-BN.

The effects of the hydrogen concentration during the deposition of boron nitride are investigated. The deposition rate of boron nitride is found to be proportional to the hydrogen gas flow. The sp^2 to sp^3 bonding is also found to be dependent on the Hydrogen gas flow. Preferential growth of h-BN is observed when an excess of hydrogen is supplied to the reaction, while h-BN growth is suppressed when hydrogen flow is reduced to be the limiting reactant. Reduced hydrogen flow is also observed to promote preferential growth of c-BN.

The limited hydrogen reaction is used to deposit c-BN on single crystal (100) boron-doped diamond substrates. *In-Situ* ultra-violet photoelectron spectroscopy (UPS) and XPS are used to deduce the valence band offset of the diamond/c-BN interface. A valence band offset of -0.3 eV is measured with the diamond VBM above the VBM of c-BN. This value is then discussed in context of previous experimental results and theoretical calculations.

Finally, UPS and XPS are used to characterize the surface states of phosphorus-doped diamond. Variations within the processing parameters for surface preparation and the effects on the electronic surface states are discussed.

DEDICATION

To the everlasting pursuit of knowledge.

As above, so below

ACKNOWLEDGEMENTS

Completing this PhD is the most difficult thing I have done yet. I would like to thank all the people who helped make this happen along this journey. Firstly, I would like to give my sincere gratitude to Dr. Robert J. Nemanich. Your excitement about science and tireless dedication to your lab and students was an inspiration for me. I greatly appreciated our physics discussions, as they always lead to a better understanding of the science. You dealt with my crazy and pushed me to be better than I thought I could, and I thank you for this.

I also want to thank my committee members, Dr. Ricardo Alarcon, Dr. Stuart Lindsey, Dr Anna Zaniewski. I greatly enjoyed the experiments that I was able to do with you all and appreciate the guidance you gave me during those experiments. I would also like to thank you for taking the time and effort of serving on my committee.

I would also like to whole heartedly thank Professor Gary Adams who first introduced me to Dr. Nemanich and gave me a helping hand when I was down in the gutters. You provided the foothold to launch myself toward any opportunity to be a scientist. I would also like to recognize Dr. Kate Ross who introduced me to crystal growth and inspired me to start this journey toward my PhD. Her brilliance and passion gave me a goal to strive to be the best, I'm still aiming to achieve a Nobel Prize in physics... only time will tell. A special thanks to Tucker Manton (soon to be Dr), you are an amazing person. We started our physics careers together and have had such an intertwining lifeline, and I am the better for it. You provided the handhold to launch

myself into the PhD program and now we are about to graduate together, how amazing is this!

To Dr. Danial Messina, working with you in the lab has been a great pleasure, and sharing in the pain of equipment troubles. You have been my comrade in science research. The late nights and fabulous homework solutions we did together made the weight of classes so much lighter, and more fun.

To my dear brother Jack, you have been my rock, my calming pool of water along this journey. You seriously kept me alive with your delicious food and kept me sane with your insightful words. Mom how can I even describe how you have made this all possible. In the immortal words, I love you. Dad I can't even put into words, but I know that you and I are one in the same now that you have passed to the other side.

To all my NSL Lab mates, Kevin Hatch, Avani Patel, Franz Koeck, Yu Yang, Xingyi Wang, Mei Hao, Robert Mechem, Kari Sloten Thank you all for your help with late night experiments, and many enjoyable discussions.

To my Roommates Dave Magenheim, Toshi Demonteroza, and Torrey Ray, thank you for making my life outside of school a blast, and thanks for listening to the ranting and raving of all the cool science I am privileged to contribute to.

Finally, I would like to acknowledge that the research presented in this dissertation is supported by The National Science Foundations (NSF) and Northrop Grumman., ARPA-e and the ULTRA project.

TABLE OF CONTENTS

	Page
LIST OF FIGURES	ix
CHAPTER	
1 INTRODUCTION	1
1.1 Objective and Outline.....	1
1.2 Boron Nitride History.....	2
1.3 Properties of Boron Nitride and Diamond	5
1.4 Current State of the Art Synthesis of Boron Nitride	9
2 INTRODUCTIONS TO EQUIPMENT AND EXPERIMENTS	11
2.1.1 Substrates for Electron Cyclotron Resonance Plasma Enhanced Chemical Vapor Deposition.....	11
2.1.2 Electron Cyclotron Resonance Plasma Enhanced Chemical Vapor Deposition (ECR PECVD).....	12
2.2 PHOTOELECTRON SPECTROSCOPY	17
2.2.1 Background and General Principles	17
2.2.2 Peak Broadening.....	19
2.2.3 Photoelectron Energy Loss.....	22

CHAPTER	Page
2.3 Photoelectron Spectroscopy System and Calibration.....	27
2.3.1 Monochromatic X-ray Source	27
2.3.2 Ultra-Violet Light Source.....	28
2.3.2 Calibration of Photoelectron Spectroscopy System	29
2.4 Surfaces and Interface Physics	31
2.4.1 Surface States	31
2.4.2 Band Bending	32
2.4.3 Valence Band Offset.....	34
 3 NUCLEATION OF CUBIC BORON NITRIDE ON POLYCRYSTALLINE BORON- DOPED DIAMOND VIA PLASMA ENHANCED CHEMICAL VAPOR DEPOSITION	 37
3.1 Abstract	37
3.2 Introduction	37
3.3 Experiment	41
3.4 Results	44
3.5 Discussion	50
3.6 Conclusion.....	54

CHAPTER	Page
4 VALENCE BAND OFFSET OF CUBIC BORON NITRIDE ON (100) BORON-DOPED DIAMOND.....	56
4.1 Abstract	56
4.2 Introduction	56
4.3 Experiment	60
4.4 Results	64
4.5 Discussion	76
4.6 Conclusion.....	79
5 ELECTRONIC SURFACE STATES OF PHOSPHORUS-DOPED DIAMOND	81
5.1 Abstract	81
5.2 Introduction	81
5.3 Experiment	83
5.4 Results	86
5.5 Discussion	88
5.6 Conclusion.....	90
6 SUMMARY AND FUTURE WORK	91
REFERENCES	96

List of Figures

Figure		Page
Figure 1	Number of publications per year on boron nitride compared to publications on cubic boron nitride.....	2
Figure 2	Physical properties and potential applications for diamond, and cubic boron nitride.....	6
Figure 3	Atomic orbital hybridization and molecular orbital bonding energy diagram for h-BN (top) and c-BN (bottom). The 2s and 2p orbitals have either sp^2 or sp^3 for hexagonal structure, and cubic structure respectively. The B 1s and N 1s core levels are ~191 eV and ~399 eV below fermi level. The core level shift between the two hybridizations is ~0.5 - 1 eV	7
Figure 4	Polycrystalline boron doped diamond substrates from Element Six.....	11
Figure 5	Schematic of ECR PECVD deposition chamber used to deposit boron nitride films	12
Figure 6	(Top) Magnetic field strength for a bottom magnet current of 128A and a top magnet current of 110A plotted along the central axial position of the chamber. The red line is positioned at 875G, which is the reported resonance with the microwave source. (Bottom) Corresponding magnetic field strength gradient, which is proportional to the force applied to charged particles.....	14

Figure	Page
Figure 7	Energy level diagram illustrates schematically the basic XPS equation including x-ray source energy ($h\nu$), the binding energy of the electron (E_B), the measured kinetic energy of the electron (E_K) and the work function of the spectrometer (Φ_{spec}). [26] 19
Figure 8	Relative intensity and energy resolution for the VG Scientia R3000 hemispherical analyzer. Each point represents a different pass energy and slit size combo, Relative intensity is calculated per unit of time. For future student reference 21
Figure 9	Universal IMFP curve. 22
Figure 10	(a) Schematic representation of photoelectron generation, and transport to surface. Electrons emitted without interaction, labeled (A) produce core level and auger peaks. Electrons which undergo at least one inelastic collision, labeled B, contribute to the background. Electrons which undergo multiple collisions and do not escape the sample are labeled C. 23
Figure 11	Shake up process for h-BN. The excitation of the host atom into the π^* state reduces the kinetic energy of the ejected 1s core electron by exactly the quantized energy difference between the excited state and the ground state. For h-BN this is equal to the band gap (~ 5.2 eV)..... 26
Figure 12	Schematic process of X-ray generation, monochromation, photoelectron generation, and electron analyzer for High Resolution XPS measurements.. 27
Figure 13	XPS calibration curves of clean gold surface. 29

Figure	Page	
Figure 14	E-beam deposited gold on silicon wafer after a hydrogen plasma cleaning. The blue lines denote the Fermi level and secondary electron cutoff (S_{cutoff}). The S_{cutoff} is used to calculate the work function. ($\Phi = 21.2 - 16.1 = 5.1 \text{ eV}$)	30
Figure 15	Simplified one-dimensional model of a periodic crystal potential terminating at an ideal surface. At the surface, the model potential jumps abruptly to the vacuum level (solid line). The dashed line represents a more realistic picture, where the potential reaches the vacuum level over some distance.....	31
Figure 16	Example of energy dispersion relation, with projected bulk bands and surface states. Surface states only exist in the k_{\parallel} direction	32
Figure 17	Schematic representation of downward band bending ($q \cdot V_{\text{BB}}$). The change in the core level and VBM at the surface can be measured with XPS and UPS.	34
Figure 18	Representation of the three-step process described above. The top black curves represent the clean substrate in step (1). The middle blue curves represent the core levels at the interface. The substrate core level shift to higher binding energies represents downward band bending at the interface. The red curves represent the thick overlayer in step (3). The overlayer shift in binding energies indicates there is upward band bending toward the interface. 	35
Figure 19	Energy band alignment diagram using the representative data in Figure 18. In this example, the substrate is p-type, and exhibits downward band bending,	

Figure	Page
	while the overlayer, which has a larger band gap than the substrate exhibits upward band bending toward the interface. The VBO is the discontinuous energy barrier between the substrate and the over layer, and in this example is a negative VBO, as the overlayer VBM is below the substrate VBM 36
Figure 20	An evolution of the N 1s, C1s and B1s core energy levels. The data has been normalized to the clean diamond peak intensity, and with the corresponding ASF to better view the relative concentration of each element. (i) Initial Hydrogen plasma cleaned boron doped diamond (a) 10 minutes with H ₂ = 0 sccm, followed by (b) 10 minutes with H ₂ = 4 sccm, followed by (c) 10 minutes with H ₂ = 0 sccm. Results show how hydrogen can be toggled to either grow or etch BN. 45
Figure 21	The Nitrogen, Carbon, and Boron 1s core level peaks for different H ₂ flow rates: (a) H ₂ = 1 sccm for 100 minutes (b) H ₂ = 2 sccm for 10 minutes (c) H ₂ = 3 sccm for 10 minutes (d) H ₂ = 4 sccm for 10 minutes. Showing that hydrogen can control the reaction rate. 46
Figure 22	Growth Rates, Thickness, and %-hBN as a function of hydrogen flow rates. Note the correlation between growth rate and %-h-BN..... 47
Figure 23	The B 1s core level (right) and enlarged π -plasmon energy loss peak spectrum (left) for BN deposition using limited H ₂ flow for (a) 30 minutes and (b) for 150 minutes and using excess H ₂ flow for (c) 10 minutes and (d) 40 minutes.

Figure	Page
	The deposition with a limited H ₂ flow results show a reduced π -plasmon energy loss peak..... 48
Figure 24	Example double carbon peak from (data from Figure 20 scan (a)). The C 1s core level energy from the hydrogen terminated surface (284.2 eV) and the C 1s core level energy from the nitrogen terminated diamond surface (285.2 eV). This non-uniform surface shows the difference in band bending between the nitrogen terminated and hydrogen terminated surfaces of diamond. The two small peaks to higher binding energy can be attributed to carbon nitrogen bonding near the surface..... 49
Figure 25	Model of hydrogen defect in c-BN nucleation for the (111) interface. The extra enthalpy causes the N—B bond to increase in length, changing the nearest neighbor bonding angle from isotropic 109° to anisotropic 119° and 94.5°. If excess hydrogen is used during the deposition an extra hydrogen may get trapped during the growth process. This may provide a nucleation point for h-BN..... 53
Figure 26	Schematic representation of the measured values to determine the electron affinity of a surface..... 67
Figure 27	Initial (100) boron-doped diamond substrates after Hydrogen termination process. The C 1s energy of 284.2 eV, and an NEA of -0.7 eV was repeatable for all initial substrates. 67
Figure 28	XPS of N1s C1s and B1s core levels, and VBM scan using He II α (40.8 eV). (a) Typical H-terminated boron-doped diamond (b) Nitrogen terminated

Figure	Page
surface (c) Nucleation of boron nitride. (d) Boron nitride ~1 nm thick, covering 70-80% of the diamond substrate (e) Boron nitride film ~ 6.7 nm thick (f) Thick boron nitride film (> 10 nm)	68
Figure 29 Valence band maximum measured with He II (40.8 eV), and work function measured with He I (21.2 eV), for (a) hydrogen terminated boron doped diamond, (b) Nitrogen terminated boron doped diamond. (c) Nucleation of BN (1 nm thick). (d) 6.7 nm of BN. (d) Thick layer (14-17 nm) of BN.	70
Figure 30 Energy level diagram of (left) hydrogen terminated boron-doped diamond, presented in Figure 28 scan (a) and Figure 29scan (a). (right) Nitrogen terminated boron-doped diamond presented in Figure 28 scan (b) and Figure 29 scan (b)	71
Figure 31 Energy band alignment of 1.1nm of c-BN on (100) single crystal boron-doped diamond. Derived from data presented in Figure 28 scan (d) Figure 29 scan (c).....	73
Figure 32 TEM of 1.1 nm of boron nitride on boron-doped diamond. Showing the nucleation of BN on the diamond surface, and the partial coverage of the substrate, also seen in the XPS peak analysis if Figure 28 scan (d), and Figure 29 scan (c).....	73
Figure 33 Energy level diagram for the 6.7 nm thick 86 % h-BN film deposited on (100) boron-doped diamond substrate.....	75

Figure	Page
Figure 34	TEM of 14-17 nm thick BN on top of (100) boron-doped diamond surface. The BN layer seems to be in a disordered state of sp^2 often called turbostatic BN..... 75
Figure 35	Experimental flow diagram showing the difference between process A and process B..... 85
Figure 36	XPS and UPS of top: (a) hydrogen-terminated boron-doped diamond, middle: (b) hydrogen-terminated phosphorus-doped diamond, bottom: (c) modified surface of phosphorus-doped diamond..... 87
Figure 37	Band alignment diagram for P-doped diamond for Process A (left) showing the surface state pinning causing the upward band bending. For process B (right) the triple core level, and subsequent triple VBM are shown in different colors. The VBM ranges from upward band bending to flat bands, to downward band bending depending on which peak the VBM is deduced from. 89

1 INTRODUCTION

1.1 Objective and Outline

The object of the research described in this dissertation is the study of the ultra-wide bandgap (UWBG) materials of diamond and boron nitride, and the interface between the two. The electronic, thermal, and structural properties of diamond and boron nitride make these materials ideal for the next generation of high power, high frequency electronics. The emphasis of this dissertation is on the photoelectron spectroscopy characterization of the boron nitride / p-type diamond interface states, and the study of the surface states of p-type and n-type diamond. The fabrication and application of a neutron detector using semiconducting diamond structure and a boron nitride neutron conversion layer will also be discussed. Then we will conclude with a summary of the work done and propose a new neutron detector design structure using boron nitride.

The first chapter of this dissertation will introduce the reader to the current state-of-the-art of boron nitride and diamond research. The second chapter will focus on the equipment used in the experiments, the theory of photoemission, and the interface physics. Further chapters will describe the research findings of this dissertation.

1.2 Boron Nitride History

Boron Nitride has many similarities with the carbon analogs of graphite and diamond. However, these similarities have not always been recognized. Unlike graphite and diamond, no form of boron nitride was found in around volcanic vents according to a volcanological study of boron compounds in 1936. [1] However, a recent report (2014) found a mineral sample from Tibet with micron sized inclusions of cubic boron nitride (c-BN) in chromium rich rock. [2] This was an interesting discovery, as the pressures and temperatures generated when the Indian and Asian continental plates collided had the right conditions for c-BN to form. However volcanic vents, where diamonds are normally found, do not have the right conditions for c-BN to form. The first reported synthesis of boron nitride was in 1842. [1]

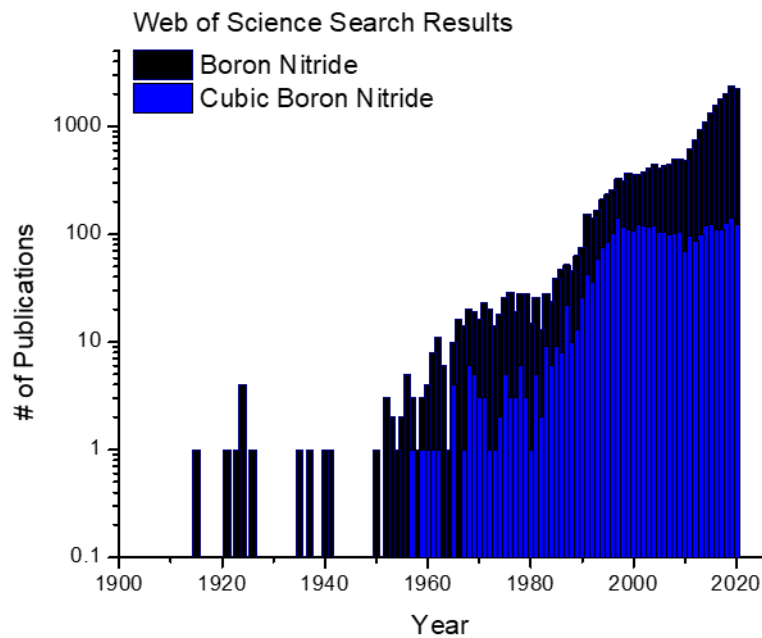


Figure 1 Number of publications per year on boron nitride compared to publications on cubic boron nitride

The products containing boron and nitrogen resembled cyanogen (C_2N_2), and when combined with metals, formed compounds similar to the cyanides. This first reaction to form this BN was a mixture of molten boric acid, mercuric cyanide, potassium cyanide, and sulfur. In the following decades (1850-1910) there were several experiments investigating the reaction pathway to form boron nitride compounds. These reactions used borax, boric acid, or amorphous boron for the boron source, and urea, ammonium salts, ammonia gas or nitrogen at high temperatures ($>1000^\circ C$) to form boron nitride compounds. In 1913 the first patents on stable BN synthesis methods were written and by the 1920's ceramic BN that could be shaped and molded were being investigated. Ceramic boron nitride was found to be very resistant to conventional corrosive acids and bases, or wetting of metals, and did not decompose at or below $1100^\circ C$. In 1945 crucibles made of boron nitride went into production and are still used today.

The possibility of BN in a diamond structure was not considered until 1923. It is interesting to note the spike in publications at this time Figure 1. Shortly after, in 1926, the first investigation of crystalline boron nitride using X-ray diffraction was performed. [1] Amorphous BN was bombarded with cathode rays producing micron sized crystals. The X-ray diffraction pattern of these crystals resembled a hexagonal structure, similar to graphite, and was the first confirmation of hexagonal boron nitride (h-BN). In the following decades (1926-1940) physical, electrical, chemical, and thermal characteristics of BN allotropes were studied.

In 1957 R. H. Wentorf and colleagues were the first to report on the synthesis of cubic boron nitride, via high pressure high temperature (HPHT). [3] Wentorf, first

proposed the name “Borozon” as a unique name for cubic boron nitride, but it seems that this name did not stick. Shortly after (1961) Wentorf published a study on doping of c-BN with Be ($E_A \sim 0.2$ eV) to form p-type c-BN, and doping with S ($E_A = 0.05$ eV) , Si, KCN, and other more complex hydrocarbons to produce n-type c-BN. [4] A p-n junction was attempted with these crystals, but the results were found to not be reliably repeatable, and left much to be desired.

Up to this point (1960’s) the known physical properties of BN were that the hardness and structure was comparable to the carbon analogs of graphite and diamond. These BN crystals were known to be extremely resistant to corrosive acids and bases. In fact, buffered HF etches at < 1 nm/min and 3% hydrogen peroxide at 80C etched at 3.5nm/min. [5] These solutions are destructive to conventional etch-resistant films.

By 1968 there were a few groups studying thin films of boron nitride, mostly producing smooth amorphous films (a-BN), films with a disordered hexagonal structure termed turbostratic BN (t-BN), or hexagonal BN (h-BN) thin films. Mostly these were grown on silicon substrates, but also different metals and fused silica substrates as well. [5] Using thermal vapor deposition with diborane and ammonia gas as the precursors increased the purity of the films. The reaction to produce quality BN films was sensitive to the presence of water down to 200ppm. The thermal CVD method of growing thin films of h-BN produced crystallite sizes about 1-8 nm in width for substrate temperatures at 600C – 1000C respectively, and thickness up to 0.6 mm.

With the slow and steady improvement in synthesis methods the physical, electrical, and chemical properties were more thoroughly investigated. By 1971 the

electronic indirect band gap was measured to be ~5-6 eV (current accepted value ~ 5.2eV) for h-BN and a refractive index of 1.9-2.0. [6] The indirect band gap of c-BN was measured to be 6.4 eV for the first time in 1974 using ultraviolet absorption spectra of single crystals platelets 400 micron in diameter and 20-80 micron thick. [7]

An explosion of research on BN thin films started in the 1960's and into the 1980's can be seen in Figure 1. Vacuum technology was becoming more accessible at the time and a myriad of low-pressure deposition methods were investigated. This was followed by a second surge of publications between (1985-2000) on the use of physical vapor deposition methods, producing thin films of BN.

1.3 Properties of Boron Nitride and Diamond

Boron nitride is a III/V semiconductor that can have either sp^2 -hybridized or sp^3 -hybridized bonding configurations. The molecular orbital hybridization for both sp^2 and sp^3 are depicted in Figure 3, which displays the atomic orbital hybridization and molecular orbital bonding energy diagram for h-BN (top) and c-BN (bottom). The 2s and 2p orbitals have either sp^2 or sp^3 hybridization for hexagonal structure or cubic structure respectively. The B 1s and N 1s core levels are ~191 eV and 399 eV below the Fermi level. The most common phase of BN is the sp^2 hybridized hexagonal boron nitride (h-BN), which is analogous to graphite. The sp^3 hybridized BN is known as cubic boron nitride (c-BN), which is analogous to diamond. The diamond structure is a face centered cubic (FCC) structure, with a basis of two identical atoms, with basis vectors (0,0,0) and ($\frac{1}{4}$, $\frac{1}{4}$, $\frac{1}{4}$). The cubic structure of boron nitride (c-BN) is similar to the diamond structure, but with two distinguishable atoms for the basis, also known as a zinc-blende structure.

The structure, space group, and lattice parameters for these four compounds are shown in Table 1

Diamond, c-BN, and h-BN are all considered wide band gap semiconductors, with indirect band gaps of 5.5 eV, 6.4 eV, and 5.2 eV respectively. The electronic, thermal, and structural properties of c-BN and diamond make these materials ideal for the next generation of high power, high frequency electronics. High thermal stability of these materials enables electronic devices of diamond or c-BN to be used in extreme conditions. From the surface of Venus, with surface temperatures of $\sim 450^{\circ}\text{C}$ and a corrosive atmosphere, too deep within the earth's crust, or even in the intense radiation near the core of a nuclear reactor. The diagram in Figure 2 shows how the mechanical, thermal, and electronic properties of diamond and c-BN are used in potential applications.

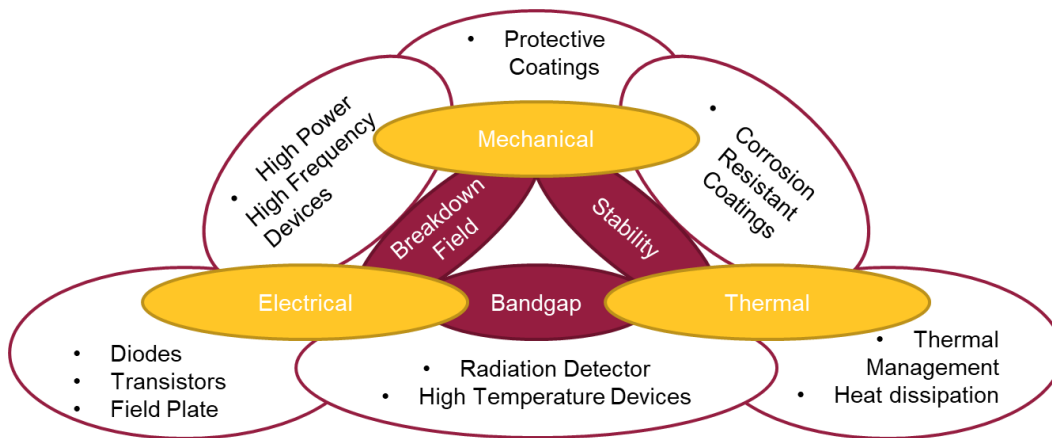


Figure 2 Physical properties and potential applications for diamond, and cubic boron nitride

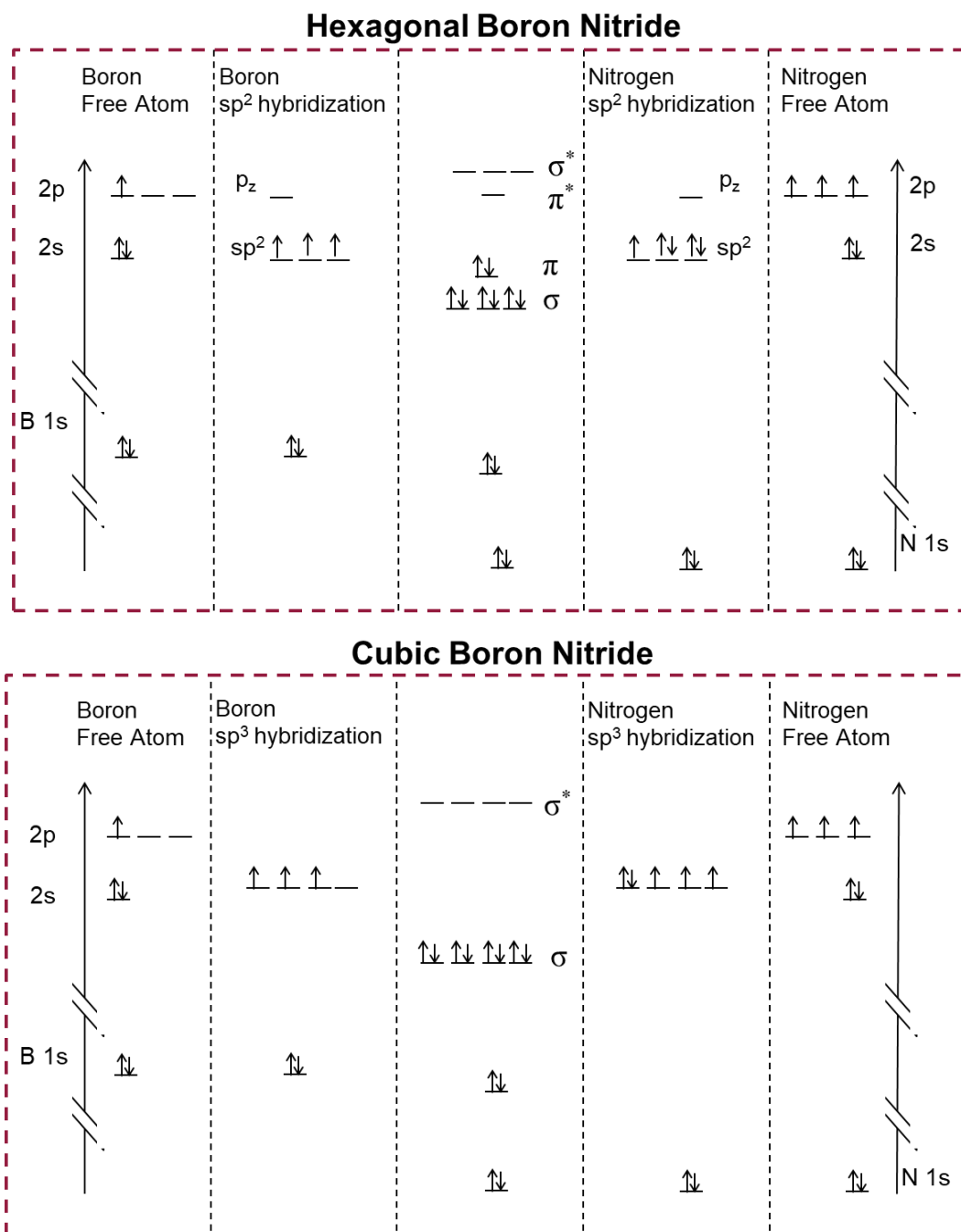


Figure 3 Atomic orbital hybridization and molecular orbital bonding energy diagram for h-BN (top) and c-BN (bottom). The 2s and 2p orbitals have either sp^2 or sp^3 for hexagonal structure, and cubic structure respectively. The B 1s and N 1s core levels are ~ 191 eV and ~ 399 eV below fermi level. The core level shift between the two hybridizations is $\sim 0.5 - 1$ eV

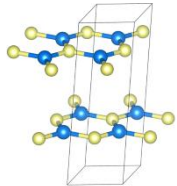
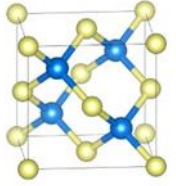
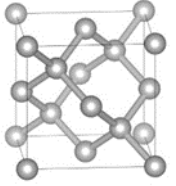
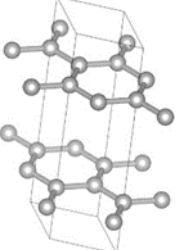
Compound	Hexagonal Boron Nitride (h-BN)	Cubic Boron Nitride (c-BN)	Diamond	Graphite
Structure				
Space Group	P6 ₃ /mmc [194]	F4 ₃ m [216]	Fd3m	P6 ₃ mmc [194]
Lattice Parameter (Å)	a = 2.504 c = 7.707	a = 3.615	a = 3.567	a = 2.461 c = 6.708
Density (g/cm ³)	2.34	3.48	3.51	2.26
Hardness (Mohs)	2	9	10	1-2
Thermal conductivity (W/cmK)	0.2 4 ⊥ [8]	8-16 [9]	20-30 [10]	9-10 0.1 ⊥
Band Gap (eV)	5.2	6.4	5.5	0.04 [11]
Breakdown Electric Field (MV/cm)	10 [12]	8	10	0.1 [13]

Table 1 Physical properties of hexagonal boron nitride, cubic boron nitride, diamond, and graphite

1.4 Current State of the Art Synthesis of Boron Nitride

The current art of the growth/deposition of boron nitride can be divided into two categories, high-pressure and low-pressure methods. Production of high-quality c-BN crystals 1-3 mm in diameter requires temperatures of 1200-1300C and pressures of 4-5 GPa and must be maintained for weeks to months. [14] A recent paper in 2018 used Auger electron spectroscopy to study the growth interface of the HPHT c-BN. [15] Boron nitride can be doped using beryllium (Be) for p-type c-BN and Si or S for n-type c-BN. A p-n junction of c-BN was produced by starting with a p-type seed crystal and the growth of a homoepitaxial n-type layer grown via HPHT. [16] The HTHP method has been essential in the advancement of c-BN research and is used to produce microcrystalline c-BN that is then molded into metals to reduce the wear and increase the lifetime of cutting tools. However, to further advance the electronic understanding of this material, more precise control of the growth of thin films is needed. The low-pressure methods such as physical vapor deposition (PVD), or chemical vapor deposition (CVD) are more suited to film growth than HTHP.

Various physical vapor deposition (PVD) techniques have been successfully used to deposit c-BN thin films since the 1990's. Deposited films using PVD typically have mixed crystal phases of c-BN and hexagonal boron nitride (h-BN), including an amorphous phase at the growth interface. [17] However, there has been a recent report of epitaxial c-BN on diamond using PVD. [18] In general the high ion flux necessary in PVD creates films with poor crystallinity, high defect density, and high internal stress, which can lead to delamination. [17]

Plasma enhanced chemical vapor deposition (PECVD) is known to be effective at producing c-BN films with improved crystalline quality over PVD. [17] [19] [20] However, the presence of h-BN at the interface inhibits large area heteroepitaxy of c-BN needed for many electronic applications. Hexagonal boron nitride (h-BN) has its own unique and interesting properties and being able to selectively grow either phase with high purity would be ideal for future applications of this material. In the early 2000's PECVD employing fluorine chemistry was introduced by groups in Japan and Hong Kong. [21] [22] [23] Including fluorine chemistry is thought to provide preferential etching of h-BN over that of c-BN. The CVD process reduces the required substrate bias, while increasing the crystallinity[14]. One focus of this work is the deposition of boron nitride using electron cyclotron resonance PECVD (ECR-PECVD) for the synthesis of c-BN and h-BN films.

2 INTRODUCTIONS TO EQUIPMENT AND EXPERIMENTS

2.1.1 Substrates for Electron Cyclotron Resonance Plasma Enhanced Chemical Vapor Deposition

The results described in Chapter 3 used the polycrystalline p-type diamond (5 x 5 x 0.3 mm) supplied by Element Six and pictured in Figure 4 as starting substrates. These substrates were mounted on 25.4 mm diameter nichrome plate using tantalum wires. It should be noted that the surface roughness of these starting substrates limits the applicability for interface morphology characterization using SEM, or TEM. They are a good quality, inexpensive option for performing chemistry optimization of the ECR PECVD process because XPS measurements do not suffer from charging effects.

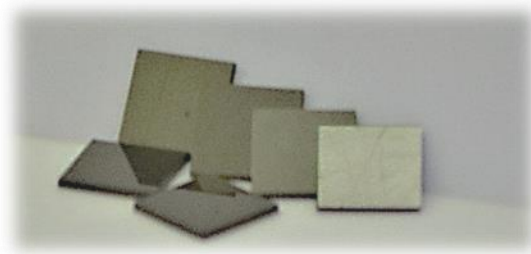


Figure 4 Polycrystalline boron doped diamond substrates from Element Six

For the valence band offset measurements of boron nitride on diamond, the substrates used were (100) boron-doped, p-type diamond (3.0 x 3.0 x 0.3 mm) supplied by the Technological Institute for Super Hard and Novel Carbon Materials (TISNCM). These substrates were also mounted on 25.4 mm diameter nichrome plate using tantalum wires. It should be noted that contamination related to the tantalum wires was visually observed across the surface after deposition of BN. It was necessary to use caution when mounting the substrates with tantalum wire. A new molybdenum mounting plate was

designed to alleviate this issue. Lastly, (111) intrinsic substrate with 5 μ m homoepitaxial Phosphorus-doped diamond layer were studied with photoelectron spectroscopy. These were mounted on the 25.4 mm diameter nichrome plate, but instead of tantalum wires holding the diamond, the new molybdenum plate was fabricated to clamp the substrate to the nichrome plate.

2.1.2 Electron Cyclotron Resonance Plasma Enhanced Chemical Vapor Deposition (ECR PECVD)

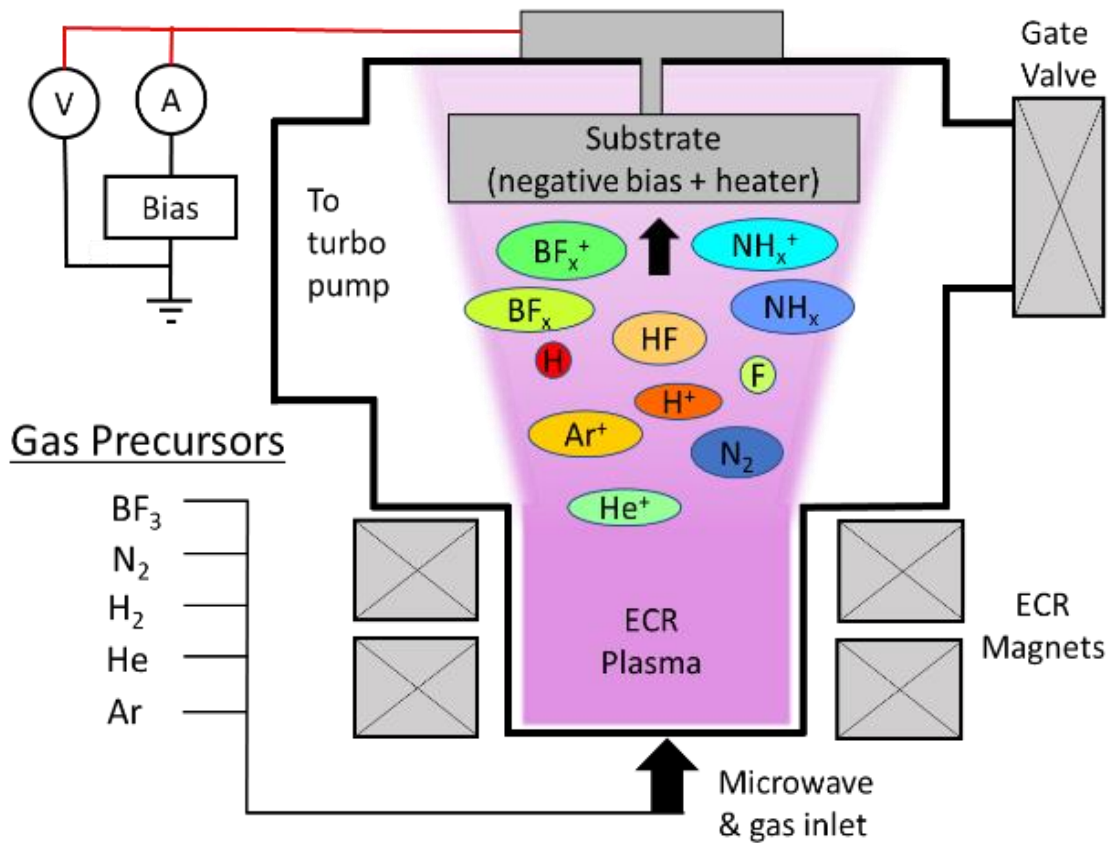


Figure 5 Schematic of ECR PECVD deposition chamber used to deposit boron nitride films

The deposition chamber is a 14-inch diameter stainless steel chamber pumped by a 10 inch turbomolecular vacuum pump backed by a hydrocarbon oil roughing pump. The base pressure of the chamber is 2×10^{-9} Torr. A more detailed description can be found in J. Shammass' dissertation. [24]

Microwaves are generated from an integrated beryllium magnetron wave guide system. The wave guide system consists of a rectangular wave guide which is fused with a perpendicular cylindrical wave guide at the far end away from the source. The wave guides are tuned using a movable rectangular block and a cylindrical rod to minimize the reflected microwave power. A quartz window, which is transparent to microwaves, is used as the atmosphere/vacuum barrier at the bottom of the chamber.

Two electro-magnetic coils, positioned just above the quartz window and separated by 30 cm, generate the electron cyclotron resonance (ECR) zone where the plasma is maintained. The two magnets are operated with parallel currents of different magnitudes. Generally, the currents used are 120 A for the bottom coil and 108 A for the top coil. The different magnetic field magnitudes create a magnetic field gradient, and a magnetic bottle is formed. The bottom coil with a larger magnetic field, reflects more of the charged particles into the chamber center, while the lower current of the top magnets acts as a type of release valve, reflecting charged particles back into the ECR plasma zone, while also allowing for charged particles to pass through and impact the substrate. The magnetic field strength, and magnetic gradient were simulated based on the ECR manual see Figure 6. ECR plasmas operates in the 0.1-10 mTorr range, with ion densities $\sim 10^{12}$ and a degree of ionization $\sim 0.1\%$.

The precursor gas inlet is at the base of the chamber, above the quartz window for microwaves. The gas is then distributed into multiple lines to provide a cylindrically symmetric gas supply into the vacuum chamber.

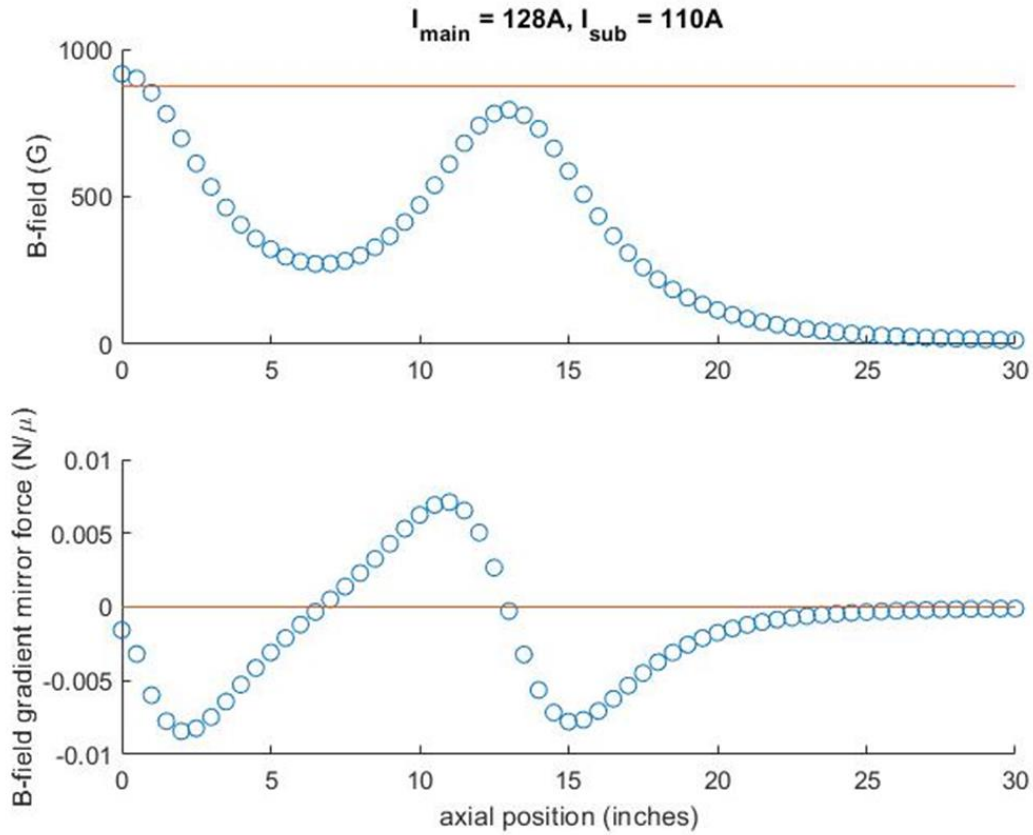


Figure 6 (Top) Magnetic field strength for a bottom magnet current of 128A and a top magnet current of 110A plotted along the central axial position of the chamber. The red line is positioned at 875G, which is the reported resonance with the microwave source. (Bottom) Corresponding magnetic field strength gradient, which is proportional to the force applied to charged particles.

Helium (99.9999% purity) is the largest partial pressure and can be thought of as a carrier gas that also is easily ionized to supply free electrons to the ECR plasma zone.

A small amount of argon (99.9999% purity) is introduced, where the purpose of the Ar is to provide an inert, heavy ion for momentum transfer to the substrate. The ion impact provides energy to enable the formation of sp^3 bonded BN.

Nitrogen gas (99.9999% purity) is the source of nitrogen for the reaction. It is chemically inert and difficult to dissociate even within the plasma. It is likely that only a small fraction of nitrogen gas is dissociated into atomic nitrogen that can then react with the available hydrogen in the system. For this reason, an excess of nitrogen is used in most reactions.

Boron Trifluoride (99.995% purity) is the source of boron and fluorine. It has been shown that fluorine free radicals are effective at etching BN, with a larger etch rate for h-BN over c-BN. A number of studies have employed BF_3 as an ideal boron source for the growth of c-BN.

The role of hydrogen (99.9999% purity) is the focus of Chapter 3. The relative hydrogen concentration was systematically varied to investigate the nucleation, growth, and sp^3 fraction of deposited BN films. Hydrogen when dissociated into atomic hydrogen can react with the free radical fluorine atoms from BF_3 as well as the nitrogen to form NH_x radicals for this reason, in future studies the use of NH_3 as a precursor could enable separate control of the NH_x radicals.

The substrate temperature is controlled by a toroidal tungsten filament, which radiatively heats the sample holder on the back of the substrate mounting plate. The substrate is electrically isolated from the chamber walls and a sample bias is applied during the deposition of BN. A voltage supply is connected to the sample, with the

chamber walls ground, and a negative bias (generally -60V) is applied to the substrate. A voltmeter and ammeter are connected to the voltage supply to monitor the current during growth. A schematic representation of the ECR PECVD system is shown in Figure 5

2.2 PHOTOELECTRON SPECTROSCOPY

2.2.1 Background and General Principles

Photoelectron Spectroscopy (PES) is based on the photoelectric effect. Which was first observed in 1887 by Heinrich Hertz, where he noticed electrons were emitted from a metal surface when irradiated with ultra-violet light. A more formal description was presented by Albert Einstein in 1905, for which he was awarded the Nobel Prize in physics in 1921. X-rays were first reportedly discovered in 1895 by Wilhelm Conrad Roentgen, who was awarded the first Nobel Prize in physics in 1901. Development of stable and intense X-ray sources that can be used for photoelectron spectroscopy took many more decades. However, the bulk of the work to develop x-ray photoelectron spectroscopy into the technique we know today was done by Kai Siegbahn at the Uppsala University in Sweden in the 1950's and 1960's, and in 1981, was awarded the Nobel Prize for his work. With the advancement of theoretical solid state and surface physics, vacuum technology, and electron spectrometers, this technique has become a powerful tool for surface science.

In X-ray photoelectron spectroscopy (XPS) the sample is irradiated with soft x-rays (energies less than ~ 6 keV). In ultra-violet photoelectron spectroscopy (UPS) the sample is irradiated with ultra-violet (UV) light (energies less than ~ 100 eV). In both XPS and UPS the kinetic energy of the emitted electrons are measured. The emitted photoelectron is the result of the complete transfer of energy from the incident photon to an electron in a bound state. This process is expressed mathematically in Equation (1). Energy is conserved, so the energy of the x-ray ($h\nu$) is equal to the binding energy (E_B)

of the electron, plus the kinetic energy (E_K) of the emitted electron, plus the spectrometer work function (Φ_{spec}), which is constant value.

The photoemission process is often described as a three-step process. [25] First an electron absorbs an incident photon with energy $h\nu$, which sends the electron to an excited state with energy greater than E_{vac} . This is followed by the transport of the electron through the material. Only those electrons within a critical distance from the surface, which will be discussed in later sections, and transported in the direction of the surface will be observed. Finally, the electron is emitted from the surface into the vacuum, where it can be considered a free electron with kinetic energy (E_K)

Equation (1) can be rearranged to determine the binding energy of the electron, as the photon energy and spectrometer work function are known values, and the electron kinetic energy is the experimentally measured value. Note that the binding energy (E_B) is measured with respect to the system Fermi level, not the vacuum level. While the kinetic energy (E_K) is described with respect to the vacuum level, which is why Φ_{spec} must be used to obtain the actual kinetic energies. [26] The work function of a material is defined as the difference between the Fermi level (E_F) and the vacuum level (E_{vac}) a long distance from the surface to avoid image charge effects.

$$h\nu = E_B + E_K + \Phi_{spec} \quad (1)$$

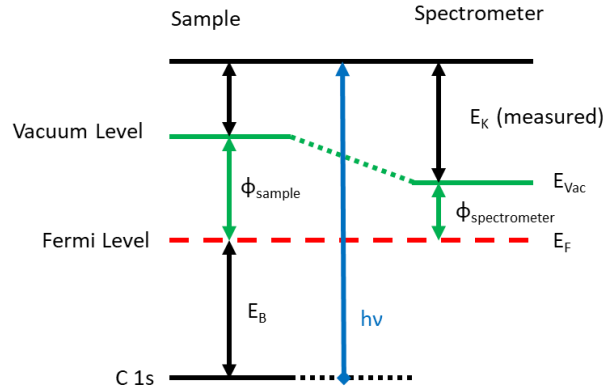


Figure 7 Energy level diagram illustrates schematically the basic XPS equation including x-ray source energy ($h\nu$), the binding energy of the electron (E_B), the measured kinetic energy of the electron (E_K) and the work function of the spectrometer (Φ_{spec}). [26]

2.2.2 Peak Broadening

The intensity as a function of electron energy for the idealized photoelectron emission process results in a set of delta functions as shown in equation (2) where the delta function is defined by the conservation of energy in equation (1). The first term of equation(2), often termed Fermi's Golden rule, is the second order perturbation on a many body wavefunction of the system by an electromagnetic photon field potential. Where Δ is the perturbation Hamiltonian, and $\Psi_i(N)$ and $\Psi_f(N)$ are the initial and final many body wavefunction with energy eigen values of E_i and E_f respectively.

$$I(E) \sim |\langle \Psi_f(N) | \Delta | \Psi_i(N) \rangle|^2 \delta(E_f - E_i - \hbar\omega) \quad (2)$$

The idealized delta function is broadened by the transition lifetime, variations of atomic configurations, and equipment resolution. The transition lifetime creates a Lorentz line shape broadening, while the atomic configurations, and equipment create gaussian

broadening. The combined Gaussian-Lorentz line, or Voigt function is used for curve fitting, and core level peak analysis.

The photon source is not perfectly monochromatic and has a bandwidth of 0.2 eV. The thermal motion (0.025eV) of the atoms contribute a small amount of broadening, as the relative velocity and thus kinetic energy of the emitted electron can change depending on the relative motion of the vibrating atom with respect to the detector. The electrostatic energy lens, baffle slit size, and hemispherical analyzer pass energy also all contribute to the peak broadening. Figure 8 shows the energy resolution and relative intensity for most of the detector pass energies and baffle slit sizes available for the VG Scientia R3000 spectrometer.

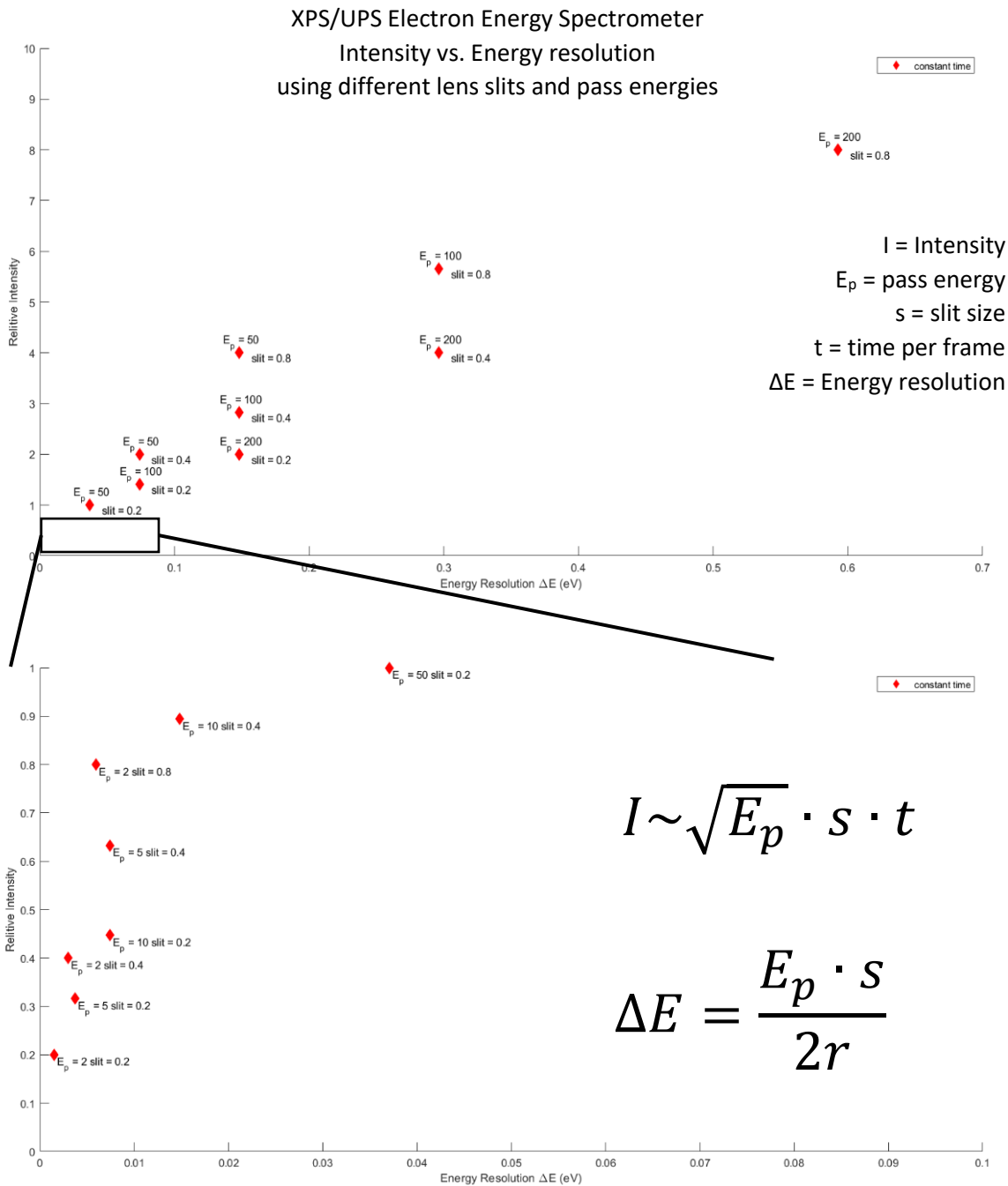


Figure 8 Relative intensity and energy resolution for the VG Scientia R3000 hemispherical analyzer. Each point represents a different pass energy and slit size combo, Relative intensity is calculated per unit of time. For future student reference

2.2.3 Photoelectron Energy Loss

The X-rays that irradiate the sample can penetrate a few microns into the sample material. [26] Photoelectrons generated this deep will encounter many inelastic collisions as they travel and will eventually lose all their energy before escaping from the surface. In Figure 10 (a) the path labeled C represents electrons generated deep in the sample. Closer to the surface photoelectrons may only experience inelastic collisions before escaping the surface represented by line B in Figure 10 (a)

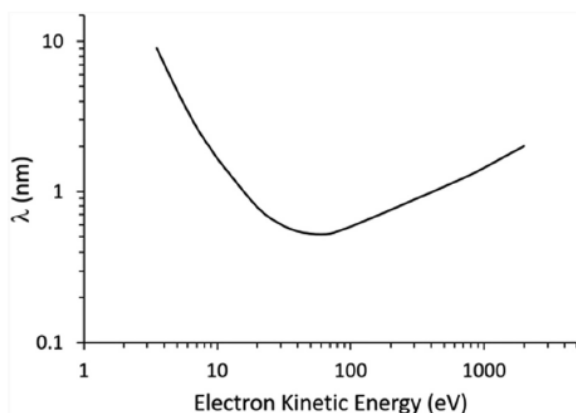


Figure 9 Universal IMFP curve.

These inelastic collisions contribute to the background of the photoelectron spectrum, shown in Figure 10 (b) for the N 1s core level, shaded in orange. This example of the full energy scale photoelectron spectrum is from a thin layer of boron nitride, on a diamond substrate. The surface sensitivity of PES is a result of the depth from which a photoelectron can be generated and be emitted from the surface.

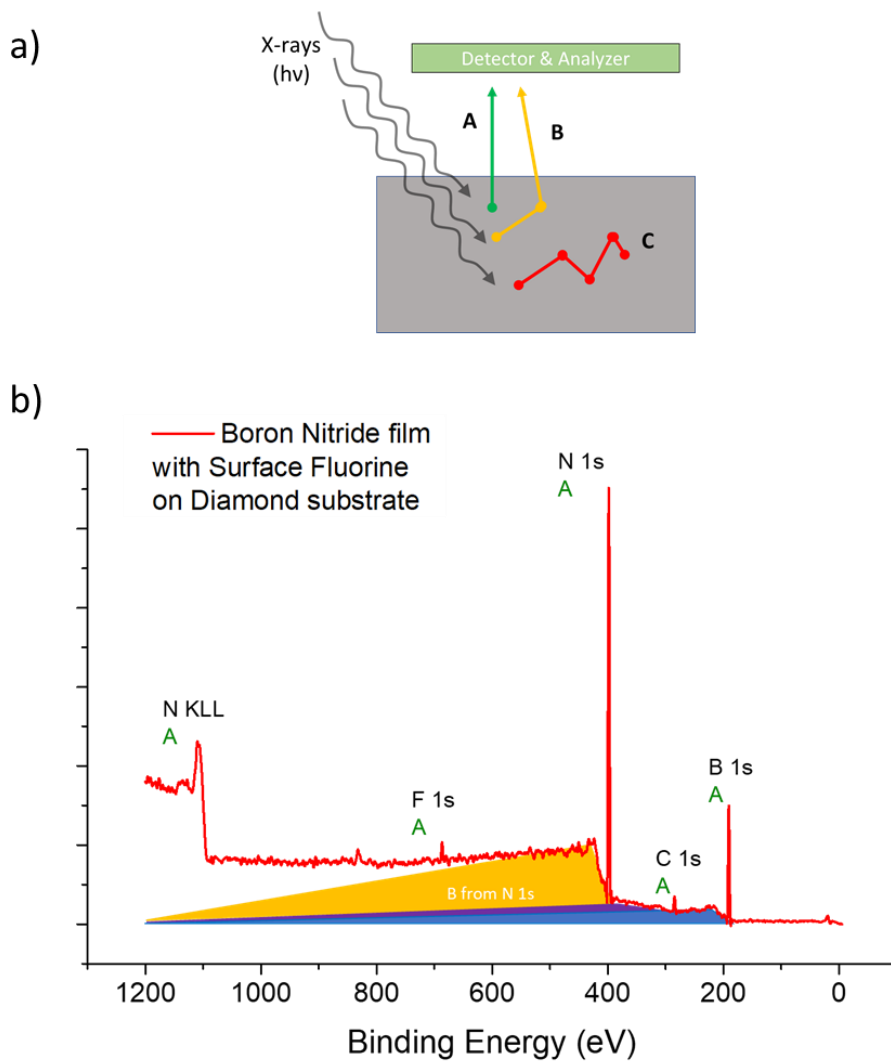


Figure 10 (a) Schematic representation of photoelectron generation, and transport to surface. Electrons emitted without interaction, labeled (A) produce core level and auger peaks. Electrons which undergo at least one inelastic collision, labeled B, contribute to the background. Electrons which undergo multiple collisions and do not escape the sample are labeled C.

(b) Shows a sample XPS spectrum with core level and auger peaks labeled. The orange shaded area shows the contribution to the background from the N 1s electrons, similar background contributions are made by the electrons from the B 1s and the N Auger transitions as well, forming the vertical “steps” in the baseline observed for every major peak

Beers-Lambert law (equation (3)) describes the intensity of photoelectrons (I) emitted from below a depth (d). where I_0 is the total number of electrons generated. [26], The term λ is the attenuation coefficient of the electron, which is closely related to the inelastic mean free path (IMFP). This describes the distance which the electron is likely to experience an inelastic collision. The actual value of the IMFP depends on the kinetic energy of the electron, and the density of the material.

$$I = I_0 e^{\frac{-d}{\lambda}} \quad (3)$$

The thickness of the overlayer (BN in this example) can be determined by the relative intensity of the photoelectron core levels. [27] The attenuation of electrons through a material is energy dependent. The energy dependence of the attenuation length follows a universal curve shape shown in Figure 9. The IMFP also depends on the energy band gap of the material, which needs to be considered for wide band gap materials like c-BN, h-BN, and diamond. This energy loss mechanism can be used to determine the thickness of an overlayer. By first measuring integrated area of the bare substrate core level (I^S), and the integrated area of the substrate core level after an overlayer is deposited (I^O) Take the ratio to obtain the deposited overlayer thickness (t)

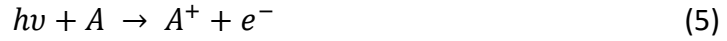
$$\frac{I^O}{I^S} = \frac{I_0 e^{\frac{-(d+t)}{\lambda}}}{I_0 e^{\frac{-d}{\lambda}}} = e^{\frac{-t}{\lambda}}$$

Solve for thickness t

$$t = \lambda \cdot \ln \left(\frac{I^S}{I^O} \right) \quad (4)$$

Where λ is the IMFP of substrate electrons traveling through the overlayer. For C 1s stimulated with an Al- $\kappa\alpha$ source, the IMFP through c-BN is 2.0 nm, and through h-BN is 2.4 nm. [28]

The photoionization process can also be described using chemical state notation as in equation (5). Where a photon of energy ($h\nu$) colliding with an atom (A), resulting in the ionization of that atom (A^+) and an ejected electron (e^-) with kinetic energy (E_K) greater than the vacuum energy (E_{vac}).



In most instances the atom (A) and the ion (A^+) are left in the ground state, this is the atomic core level energy. In some fraction of the photoionization interactions, the resulting ion can be left in an excited state.



This means that the emitted photoelectron has less kinetic energy than if the atomic ion were in the ground state. The smallest energy difference with respect the ground state photoelectron emission is the difference between the highest occupied molecular orbital (HOMO), and the lowest unoccupied molecular orbital (LUMO). For crystalline materials this equates to the value of the energy gap between the conduction band minimum (CBM) and the valence band maximum (VBM). This energy loss process is referred to as a “shake-up” process. [26] As there are many excited states above the CBM, there is a wide energy distribution in the photoelectron kinetic energy that is less

than this minimum energy loss of the band gap that adds to the emission spectrum width to higher binding energy.

The shake-up process can create plasmons, a collective oscillation of valence or conduction electrons. The resonant collective transitions from the π and σ bonding states to the π^* and σ^* antibonding states are called π -plasmon, and σ -plasmon respectively. The inelastic collision of the photoelectron with π -plasmons, or σ -plasmons can be observed at higher binding energies than the core level excitation. The energy loss of the π -plasmon is a characteristic of the sp^2 bonded h-BN and can be used to identify the phase of the deposited material. The absence of the π -plasmon, centered at ~ 200 eV, implies that the film only has σ -plasmons, and σ bonds, characteristic of sp^3 bonded c-BN

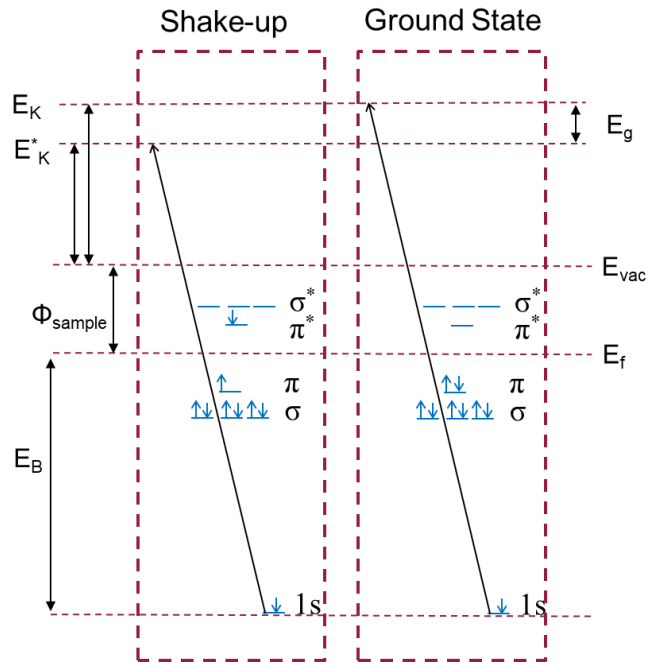


Figure 11 Shake up process for h-BN. The excitation of the host atom into the π^* state reduces the kinetic energy of the ejected $1s$ core electron by exactly the quantized energy difference between the excited state and the ground state. For h-BN this is equal to the band gap (~ 5.2 eV)

2.3 Photoelectron Spectroscopy System and Calibration

2.3.1 Monochromatic X-ray Source

A VG Scientia MX 650 high intensity monochromatic Al K_{α} x-ray source 1486.6 eV with a bandwidth of 0.2 eV is the photon source for XPS measurements. The X-rays are generated in a water-cooled vacuum chamber by accelerating electrons from a tungsten cathode at a high voltage (15keV) relative to an aluminum anode. The accelerated electrons bombard the aluminum and the deceleration of these electrons generates a distribution of x-rays. The nonmonochromatic x-rays radiate toward a set of seven 76 mm diameter toroidal α -quartz single crystals. One quartz crystal is located at the center and six positioned in a circle around the center. All seven crystals are placed on a Rowland circle of 650 mm diameter. These quartz crystals are heated to 55 °C to avoid photon energy shifts caused by temperature changes of the quartz during the measurements.

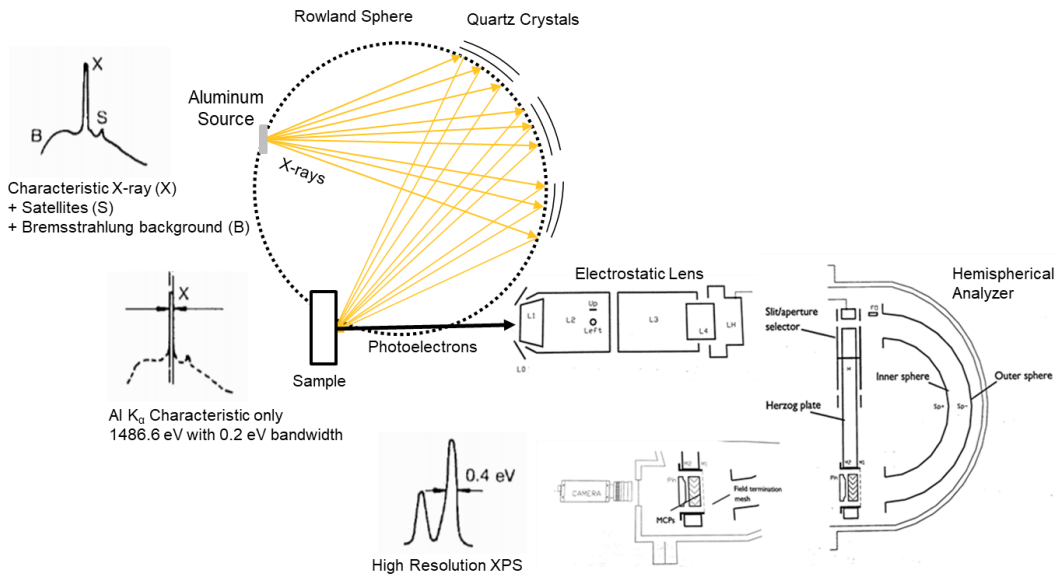


Figure 12 Schematic process of X-ray generation, monochromatization, photoelectron generation, and electron analyzer for High Resolution XPS measurements

2.3.2 Ultra-Violet Light Source

A helium discharge lamp is used as the UV source, which is excited by a DC discharge. The helium lamp produces resonance emission lines at photon energies of 21.22 eV (He I α), 23.09 eV (He I β), 40.81 eV (He II α), and 48.37 eV (He II β). [29] The most intense is the He I α line with energy 21.2 eV. As the lowest energy of the emission lines, He I α is used to measure the work function of the materials. The He I β emission line at 23.1 eV can cause some difficulty in the analysis of the valence band maximum from He I α for wide band gap semiconductors. The 2.1 eV difference between He I α and He I β can distort the signal and produces a tail toward lower binding energies and introduces an uncertainty in the analysis of the VBM.

The He II α resonance emission at 40.8 eV is more appropriate for at determining the VBM. While it has a lower intensity, the absorption cross section of He II α is greater for valence band spectrum than He I α . Consequently, the photoelectron signal is sufficiently high to detect, while avoiding the pesky 2 eV separation in the photon lines between , He I α and He I β . Since the band gaps of diamond and boron nitride are in the range of 5.2-6.4 eV, the 7.6 eV difference between He II α and He II β does not cause the same analysis difficulties as He I α and He I β

2.3.2 Calibration of Photoelectron Spectroscopy System

The XPS/UPS system was calibrated using a hydrogen plasma cleaned gold surface. The calibration sample structure uses a 25.4 mm diameter p-type silicon wafer, with 50 nm of titanium, 50 nm of platinum, and 150nm of gold. All metals were deposited using an e-beam deposition system. Prior to calibration a hydrogen plasma cleaning was performed in the ECR PECVD system. The calibration sample was cleaned, and then transferred in-situ to the XPS/UPS chamber.

The calibration procedure detailed in {Modern ESCA, Chapter: 3} was followed. [30] For XPS measurements, the high pass detector configuration, with a pass energy of 100 eV, and a slit size of 0.4 mm (curved slit) was used. The Fermi edge (0.00 eV) of gold was used as one calibration point and the Au 4f^{7/2} peak at 84.00 eV is a second calibration point for the XPS detector settings, see *Figure 13*.

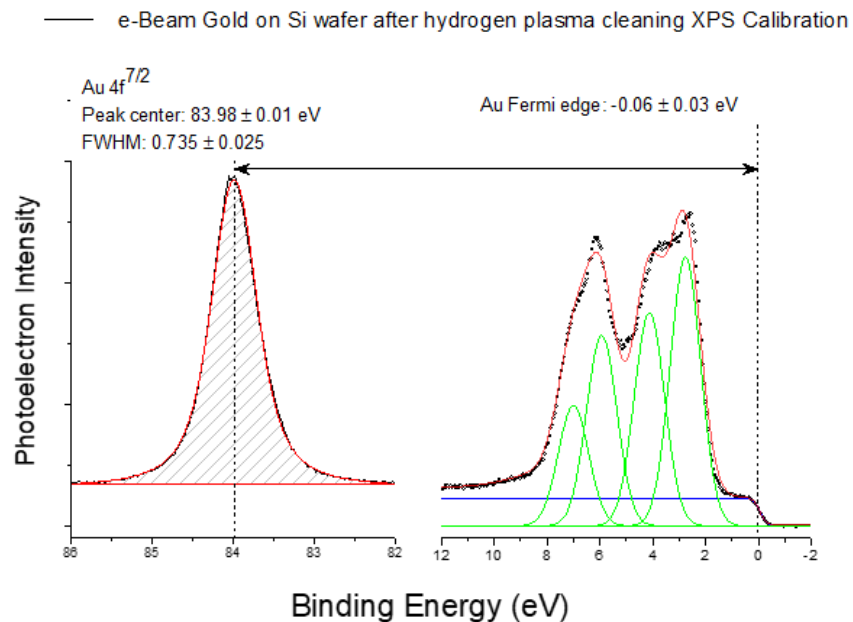


Figure 13 XPS calibration curves of clean gold surface.

For UPS measurements, the low pass detector configuration, with a pass energy of 2 eV, and a slit size of 0.4 mm (curved slit) are used. The Fermi edge of gold was used as the calibration point for the UPS settings. The measured Fermi edge using UPS and XPS are in good agreement see Figure 14. Two different metals (platinum (Pt), and palladium (Pd)) were used to confirm the calibration to the Fermi edge.

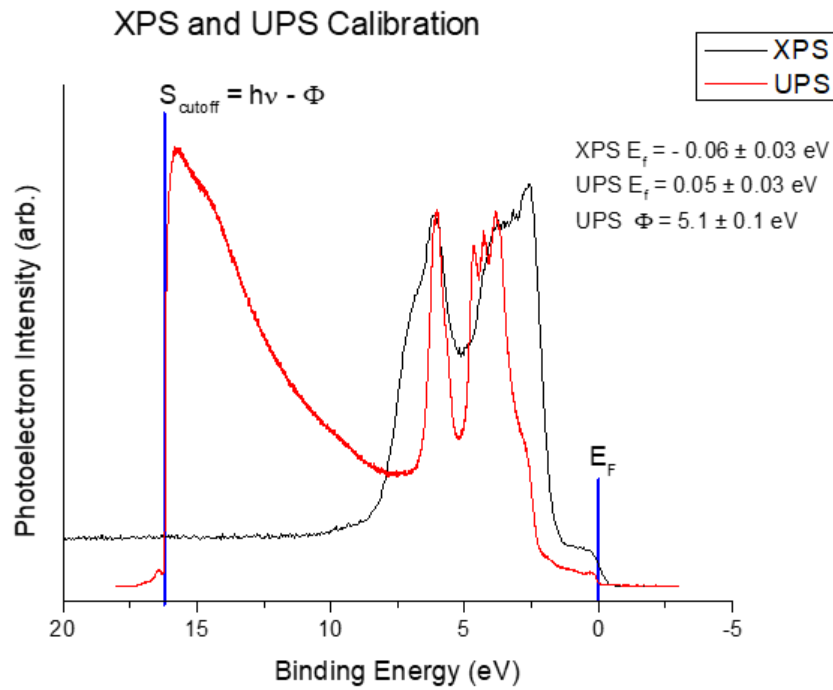


Figure 14 E-beam deposited gold on silicon wafer after a hydrogen plasma cleaning. The blue lines denote the Fermi level and secondary electron cutoff (S_{cutoff}). The S_{cutoff} is used to calculate the work function. ($\Phi = 21.2 - 16.1 = 5.1$ eV)

2.4 Surfaces and Interface Physics

2.4.1 Surface States

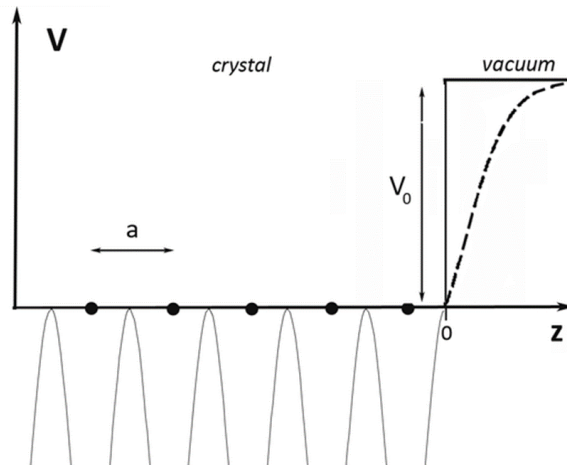


Figure 15 Simplified one-dimensional model of a periodic crystal potential terminating at an ideal surface. At the surface, the model potential jumps abruptly to the vacuum level (solid line). The dashed line represents a more realistic picture, where the potential reaches the vacuum level over some distance.

The definition of a crystal is the presence of translational symmetry. This symmetry provides a periodic boundary condition for the electronic wave functions. Which is one of the most key considerations when calculating the bulk electronic states in a crystal. However, when studying surfaces, there is one direction that has no periodic boundary, and instead has an abrupt potential barrier. This is the root cause of surface states. For semiconductors dangling bonds, or surface atomic orbitals (Tamm states) also create surface states.

When the system in question is near a surface, there is symmetry breaking and there are different solutions to the wavefunction in this anisotropic direction, when compared to the bulk wavefunctions. Surface states can exist within the bulk band gap and can cause band bending.

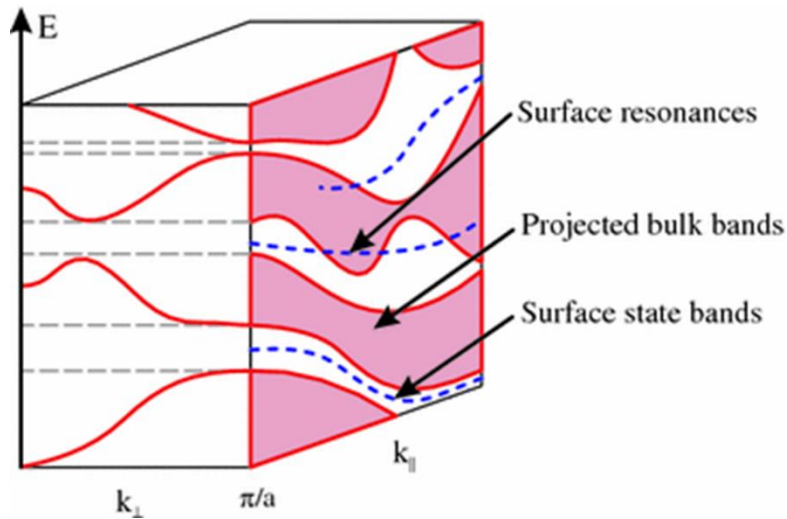


Figure 16 Example of energy dispersion relation, with projected bulk bands and surface states. Surface states only exist in the k_{\parallel} direction

Covalent crystals like silicon or diamond have surface state densities approximately equal to the atomic surface density. Both silicon and diamond are known to undergo surface reconstruction. Ionic crystals like III-V semiconductors have in general less surface states than covalent crystals, as the electrons are more localized from the charge transfer between bonding atoms.

The difference between the abrupt vacuum interface and the smooth vacuum interface gives rise to a fundamental question. What is the uncertainty of a surface?

$$\Delta z \Delta p \geq \hbar/2$$

2.4.2 Band Bending

Band bending is caused by the presence of an electric field in a semiconductor. [31] The electric field can be applied externally (Field-effect band bending) or due to an accumulation of charges at the interface. The presence of an electric field near the

interface effectively separates the electrons—hole pair and inhibits the electron—hole pair recombination.

There are many mechanisms to induce band bending at the semiconductor surface. The metal/semiconductor interface can induce band bending in the semiconductor and create a potential barrier between the two materials. This is commonly known as a Schottky Barrier. The bending in metals can be ignored as the conductivity quickly eliminates any internal electric fields. Surface states also accumulate charges, and thus can cause band bending. Molecules adsorbed to the surface act as electron acceptors, or donors and thus become charged which also induces band bending.

Semiconductor heterojunctions can also induce band bending if there is a charge transfer across the interface. The band bending between two semiconductors can be influenced by many factors such as doping type and concentration, particle size, surface structure, phase, etc. Optimization of charge transfer process at semiconductor surfaces by manipulation of energy bands is a theme of broad generality and current applicability.

Band bending at the semiconductor interface can be measured if the material band gap, doping density, and bulk VBM are known. [32] The difference between the measured VBM of the surface, using UPS (or XPS) and the bulk VBM reflects the band bending. The difference between the core level binding energy and the VBM ($\Delta E = E_{CL} - E_{VBM}$) is a constant for each unique material. If ΔE is measured on the initial substrate, then any surface modifications that change the band bending can be observed by the shift of the core level, and/or the change in the surface VBM.

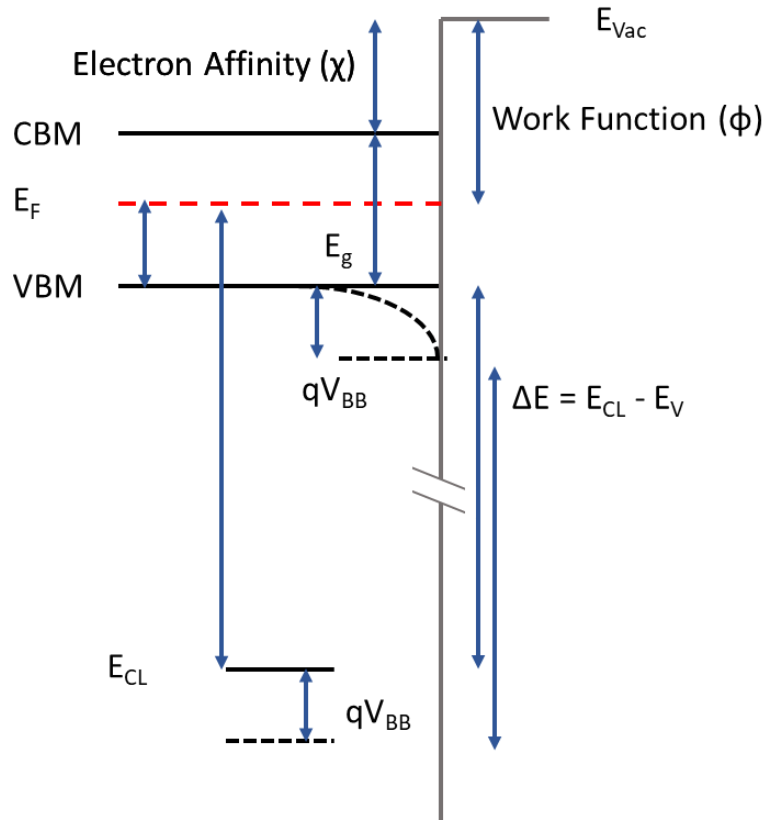


Figure 17 Schematic representation of downward band bending ($q \cdot V_{BB}$). The change in the core level and VBM at the surface can be measured with XPS and UPS.

2.4.3 Valence Band Offset

The valence band offset (VBO) at a heterojunction interface is measured in a similar fashion, by using the method proposed by Waldrop, Grant, and Kraut. [33] The VBO between substrate and overlayer can be calculated using:

$$\Delta E_V = \Delta E_{CL} + (E_{CL} - E_V)_{Overlayer} - (E_{CL} - E_V)_{Substrate} \quad (7)$$

Where ΔE_V is the VBO, E_{CL} and E_V are the binding energies of the core level and the VBM of the corresponding substrate or overlayer, and ΔE_{CL} is the difference in core level

energies between the substrate and overlayer. The experimental procedure to measure the VBO is as follows:

- (1) – Measure the clean substrate E_{CL} via XPS, and E_V via UPS (He II)
- (2) – Deposit a thin overlayer ($\lesssim 5$ nm) on the substrate, such that the E_{CL} of both the substrate and overlayer are measurable to obtain ΔE_{CL}
- (3) – Deposit a thick overlayer (> 15 nm) to measure the overlayer E_{CL} and E_V just as in step (1). The substrate core level should not be visible in the XPS spectrum. If the $(E_{CL})_{\text{substrate}}$ in step (2) has shifted relative to $(E_{CL})_{\text{substrate}}$ in step (1), then there is band bending in the substrate. Similarly, if $(E_{CL})_{\text{overlayer}}$ in step (2) is shifted relative to $(E_{CL})_{\text{overlayer}}$ in step (3), then there is band bending in the overlayer.

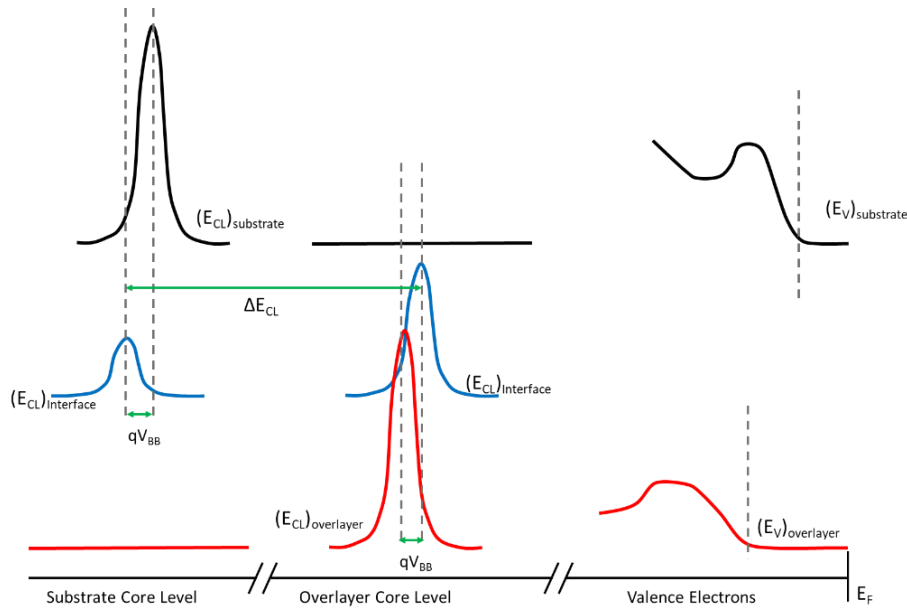


Figure 18 Representation of the three-step process described above. The top black curves represent the clean substrate in step (1). The middle blue curves represent the core levels at the interface. The substrate core level shift to higher binding energies represents downward band bending at the interface. The red curves represent the thick overlayer in step (3). The overlayer shift in binding energies indicates there is upward band bending toward the interface.

Similarly, if there is a difference in overlayer core level energies, then there is band bending in the overlayers as well. While band bending is continuous and occurs over 10's of nm within the corresponding semiconductors, the VBO is a discontinuity at the interface, confined to only the interfacial bonding layers. Given that XPS and UPS are so surface sensitive, and assuming that the overlayer is thin enough that band bending can be ignored in most cases.

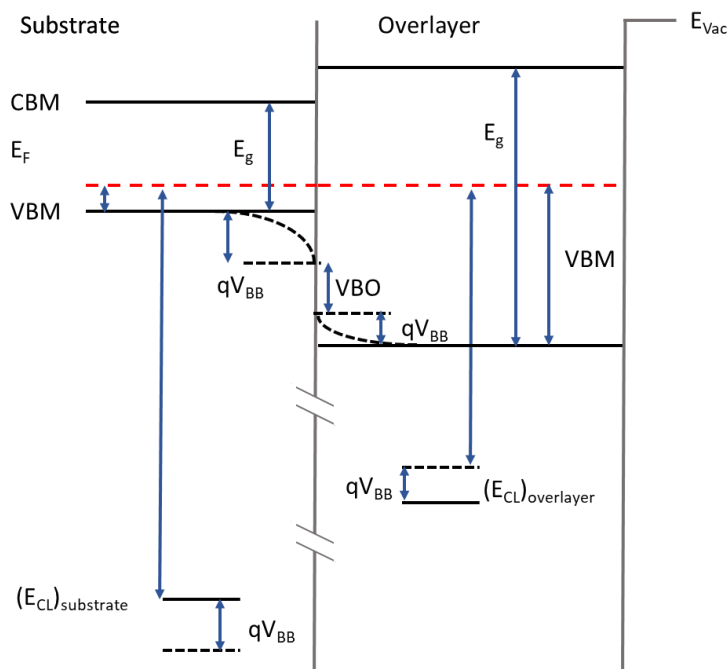


Figure 19 Energy band alignment diagram using the representative data in Figure 18. In this example, the substrate is p-type, and exhibits downward band bending, while the overlayer, which has a larger band gap than the substrate exhibits upward band bending toward the interface. The VBO is the discontinuous energy barrier between the substrate and the over layer, and in this example is a negative VBO, as the overlayer VBM is below the substrate VBM

3 NUCLEATION OF CUBIC BORON NITRIDE ON POLYCRYSTALLINE BORON-DOPED DIAMOND VIA PLASMA ENHANCED CHEMICAL VAPOR DEPOSITION

3.1 Abstract

Cubic boron nitride (c-BN) has been deposited on free standing polycrystalline boron doped diamond substrates via electron cyclotron resonance plasma enhanced chemical vapor deposition (ECR PECVD), employing fluorine chemistry. In-situ X-ray photoelectron spectroscopy (XPS) is used to characterize the nucleation and growth of boron nitride (BN) films as a function of hydrogen gas flow rates during deposition. The PECVD growth rate of BN was found to increase with increased hydrogen gas flow, and in the absence of hydrogen gas flow the BN layer was reduced in thickness or etched. XPS results show that an excess of hydrogen gas significantly increases the percent of sp^2 bonding, characteristic of hexagonal BN (h-BN), particularly during initial layer growth. Reducing the hydrogen flow, such that hydrogen gas is the limiting reactant, minimizes the sp^2 bonding during nucleation of BN. The limited hydrogen reaction is found to be a favorable growth environment for c-BN on polycrystalline boron-doped diamond.

3.2 Introduction

With properties rivaling diamond, the cubic phase of boron nitride (c-BN), with a zinc blende structure, has received interest as an ultra-wide bandgap semiconductor (~ 6.4 eV). A high thermal conductivity of ~ 13 W/cm K [34], chemical inertness [35], and an oxidation stability up to 1500 °C [34] make c-BN an ideal material as a protective coating in extreme corrosive and thermal environments. With hydrogen termination, c-BN has been shown to have a negative electron affinity (NEA) making it a promising material for thermionic devices [36] [37] [38]. Both p-type and n-type doping have been previously

demonstrated [35]. A predicted high breakdown field (~8-13 MV/cm) [34] [39] would enable applications in high power and high frequency devices [40]. Additionally, c-BN can act as an efficient thermal neutron to alpha converter [41] [42]. The thermal neutron absorption cross-section of ^{10}B is one of the largest of all elements (~3840 barns) [43]. Therefore, semiconducting c-BN structures may have potential application as a highly efficient thermal neutron detector.

The first reported synthesis of c-BN was in 1957, using a high-pressure high temperature (HPHT) method at the GE Research Laboratories [3]. Most reports of c-BN HPHT synthesis described c-BN crystals ~ 10 -100 μm in diameter, which are used as an abrasive or as a protective layer for cutting tools. A major limitation of using HTHP c-BN for electronic applications is the crystal size, the largest of which have only reached a few millimeters, too small for most electronic applications [35] [39]. High quality thin films of c-BN can be an alternative to bulk c-BN for many electrical applications such as diodes, or as a dielectric [44]. Diamond is an ideal substrate for c-BN thin films due to its small 1.4% lattice mismatch, which provides a low stress template for heteroepitaxy. Recent advances in diamond growth technology have provided consistent quality single crystal substrates.

Various physical vapor deposition (PVD) techniques have been successfully used to deposit c-BN thin films since the 1990's [35]. Many previous reports of PVD c-BN on diamond have described mixed crystal phases of c-BN and hexagonal boron nitride (h-BN), with an amorphous phase at the growth interface [39]. The high energy ions (Ar^+ , N^+) typically used in PVD of c-BN, can produce films with poor crystallinity, high defect density, and high internal stress, which leads to delamination [35] [39]. Thin films of c-

BN deposited using PVD require high energy ion bombardment, with accelerating voltages of ~ 300 - 400 V to enable formation of c-BN [45]. A recent report has shown epitaxial c-BN on (111) diamond using ion beam assisted MBE. [18] This report found that for high substrate temperatures (~920°C) epitaxial c-BN on (111) diamond was observed. However, stacking fault defects in the c-BN film were still observed, which caused rotated crystal domains, and the formation of the wurtzite structure at the growth interface.

Alternatively, plasma enhanced chemical vapor deposition (PECVD) relies on surface chemistry as the growth mechanism, instead of ion bombardment used in PVD. PECVD has been shown to be effective at producing c-BN films with improved crystalline quality over PVD [35] [39] [46]. However, the presence of hexagonal boron nitride (h-BN) at the interface inhibits large area heteroepitaxy of c-BN, which is needed for many electronic applications. In fact, h-BN has its own unique and interesting properties and being able to selectively grow either phase with high purity could be important for specific applications of this material.

The incorporation of fluorine chemistry during the PECVD process provides a chemical mechanism for the preferential etching of h-BN [46] [23]. Atomic fluorine, produced in the plasma, were shown to etch h-BN at a higher rate than c-BN. [21] [23] Moreover, the gas phase ratio of H/F was found to strongly influence the growth rate, and BN phase purity [23]. The PECVD precursor gases of boron trifluoride, nitrogen and hydrogen, react to form the proposed surface growth reactants of BF_x and NH_x [46] [23] [21]. Previous work from our group on PECVD of BN [36] has shown that the substrate bias can also be used to control the phase of the deposited film. For an applied bias below

a critical value ($V_{\text{applied}} < 40\text{V}$) the BN thin films had a majority of h-BN phase. Above this critical bias value, there is a range of bias values ($40\text{V} < V_{\text{applied}} < 100\text{V}$) that produces films that are predominately c-BN. Increasing the bias further ($V_{\text{applied}} > 125\text{V}$) results in etching of the deposited film. This study, which is focused on the surface chemical effects, is completed with a bias of 60V which is within the range of applied bias that is favorable for c-BN growth.

First principle calculations based on density functional theory have been performed to study the role of hydrogen defects in h-BN and c-BN structures [47]. The results indicate that hydrogen defects in h-BN form between layers with minimal distortion of the local structure. While hydrogen defects in c-BN are incorporated along B—N bonds, significantly distorting the tetrahedral structure toward a more planar structure, similar to h-BN. These calculations suggest that the incorporation of hydrogen defects during the nucleation of BN would be beneficial for the formation of h-BN, while detrimental to the formation of c-BN.

In this work we investigate the role of hydrogen gas on the nucleation and growth of c-BN on diamond using PECVD and fluorine chemistry. Based on the experimental evidence of preferential etching of h-BN by fluorine free radicals and the calculations on the role of hydrogen defects we anticipate a trend in the h-BN to c-BN ratio as the hydrogen gas flow is systematically varied. X-ray photoelectron spectroscopy is employed, enabling the characterization of sp^2 or sp^3 bonding of the as-grown thin films, as well as the thickness as a function of hydrogen gas flow.

3.3 Experiment

Deposition of boron nitride was performed on boron-doped polycrystalline diamond plates (5mm x 5mm x 0.45mm; doping concentration $[B] = 2-6 \times 10^{20} \text{ cm}^{-3}$; supplied by element six). Each substrate was mounted on a nichrome (Ni/Cr/Nb) plate with tantalum wires and bound to a molybdenum sample holder. The polycrystalline diamonds have the rough side ($R_a \sim 50 \mu\text{m}$) in contact with the nichrome plate. The smooth side ($R_a < 30 \text{ nm}$) is employed as the BN growth surface. The sample holder is placed into the load locked transfer line, an integrated vacuum system with a base pressure of $5 \cdot 10^{-9}$ Torr. Thus, the sample maintains a clean surface or a growth surface during *in-vacuo* transfer between the deposition chamber and surface characterization chamber.

	Clean	Deposition
Substrate Temperature	$825 \pm 25 \text{ }^\circ\text{C}$	$825 \pm 25 \text{ }^\circ\text{C}$
Chamber Pressure	$2 \cdot 10^{-4} \text{ Torr}$	$2 \cdot 10^{-4} \text{ Torr}$
Applied Bias	N/A	-60 V
Deposition Time	30 min at temperature with gas flow + 10 min plasma + cooldown in vacuum	Varied
Gas flow (sccm)		
He	0	35
Ar	0	2.5
N ₂	0	12.5
BF ₃	0	1
H ₂	20	0, 1, 2, 3, 4

Table 2 Experimental parameters for sample cleaning and deposition. Hydrogen plasma is used for cleaning the substrate. The deposition time varies depending on the hydrogen flow and the desired thickness of the film. These parameters are chosen based on prior work by [Shammas et al.]. [24]

An electron cyclotron resonance (ECR) plasma enhanced chemical vapor deposition (ECR PECVD) chamber was used for cleaning the substrate and for the deposition of boron nitride. The cleaning and deposition parameters are listed in Table 2. A 35cm diameter stainless steel chamber is pumped by a 25.4 cm diameter Pfeiffer turbomolecular pump (Model: TMU-1600) which maintains a base pressure of $\sim 3.0 \cdot 10^{-9}$ Torr monitored by a cold cathode gauge. An ASTeX 1500i microwave (2.45 GHz) generator coupled with a magnetic field of ~ 875 G applied by two ASTeX ECR magnets sustains the plasma. The precursor gas mixture (He / Ar / N₂ / H₂ / BF₃) is introduced below the ECR magnets. The substrate is radiatively heated by a toroidal tungsten coil and monitored with a Mikron M90Q optical pyrometer. During deposition, a negative bias is applied to the substrate and sample holder ($V_{\text{Applied}} = -60$ V).

In-situ X-ray photoelectron spectroscopy (XPS) is used to analyze the deposited surface. The monochromatic Al-K α x-ray source ($1486.7\text{eV} \pm 0.2\text{eV}$) is focused to a 7 x 2 mm spot size at the sample surface. Each sample is mounted such that the diagonal of the substrate aligns with the X-ray spot to minimize signal from the nichrome mounting plate. The chamber base pressure is $5 \cdot 10^{-10}$ Torr monitored with a hot filament ion gauge. A VG-Scientia R3000 spectrometer with a four-element electrostatic lens is used in sweep mode to scan the full energy range of photoelectrons. The hemispherical analyzer has a slit size of 0.4 mm, and the pass energy is 100 eV giving an energy resolution of 150 meV. The energy resolution of the spectrometer combined with the monochromatic X-ray source, enables a resolution limited FWHM of ~ 0.25 eV. The spectrometer is calibrated using a plasma cleaned gold foil and setting the Au 4f_{7/2} peak center at 84.00 ± 0.01 eV.

The XPS spectra are fit with a sum of Gaussian, and/or Voigt functions using Origin Pro 8.5.1 software. Peak centers correspond to the binding energy (relative to the Fermi level) of the core level electrons, which have characteristic energy ranges depending on the chemical bonding of the element. The integrated peak areas are used to calculate the following quantities:

$$\text{Thickness of deposited layer [27]} \quad t = \lambda \cdot \ln \left(\frac{I_{C1s}^s}{I_{C1s}^o} \right)$$

$$\text{The percent of } sp^2 \text{ hybridization (h-BN)} \quad \%sp^2 = 100 \times \frac{I_{B\pi^*}}{I_{B1s}} / \left(\frac{I_{B\pi^*}}{I_{B1s}} \right)_{Ref}$$

The C 1s peak area of the clean Substrate (I_{C1s}^s), the C 1s peak area after depositing an Overlayer of BN (I_{C1s}^o) and the inelastic mean free path ($\lambda = 2.00$ nm) [48] of the C 1s photoelectrons traveling through BN are used to calculate the thickness of the deposited film [27]. The π -plasmon ($I_{B\pi^*}$) is characteristic of sp^2 bonding of h-BN. The absence of this peak implies the film has only σ bonds, characteristic of sp^3 bonding of c-BN. A single crystal h-BN reference sample was prepared to determine the peak areas,

$\left(\frac{I_{B\pi^*}}{I_{B1s}} \right)_{Ref}$. Selected data has been normalized using the relative atomic sensitivity factors (B 1s = 0.13, C 1s = 0.25, N 1s = 0.42) [28] to show more clearly the B:N atomic ratio in each deposited film

3.4 Results

In-situ XPS was used to observe the effects of hydrogen gas flow rates on the growth of c-BN films on diamond using PECVD and fluorine chemistry. A hydrogen flow of 4 sccm was used to replicate previous work from our group using a similar growth process [36] [49]. An initial hydrogen plasma (parameters in Table 2) was used to remove air adsorbates and surface oxygen for each polycrystalline boron-doped diamond substrate.

The XPS of the clean diamond is shown in Figure 20 scan (i), and the C 1s peak is centered at 284.1 eV. This peak position is consistent with the C 1s for hydrogen terminated boron-doped diamond [32] [50]. The hydrogen terminated diamond is then exposed to the ECR PECVD with the deposition parameters from Table 2, with the hydrogen flow turned off ($H_2 = 0$ sccm), shown in Figure 20 scan (a). The C 1s peak significantly broadens relative to the initial C 1s peak. The deconvolution of this peak shows two main components, one peak centered at 285.2 eV which corresponds to the C 1s peak of the nitrogen terminated boron doped diamond [50], and the other peak at 284.2, which still corresponds to the C 1s of the hydrogen terminated diamond.

The XPS data presented in Figure 20 (and Figure 21) have been normalized using the atomic sensitivity factors (B 1s = 0.13, C 1s = 0.25, N 1s = 0.42) [28] to show more clearly the B:N atomic ratio for the deposited films. In Figure 20 scan (a), notice that the N 1s peak is about twice as intense as the B 1s peak, and therefore indicates twice as much nitrogen as boron. Assuming that the deposited BN is above the nitrogen terminated diamond, and not the hydrogen terminated diamond, the peak centered at 285.2 eV is used to calculate the c-BN thickness. As deduced from the C 1s core level

peak at 285.2 eV, a thin layer of boron nitride was deposited, with a thickness of $\sim 0.3 \pm 0.1$ nm, suggesting that hydrogen is not required to nucleate c-BN on diamond.

The $H_2 = 0$ process used in Figure 20 (a) was further investigated on a fresh hydrogen terminated boron-doped polycrystalline diamond substrate where the process time was increased from 10 minutes to 100 minutes. No change in the C 1s peak and no change in the film thickness was observed between the two samples with greatly different process times. The results suggest that hydrogen is not necessary for c-BN nucleation, but continued growth is not sustained in the absence of hydrogen.

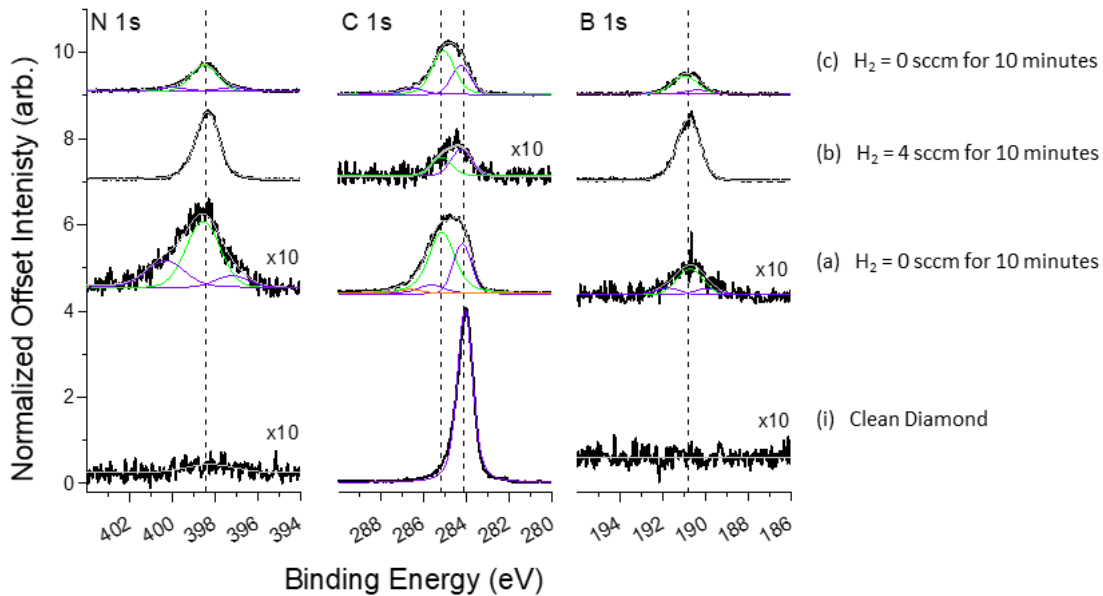


Figure 20 An evolution of the N 1s, C1s and B1s core energy levels. The data has been normalized to the clean diamond peak intensity, and with the corresponding ASF to better view the relative concentration of each element. (i) Initial Hydrogen plasma cleaned boron doped diamond (a) 10 minutes with $H_2 = 0$ sccm, followed by (b) 10 minutes with $H_2 = 4$ sccm, followed by (c) 10 minutes with $H_2 = 0$ sccm. Results show how hydrogen can be toggled to either grow or etch BN.

The sample with 0.3 nm of BN from Figure 20 scan (a) was then exposed to the PECVD deposition with the hydrogen flow on ($H_2 = 4$ sccm). The XPS results are shown

in Figure 20 scan (b). The peak area of the C 1s core level centered at 285.2 eV was used to calculate a BN film thickness of ~ 8.8 nm.

The process with $H_2 = 0$ sccm was then repeated on the 8.8 nm BN layer sample from Figure 20 scan (b). The XPS scans in Figure 20 scan (c) indicate that the BN layer was etched down to ~ 1.7 nm during the process. This result indicates that the hydrogen gas concentration is a critical parameter which controls the reaction equilibrium between growth and etching.

These results point toward controlling the equilibrium between growth and etching by tuning the hydrogen concentration. Tuning the hydrogen flow such that the etching rate of h-BN is greater than the growth rate, is a strategy to produce an improved c-BN/diamond interface.

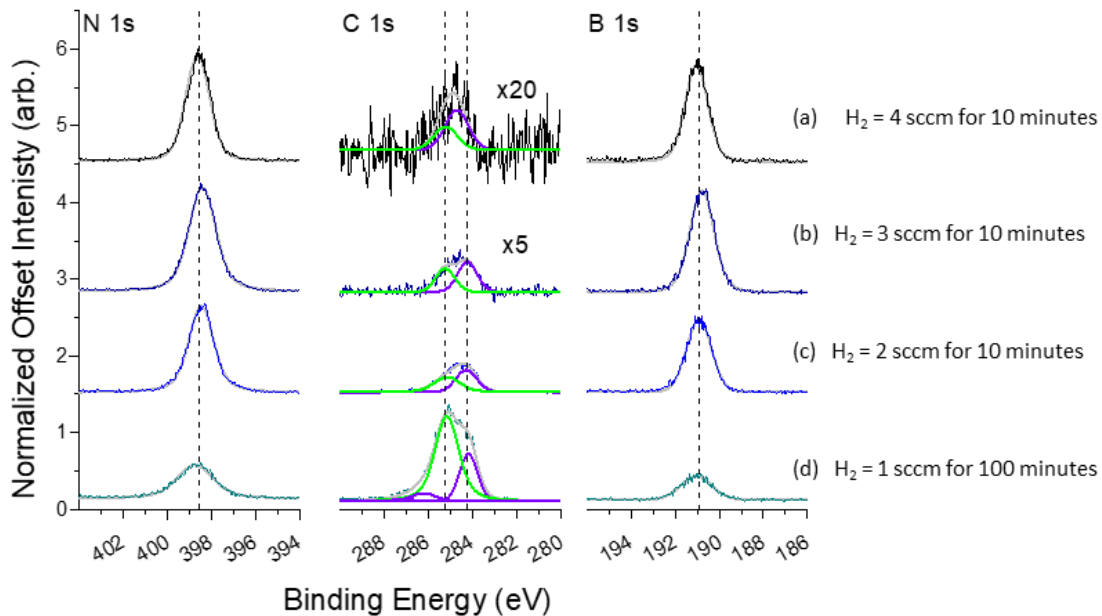


Figure 21 The Nitrogen, Carbon, and Boron 1s core level peaks for different H_2 flow rates: (a) $H_2 = 1$ sccm for 100 minutes (b) $H_2 = 2$ sccm for 10 minutes (c) $H_2 = 3$ sccm for 10 minutes (d) $H_2 = 4$ sccm for 10 minutes. Showing that hydrogen can control the reaction rate.

To determine the optimum hydrogen concentration for epitaxial c-BN on diamond, fresh boron-doped polycrystalline substrates were cleaned and exposed to the ECR PECVD deposition parameters in Table 2 with different hydrogen flow rates (Figure 21). The BN layer thickness is calculated [27] from the carbon core level peak, and an increased growth rate is found with an increased hydrogen flow, shown in Figure 22.

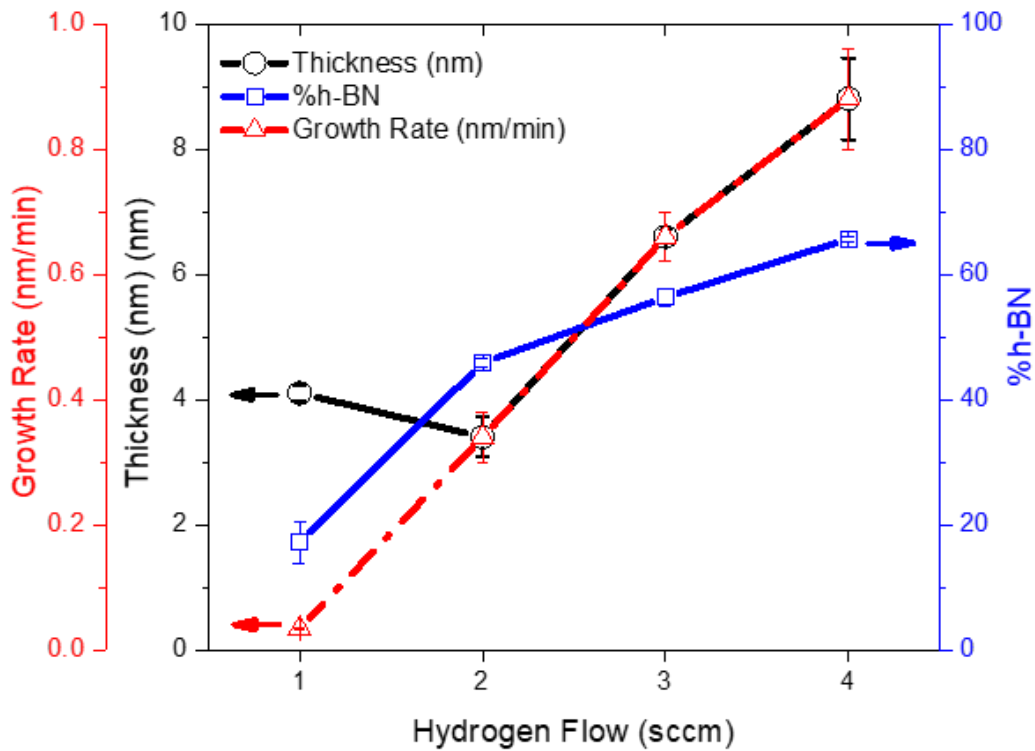


Figure 22 Growth Rates, Thickness, and %h-BN as a function of hydrogen flow rates. Note the correlation between growth rate and %h-BN

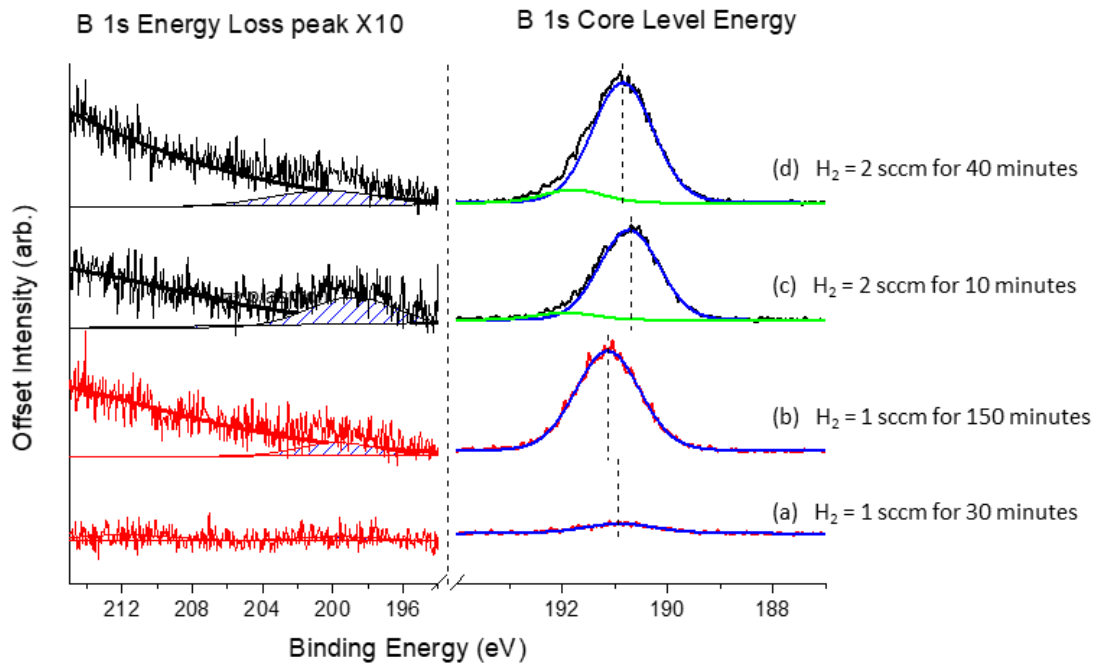


Figure 23 The B 1s core level (right) and enlarged π -plasmon energy loss peak spectrum (left) for BN deposition using limited H₂ flow for (a) 30 minutes and (b) for 150 minutes and using excess H₂ flow for (c) 10 minutes and (d) 40 minutes. The deposition with a limited H₂ flow results show a reduced π -plasmon energy loss peak.

A closer investigation into the films grown using hydrogen gas flows of H₂ = 1 sccm, and H₂ = 2 sccm are shown in Figure 23. The characteristic π -plasmon peak centered at ~200 eV, corresponding to π bonding in h-BN, is emphasized within Figure 23. The deposition with H₂ = 2 sccm shows an initial π peak at the interface (Figure 23 scan (c)) that is relatively reduced with increased film thickness (Figure 23 scan (d)). By reducing the hydrogen flow to H₂ = 1 sccm, Figure 23 scan (b), a film with similar thickness to Figure 23 scan (c) was deposited, with a greatly reduced π -plasmon peak.

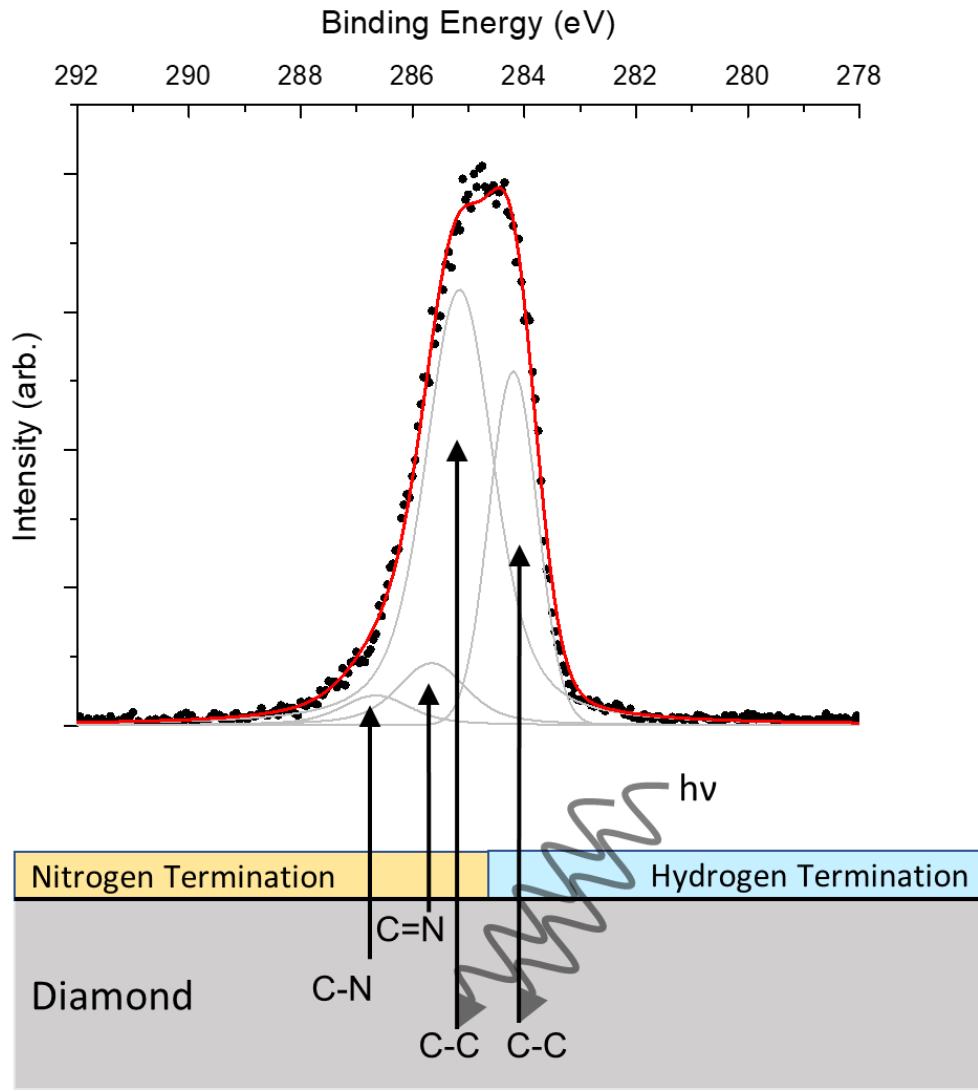


Figure 24 Example double carbon peak from (data from Figure 20 scan (a)). The C 1s core level energy from the hydrogen terminated surface (284.2 eV) and the C 1s core level energy from the nitrogen terminated diamond surface (285.2 eV). This non-uniform surface shows the difference in band bending between the nitrogen terminated and hydrogen terminated surfaces of diamond. The two small peaks to higher binding energy can be attributed to carbon nitrogen bonding near the surface.

Using a hydrogen flow of $H_2 = 1$ sccm for a deposition time of 30 minutes, and 150 minutes produced BN films of ~ 0.6 nm and ~ 4.1 nm respectively. A continuous growth is observed for the depositions using a hydrogen flow of $H_2 = 1$ sccm, as

compared to depositions with hydrogen flow of $H_2 = 0$ sccm, which did not maintain a continuous growth, and in fact etched the BN film as discussed previously.

3.5 Discussion

An unusual aspect of the XPS scan is the shape of the C 1s peak after the initial BN growth process. A double carbon peak is most distinct in Figure 21 scan (d) but is also clearly resolved in Figure 20 scan (a), Figure 20 scan (c), Figure 21 scan (b), Figure 21 scan (c). Hydrogen terminated boron doped diamond is known to have a C 1s core level energy of 284.1 eV [50] [32] [51]. Nitrogen terminated boron-doped diamond has a C 1s core level energy of 285.2 eV [50]. Previous reports of nitrogen terminated diamond indicate that the C 1s peak shift is due to both surface band bending, and chemical shifts [52].

For thin layers of BN, both hydrogen-terminated, and nitrogen-terminated C 1s core level energy peaks are observed in the deconvoluted fit peak. A representation of the various diamond terminations, and the bonding configurations of the carbon within is shown in Figure 24. Minor peaks can be attributed to chemical shifts of subsurface carbon nitrogen bonds C—N and surface carbon bonds (C==N, and C—H_x) [50] [52].

For sub-nanometer BN layers (see Figure 20 scan (a), Figure 21 scan (d)) the atomic ratio of boron to nitrogen (B:N) is consistently nitrogen rich (B:N < 0.5). The nitrogen termination of the diamond surface would shift the B:N ratio to nitrogen rich values. The XPS data presented in Figure 20 and Figure 21 have been normalized using the atomic sensitivity factors (B 1s = 0.13, C 1s = 0.25, N 1s = 0.42) [28] to visually display the atomic ratios for each process. Assuming the BN formation is occurring

above the nitrogen terminated surface, the peak at 285.2 eV is used to calculate the BN thickness. While the peak at 284.2 eV is used to calculate the % of the substrate that has either nitrogen termination, or BN growth. The growth rates, and thicknesses of each process with a different hydrogen gas flow is shown in Figure 22.

Hydrogen is a key component in the proposed BN growth mechanism. The plasma formation of NH_x and BF_x species then react on the substrate surface to form solid BN and molecular HF [21]. From the results shown in Figure 20, the PECVD process was performed while the hydrogen gas was turned off ($\text{H}_2 = 0$ sccm), then on ($\text{H}_2 = 4$ sccm), and then off again ($\text{H}_2 = 0$ sccm). When hydrogen was not used during the PECVD process, the BN thin film was etched. This result confirms that hydrogen enables deposition of BN using PECVD with employing fluorine chemistry.

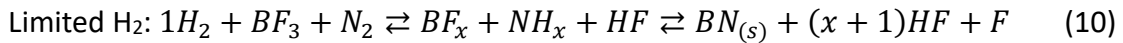
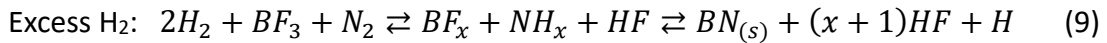
Increasing the hydrogen flow from 0 sccm to 1 sccm causes the surface chemistry to switch from etching to growth. Increasing the hydrogen further from 1 sccm to 2 sccm results in an increased the growth rate, and this trend is continued for hydrogen flows of 3 sccm and 4 sccm (Figure 22). One conclusion that can be made from this PECVD experiment is that hydrogen gas flow can be used to control the nucleation and growth rate of BN.

Another trend that is observed is the correlation between the growth rate, and the fraction of h-BN observed in the film. For higher growth rates, the deposited film showed a greater fraction of h-BN. For lower growth rates, the relative growth of c-BN was favored, see Figure 22 and Figure 23.

A deposition with a limited hydrogen gas flow ($\text{H}_2 = 1$ sccm) produced a 4.1 nm film, and a small π -plasmon peak (Figure 23 scan (b)), which corresponded to 17% h-BN.

The results indicate that most of the deposited film is c-BN. A deposition with an excess hydrogen gas flow ($H_2 = 2$ sccm) produced a 3.4 nm film with the characteristic π -plasmon peak (Figure 23 scan (c)) that corresponded to 62% h-BN. Previous reports of BN thin films deposited using PECVD with excess hydrogen gas flow produced 4.3 nm films with 68% h-BN [49]. The limited hydrogen gas reaction appears to emphasize the formation of c-BN during nucleation on boron doped polycrystalline diamond.

If an excess of hydrogen is supplied during the deposition, the excess hydrogen at or near the surface may reduce the effectiveness of fluorine chemistry to selectively etch the h-BN. This trend is evident in the balanced chemical equation (8), which describes the growth mechanism proposed by W.J. Zhang and colleagues. Assuming excess N_2 , the addition of hydrogen will reduce the concentration of atomic fluorine in the plasma, as indicated in equation (9). Reducing the hydrogen flow such that hydrogen is the limiting reactant increases the relative concentration of atomic fluorine, as indicated in equation (10). A higher concentration of atomic fluorine increases the etching efficiency of h-BN, and enables the formation of higher purity c-BN.



The concentration of H_2 gas during growth has several effects, not only in the chemistry above the surface creating the active growth species [21] [22], but also within the film [47]. As NH_x is a key component of the growth mechanism, the incorporation of

hydrogen defects during PECVD of BN is not unlikely. If a higher hydrogen gas flow is used during BN growth, the reaction rate could be sufficiently high that H incorporation occurs through incompletely reacted NH_x . In this scenario the incorporation of hydrogen defects occurs during the growth.

Theoretical research suggests that the hydrogen defects in h-BN form between layers with minimal distortion of the local structure [47]. In contrast, hydrogens defect in c-BN form along the B—N bond center which forces the tetrahedral structure to distort toward a more trigonal pyramid structure. The incorporation of a hydrogen defect during the nucleation of c-BN is modeled in Figure 25. A hydrogen atom placed along a B—N bond center increased the B—N bond length by 52% [47] and changes the nearest neighbor bonding angles from tetrahedral 109° to anisotropic 119° and 94.5° . This model suggests that the incorporation of hydrogen defects during the nucleation of c-BN may create nucleation points for h-BN growth.

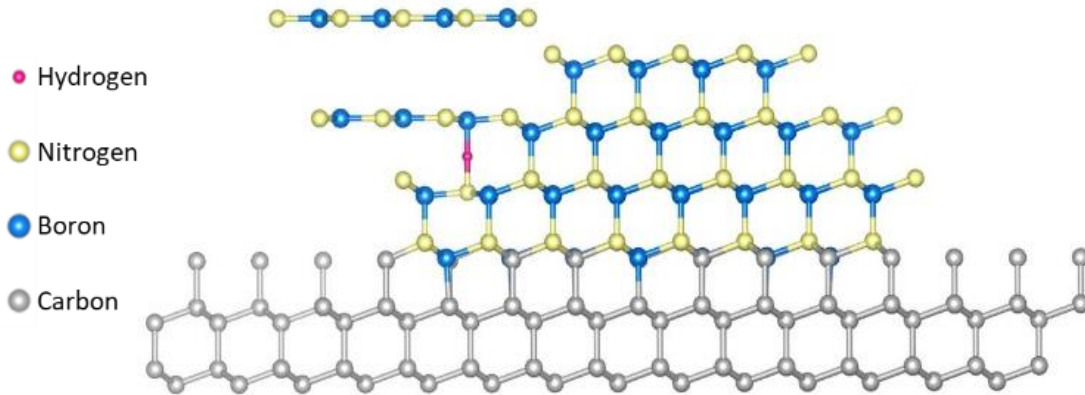


Figure 25 Model of hydrogen defect in c-BN nucleation for the (111) interface. The extra enthalpy causes the N—B bond to increase in length, changing the nearest neighbor bonding angle from isotropic 109° to anisotropic 119° and 94.5° . If excess hydrogen is used during the deposition an extra hydrogen may get trapped during the growth process. This may provide a nucleation point for h-BN.

While the incorporation of hydrogen defects can distort the c-BN to h-BN and can stabilize the h-BN structure, hydrogen appears to be necessary for continued growth. This effect may be anticipated as hydrogen gas enables the formation of NH_x according to the growth mechanism [21] [22]. In the above chemical equations, the difference between excess hydrogen and limited hydrogen is a relatively small change in the H_2 gas phase concentration. For the reaction with a limited hydrogen flow, one would expect to have excess fluorine, which reacts with h-BN as it is forming, breaking the sp^2 bond before it becomes buried, as less hydrogen also decreases the growth rate. Limiting the hydrogen will also minimize the concentration of hydrogen defects in BN thin films. With excess hydrogen gas, the formation of hydrogen defects will become more likely. The increased hydrogen defects would likely react with the fluorine and leave the h-BN unaffected.

3.6 Conclusion

The effects of hydrogen gas concentration during the growth of boron nitride using ECR PECVD with fluorine chemistry was investigated. To find the optimum concentration of H_2 for the growth of c-BN, the hydrogen gas flow was varied (0, 1, 2, 3, 4 sccm), while keeping constant temperature, pressure, bias, and other gas flows. This experiment found that hydrogen is a necessary reactant, as continuous growth was not observed in the absence of hydrogen. The growth rate of the BN film can be controlled by tuning the hydrogen to fluorine ratio. The hydrogen flow rate can also be used to select between h-BN and c-BN. Excess hydrogen will favor the growth of h-BN, while limited H_2 will favor the growth of c-BN. The growth mechanism [21], selective etching with fluorine, and incorporation of hydrogen defects [47] are used to discuss the role

hydrogen has on the structural phase of the deposited boron nitride film. Comparing the results with excess hydrogen gas and limited hydrogen gas we can conclude that limiting the hydrogen gas flow provides a more favorable environment for c-BN nucleation and growth.

4 VALENCE BAND OFFSET OF CUBIC BORON NITRIDE ON (100) BORON-DOPED DIAMOND

4.1 Abstract

There is substantial interest in the diamond/c-BN interface, especially regarding high power electronics, as both c-BN and diamond are ultra-wide band gap materials with superb thermal conductivity. Accurate knowledge of the valence band offset is needed for device design and modeling. The valence band offset (VBO) of boron nitride (BN) on boron-doped (100) diamond substrate is presented in this paper. In-situ X-ray photoelectron spectroscopy (XPS) and ultra-violet photoelectron spectroscopy (UPS) were used to measure the VBO across the interface. These experimental results find that the c-BN valence band maximum (VBM) is ~ 0.3 eV below the diamond VBM. The results presented here are compared with prior measurements of the VBO of c-BN on nitrogen-doped diamond and with theoretical calculations.

4.2 Introduction

Demand for high-power electronics has prompted a significant increase in research on wide band gap semiconductors. High power electronic systems generate substantial heat that require carefully designed thermal management systems with high thermal conductivity materials. Diamond is known to be the highest thermally conductive material (22-30 W/cm/K) [10], with cubic boron nitride (c-BN) second (13-16 W/cm/K). Hexagonal boron nitride (h-BN) is another well-known allotrope of boron nitride, with moderate thermal conductivity (4 W/cm/K) [8], [53].

Wide band gap semiconductors are a key component in the design of high-power electronics. Diamond, with a cubic structure of carbon atoms, has an indirect band gap of ~5.5 eV. Similar to diamond, c-BN has a cubic zinc-blend structure and an indirect band gap of ~6.4 eV. The structure of h-BN is very similar to graphite, with alternating boron and nitrogen atoms in a honeycomb layered structure, with weak bonding between layers. However, unlike graphite, which can be conducting, h-BN has a large indirect band gap (~5.2 eV). [54] [55] The direct band gap of h-BN have been reported to be 5.97 eV, indicating potential application for UV laser diodes [56] [57].

Using an electron cyclotron resonance plasma enhanced chemical vapor deposition system (ECR PECVD), both films with c-BN and h-BN structures can be deposited in the same chamber. Depending on the gas phase precursors and system operation conditions h-BN, c-BN, or a mixed phase of h-BN and c-BN can be deposited. Specifically, varying the hydrogen flow from a limiting reactant, or providing excess hydrogen will produce either c-BN, or h-BN respectively. This is discussed in detail in Chapter 3. With high thermal conductivity, thermal stability, oxidation stability up to 1200°C, and its wide band gap, both c-BN and h-BN are ideal materials for high power, high temperature applications. Hexagonal BN layers grown by ECR PECVD have performed well as the dielectric for GaN transistors, showing a breakdown voltage (8.4 MV/cm) [44]. Monocrystalline h-BN as a gate dielectric on a diamond field effect transistor (FET) performed with unprecedentedly high carrier mobility ($> 300 \text{ cm}^2 \text{ V}^{-1} \text{ s}^{-1}$) for moderately high carrier densities ($> 5 \times 10^{12} \text{ cm}^{-2}$). [58] Cubic BN has been shown with both p-type and n-type doping and could potentially support high power diodes or transistor operation. [4] [16]

Among the most important physical parameters for heterojunction device designs are the conduction and valence band offsets. [59] Energy band offsets occur at the interface and are due to interface bonding. Several theoretical calculations have investigated the VBO of (100), (110), and (111) diamond/c-BN interfaces. A wide range of VBO values were calculated for different interface orientations, and different interface bonding configurations. A summary of the reported VBO of diamond/c-BN interface is shown in Table 3.

The ideal (110) interface has an equal number of C—B and C—N bonds. The C—B bond is unsaturated with only 1.75 of the 2 electrons necessary to saturate a sp^3 bond, while the C—N bond is supersaturated with 2.25 electrons. However, the bonds are very close and charge transfer occurs until both bonds are effectively saturated resulting in a net neutral interface. [60] [61] The VBO of the abrupt(110) diamond/c-BN interface was calculated to be -1.4 eV [62], [63].

For (100) and (111) orientations, the interface can have either C—B or C—N bonding. Since the C—B bond is unsaturated (B has one less electron than C) and the C—N bond is supersaturated (N has one more electron than C) both bonding configurations create a polar interface. The calculated VBO of the (111) C—N interface is (+0.587 eV), while with C—B interface bonding, the VBO is (-0.045 eV) [64]. The calculated VBO of the (100) C—N interface is (-0.13 eV), while with C—B interface bonding the VBO is (-2 eV) [65]. A recent report from our group measured the VBO of polycrystalline N-doped diamond/c-BN interface to be (+0.8 eV). TEM data showed the

(111) plane of diamond parallel to the (111) plane of c-BN [49]. Here negative values of the diamond/c-BN VBO imply that the diamond VBM is above the BN VBM.

Surface band bending occurs due to electric fields in the semiconductor material. Surface band bending deduced from the difference of the surface Fermi level and the bulk VBM. When measuring the VBO of a heterojunction, the VBM of the substrate can shift due to band bending, which needs to be considered when determining the band offset from photoemission measurements. Moreover, the heterojunction band offset can depend on the detailed conditions under which the interface was prepared.

Band bending of both nitrogen-doped, and boron-doped (100) diamond has been previously studied using XPS and UPS. [66] [32] Nitrogen-doped diamond, after annealing a hydrogen terminated surface to 400°C, indicated a VBM at ~2.2 eV below the surface Fermi level. The bulk VBM of nitrogen-doped diamond is reported at ~3.9 eV. Considering both results an upward band bending of 1.7 eV was deduced. [32] Hydrogen terminated polycrystalline nitrogen-doped diamond VBM at ~2.5 eV below the surface Fermi level was very similar to that of the single crystal (100) nitrogen-doped diamond [Diederich et al.]. [32] [49] Surface state pinning is said to cause the 1.7 eV upward band bending in nitrogen-doped diamond. [32] Boron-doped diamond has a bulk VBM of ~0.3 eV, and a hydrogen terminated surface VBM of 0.6 eV, in agreement with our results. The downward band bending may be attributed to pinning the same surface state. Nitrogen-termination lightly boron-doped diamond results in deep downward band bending with a surface VBM of ~ 1.6 eV. below the Fermi level [50]

In this study BN is deposited on single crystal 5° offcut (100) boron doped diamond via electron cyclotron resonance plasma enhance chemical vapor deposition (ECR-PECVD). In-situ photoelectron spectroscopy is used to measure the core energy level and valence band maximum of the initial substrates, and after the BN deposition to deduce the valence band offset of the diamond/BN heterojunction.

4.3 Experiment

Boron-doped single crystal 5° offcut (100) diamond plates (doping concentration $[B] = 1-2 \times 10^{20} \text{ cm}^{-3}$; 3mm x 3mm x 0.3mm; supplied by TISNCM) were used to as substrates for the deposition of boron nitride thin films of various thicknesses. In-situ photoelectron spectroscopy of core levels, and valence band spectra were measured to determine the VBO between the boron-doped diamond and BN layer.

The diamond substrates are placed in an acid mixture ($\text{H}_2\text{SO}_4 / \text{H}_2\text{O}_2 / \text{H}_2\text{O}$, 3:1:1) at 220 °C for 15 min, then dipped in an HF treatment for 5 min. The substrate was boiled again in ($\text{NH}_4\text{OH} / \text{H}_2\text{O}_2 / \text{H}_2\text{O}$, 1:1:5) at 75 °C for 15 min. After each step the substrate was rinsed with DI water. This wet chemical process is used to clean the as-received diamond substrates of graphitic carbon and other surface contaminants.

Individual substrates were mounted on a nichrome plate using tantalum wires to bind two opposite corners of the substrate to the plate. Optical profilometry (using a Zygo “model”) was used to measure the surface topography of the initial substrate and an RMS of ~2 nm was measured. After cleaning and mounting, each diamond sample was placed into a load locked transfer line, which is part of an integrated vacuum system with a base pressure of $5 \cdot 10^{-9}$ Torr. Thus, the sample maintains the clean surface or the growth

surface during in-vacuo transfer between the boron nitride deposition chamber and the surface characterization chamber.

An electron cyclotron resonance (ECR) microwave plasma chemical vapor deposition (ECR MP CVD) chamber (base pressure $3 \cdot 10^{-9}$ Torr) was used for cleaning the substrate with a hydrogen plasma and for the deposition of boron nitride. The hydrogen plasma cleaning process is initiated by heating the substrate to 825°C and remaining at this temperature for 20 minutes in UHV ($\sim 5 \cdot 10^{-9}$ Torr) to thermally remove surface oxygen. After which a hydrogen flow of 20 sccm is introduced to the chamber at a pressure of $\sim 2 \cdot 10^{-4}$ Torr. The substrate is then cooled to 750°C , as the lower temperature is more conducive to hydrogen termination. The plasma is ignited and sustained with ~ 300 W of microwave power for 5 minutes. The microwave power is then turned off, and the sample is cooled to ambient temperature in a hydrogen gas flow. The chamber is then pumped to UHV, and the sample is then transferred to the XPS/UPS chamber.

UPS measurements use a helium discharge lamp as the ultra-violet light source. A small bias of 1.5V is applied to the substrate, and an energy offset of 2.7 eV is input into the software, for a total of 4.2 eV to accommodate for the work function of the analyzer. The hemispherical analyzer is operated with a pass energy of 2 eV with a resolution of less than 10 meV. The UPS system has been calibrated to the Fermi edge of plasma cleaned a e-beam deposited gold calibration sample. The work function of each sample before and after BN deposition is measured using the 21.2 eV He line and, the valence band spectra is measured using the 40.8 eV He line.

For XPS measurements using a monochromatic Al-K α X-ray (1486.6eV \pm 0.2eV) source is used. The hemispherical analyzer is operated with a pass energy of 100 eV with a resolution of 150 meV. No bias or energy offset is applied to the sample during XPS. The same gold calibration sample used to calibrate the UPS was used to calibrate the XPS. The Au 4f_{7/2} peak was measured to be 83.98 \pm 0.01 eV, and the Fermi edge was measured to be -0.06 \pm 0.03eV (see Figure 13 in Chapter 2.3.2). The Fermi edge of the gold sample measured using UPS and XPS were identical (see Figure 14 in Chapter 2.3.2). The C 1s, B 1s, N 1s, and F 1s core level peaks are measured on each sample before and after BN deposition

The deposition of boron nitride is initiated by heating the substrate to 850°C in UHV and remaining at this temperature for 20 minutes to allow for thermal equilibrium of the substrate and holder. The precursor gas flows are then introduced to the chamber (He: 36 sccm, Ar: 2.5 sccm, N₂: 12.5 sccm, BF₃: 1 sccm, H₂: 1 sccm) at a pressure of $\sim 2 \cdot 10^{-4}$ Torr. A bias of -60V is applied to the sample relative to the chamber walls. At this point, the plasma is ignited, and sustained with ~ 1400 W of microwave power for 30-120 minutes, after which the microwave power is turned off, and the sample is cooled in vacuum to ambient temperature. The chamber is then pumped to UHV, and the sample is transferred in-situ to the XPS/UPS chamber. The thickness is measured using the method described by A. Jablonski and J. Zemek. [27] The following equation is used to calculate the thickness of the deposited layer

$$t = \lambda \cdot \ln \left(\frac{I_{C1s}^S}{I_{C1s}^0} \right) \quad (11)$$

The term $\left(\frac{I_{C1s}^S}{I_{C1s}^0}\right)$ is the ratio of the integrated C 1s core level intensity of the clean substrate and the C 1s intensity after the overlayer is deposited. The term λ (2.00 nm) is the inelastic mean free path of C 1s electrons from an Al-K α source through c-BN. [48] After the final XPS measurement the sample is subsequently removed from the transfer line and the cross section of the BN/diamond interface was studied using transmission electron microscopy (TEM).

Some unexpected experimental issues occurred when depositing BN on single crystal substrates that resulted in non-ideal interfaces, and disorder in the BN layer, as seen in Figure 34. A silicon wafer had broken and dropped to the bottom of the chamber and was being etched during the BN deposition process. XPS measurements show there was an unintentional incorporation of silicon in the thick BN film 17nm thick.

The broken silicon wafer was removed from the chamber and the quartz window was cleaned. The clean quartz window also introduced silicon impurities in the films until the window was coated with a sufficiently thick layer of BN which required many hours (> 10 hours) of deposition. For the sample with 1.1 nm epitaxial c-BN on (100) diamond the chamber was finally in good working order, without silicon incorporation observed in the XPS. Unfortunately, this was the last deposition performed in this set of experiments.

4.4 Results

The combined XPS and UPS results are presented for the initial boron-doped diamond substrates, and for various thicknesses of boron nitride. The photoelectron emission features are presented relative the Fermi level. The initial diamond substrates C 1s core level and valence band spectra are used to deduce the electron affinity of the surface. The electron affinity is defined as the energy difference between the conduction band minimum (CBM) and the vacuum energy level. Following the results and discussion on the initial boron doped diamond substrates, the XPS/UPS results of increasing thickness of BN layers introduced and discussed. Energy level diagrams are used to represent the measured spectra, followed by the VBO calculation of the diamond/c-BN interface. The results presented here are compared with previous experimental reports of the diamond/c-BN offset, as well as theoretical calculations.

Hydrogen plasma cleaned single crystal (100) boron-doped diamond C 1s core level, VBM, and work function are shown in Figure 27. Each of the five independent substrates show a C 1s core level energy centered at 284.2 eV, with a VBM varying from 0.7 eV to 0.3 eV below the Fermi level. The VBM is deduced by linear fit of the low binding energy cut off and a linear fit to the background noise for energies above the Fermi level. The intersection of these two lines is interpreted as the VBM.

Hydrogen terminated diamond is known to have a negative electron affinity (NEA), where the vacuum level is below CBM. The electron affinity (χ) is the difference between the CBM and the vacuum energy level (E_{vac}). Defining the VBM as the binding energy relative to the surface Fermi level, the electron affinity (χ) plus the band gap (E_g)

is equal to the work function (ϕ) plus the VBM as seen in Figure 26. The He I α spectra can be used to deduce the electron affinity and to determine the presence of a NEA is often achieved by evaluating the following equation: [66]

$$\chi = h\nu - E_g - W \quad (12)$$

Where W is the width of the valence band spectra ($W = S_{\text{cutoff}} - \text{VBM}$) and S_{cutoff} is the secondary electron cutoff. The He I α spectra is often displayed as a binding energy (E_B), or equivalently, the energy below the Fermi level. When presenting the He I α spectra this way the secondary electron cutoff (S_{cutoff}) is located at high binding energies typically \sim 14-17 eV for a photon energy of 21.2 eV. When the He I α spectra is presented as binding energy (E_B) the work function is not directly apparent, and to deduce the work function the photon energy needs to be subtracted from the sharp secondary cutoff ($\phi = S_{\text{cutoff}} - h\nu$).

Some reports display the He I α as “kinetic energy relative the Fermi level”. [66] [32]. However, the vacuum level is defined as the energy for which an electron has zero kinetic energy outside the surface of a material. The He I α spectra in Figure 27 and Figure 29 are presented as “Energy Relative to Fermi Level”. This is done by subtracting the raw data by the He I α energy (21.2 eV) ($E_B - h\nu = E - E_F$). When presented this way, the work function (ϕ) or effective work function (ϕ^*) is more apparent. However, the energy relative to the Fermi level is negative since the convention throughout this dissertation presents binding energy, equivalent to the energy below to the Fermi level with positive values. Therefore, the negative sign is simply a result of our reference energy being the Fermi level ($E_F = 0.0$ eV), and binding energy being positive.

When the vacuum level is above the CBM for a PEA, the true work function (ϕ) can be deduced. However, when the vacuum level is below the CBM for NEA, an effective work function (ϕ^*) is observed that corresponds to the CBM relative to the Fermi level instead of the vacuum level. Using the relations for the width (W) and work function (ϕ), then equation (12) can be rearranged to:

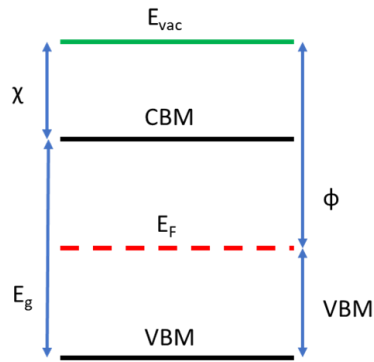
$$\text{For PEA: } \chi + E_g = VBM - \phi \quad (13)$$

$$\text{For NEA: } E_g = VBM - \phi^* \quad (14)$$

The value of ϕ or ϕ^* is the minimum energy above the Fermi level which a conduction band electron can escape the surface of the material. Since ϕ is presented as a negative value, the difference of the VBM and ϕ is a positive number. The results in Figure 27 show two sharp cutoff features. The sharp feature at 4.3 eV above the Fermi level is thought to be the vacuum level cutoff (E_{vac}). The second is the effective work function (ϕ^*) or conduction band minimum (CBM), with a cutoff at 5.3 eV above the Fermi level. The sharpest VBM cut off is located 0.3 eV below the Fermi level, so the CBM plus the VBM of this diamond sample gives 5.6 eV, which compared to the band gap of 5.5 eV appears to be a NEA, within the error of the measurements according to equation (14).

The average VBM of all five hydrogen terminated diamond surfaces is $\sim 0.5 \pm 0.2$ eV below the Fermi level, indicating small downward band bending of ~ 0.2 eV. The vacuum level, as indicated by the sharp feature within the bandgap, is measured to be 4.3 ± 0.2 eV above the Fermi level. The sum of these two values is 4.8 ± 0.28 eV. Since this is less than the bandgap of 5.5 eV the surface shows an NEA surface of -0.7 ± 0.28 eV.

Positive Electron Affinity



Negative Electron Affinity

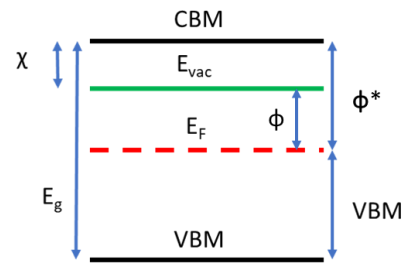


Figure 26 Schematic representation of the measured values to determine the electron affinity of a surface.

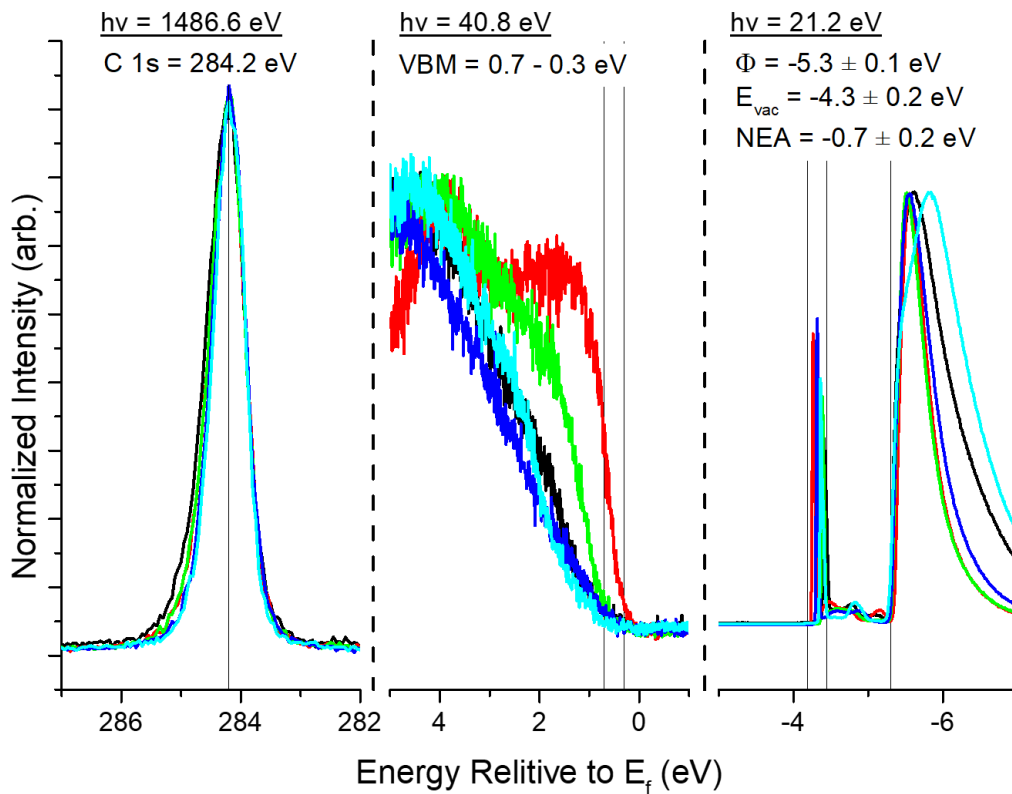


Figure 27 Initial (100) boron-doped diamond substrates after Hydrogen termination process. The C 1s energy of 284.2 eV, and an NEA of -0.7 eV was repeatable for all initial substrates.

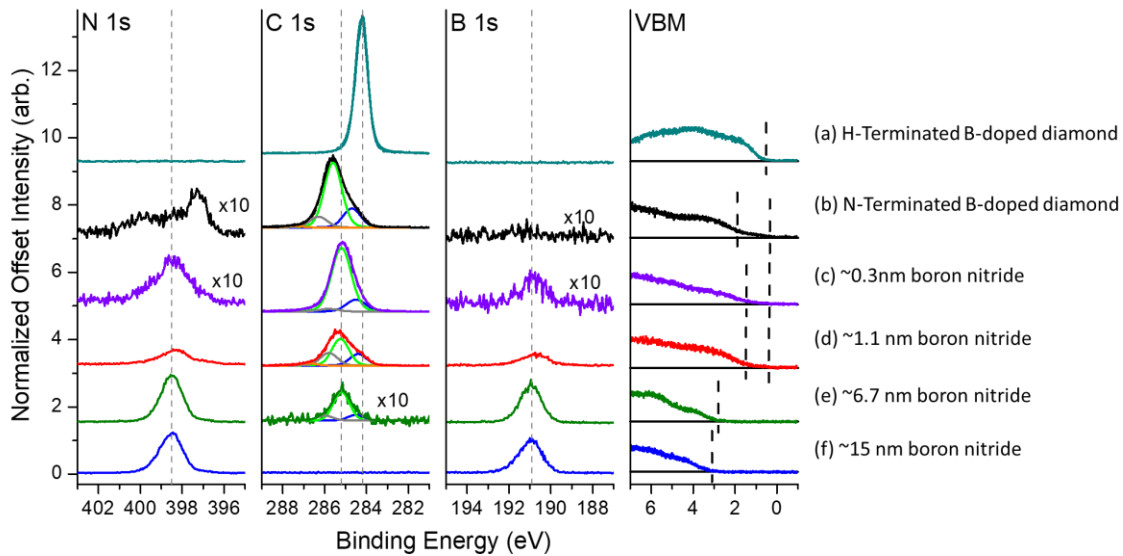


Figure 28 XPS of N1s C1s and B1s core levels, and VBM scan using He II α (40.8 eV). (a) Typical H-terminated boron-doped diamond (b) Nitrogen terminated surface (c) Nucleation of boron nitride. (d) Boron nitride ~1 nm thick, covering 70-80% of the diamond substrate (e) Boron nitride film ~ 6.7 nm thick (f) Thick boron nitride film (> 10 nm)

Boron nitride of various thicknesses was deposited on the five single crystal diamond substrates. The average thickness was determined by the change in the C 1s core level integrated intensity as discussed previously. The N 1s, C 1s, B 1s core levels presented in Figure 28 have been normalized to each substrate clean C 1s core level peak intensity, and each element's corresponding atomic sensitivity factor (N 1s = 0.42, C 1s = 0.25, B 1s = 0.13). [28] The data is normalized in this way to correct for small variations within the C 1s intensity that arise from the small sample size, and variations in the alignment of the XPS spot with the diamond substrate from sample to sample. The alignment before and after each deposition is well controlled and minimizes these small variations. The normalization using the elemental atomic sensitivity factor is so the data shows the relative concentration of elements in for each sample (i.e. the boron to

nitrogen ratio (B:N)). The UPS valence band spectrum has also been normalized to its maximum intensity such that the maximum intensity of the valence band spectra is one.

For the C 1s peak in Figure 28 scan (b), multiple deconvoluted C 1s peaks are evident at 284.6 eV and 285.6 eV. The peak centered at 284.6 eV corresponds to a bare boron-doped diamond surface, while the more intense peak centered at 285.6 eV corresponds to a nitrogen-terminated boron-doped diamond surface. [51] [67] The He II α spectra in Figure 28 scan (a) and Figure 29 scan (a) shows a clear sharp cut off for the VBM of the initial hydrogen terminated diamond surface. However, in Figure 28 scan (b) and Figure 29 scan (b) the VBM does not have a clear sharp cutoff. Instead, there is a high binding energy cut off at ~ 1.9 eV, and a long tail that extrapolates to $\sim 0.5 \pm 0.2$ eV. The extrapolated tale is in the range of the VBM of the initial hydrogen terminated boron-doped diamond. Additionally, a work function of 4.6 eV is evident in the He I α cut off in Figure 29 scan (b). A VBM of 1.9 eV and a work function of 4.6 eV results in a PEA of 0.9 eV, assuming the band gap of diamond to be 5.5 eV. Nitrogen terminated boron-doped diamond is expected to have a positive electron affinity (PEA). [67] The PEA is thought to be due to the Pauling electro negativity of carbon and nitrogen (2.55 and 3.04 respectively). The nitrogen termination shifts the C 1s core level to higher binding energy due to surface band bending. This is also evident in the shift of the VBM from 0.5 ± 0.2 eV to ~ 1.9 eV.

The absence of any observable boron in Figure 28 scan (b) indicates that prior to nucleation of BN, the diamond substrate is nitrogen terminated. The multiple core level components suggest the coverage is non-uniform. The energy level diagram for the hydrogen terminated and nitrogen terminated boron-doped diamond is shown in Figure 30.

The nucleation of BN is indicated by the presence of boron and nitrogen in Figure 28 scan (c). The C 1s core level observed in Figure 28 scan (c) is fit with two peaks. The most intense peak is centered at 285.2 eV, and the less intense peak is centered at 284.5 eV. Similar to the non-uniform nitrogen terminated surface, the presence of two C 1s peaks is interpreted as a non-uniform coverage of BN on the surface.

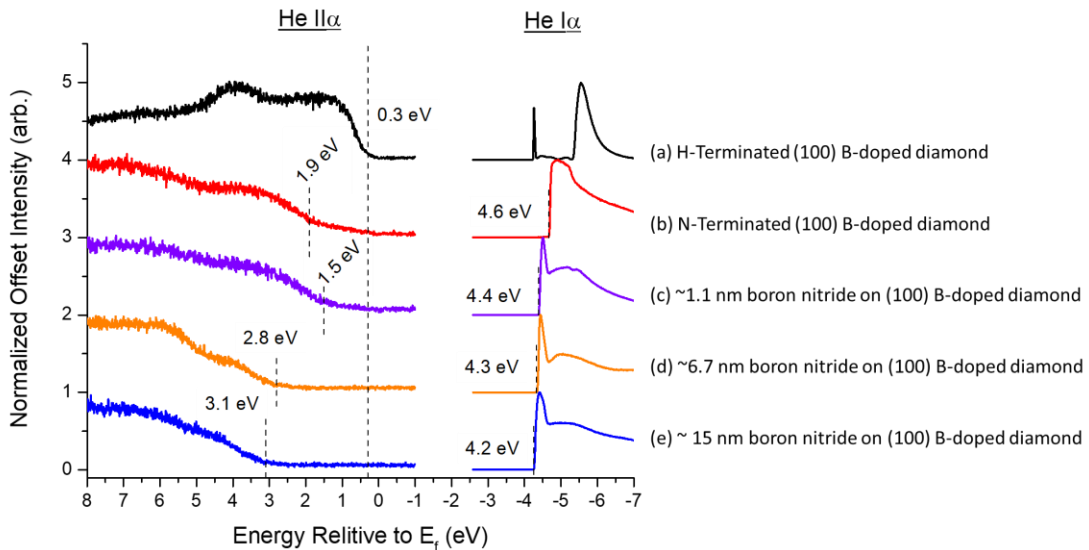


Figure 29 Valence band maximum measured with He II (40.8 eV), and work function measured with He I (21.2 eV), for (a) hydrogen terminated boron doped diamond, (b) Nitrogen terminated boron doped diamond. (c) Nucleation of BN (1 nm thick). (d) 6.7 nm of BN. (e) Thick layer (14-17 nm) of BN.

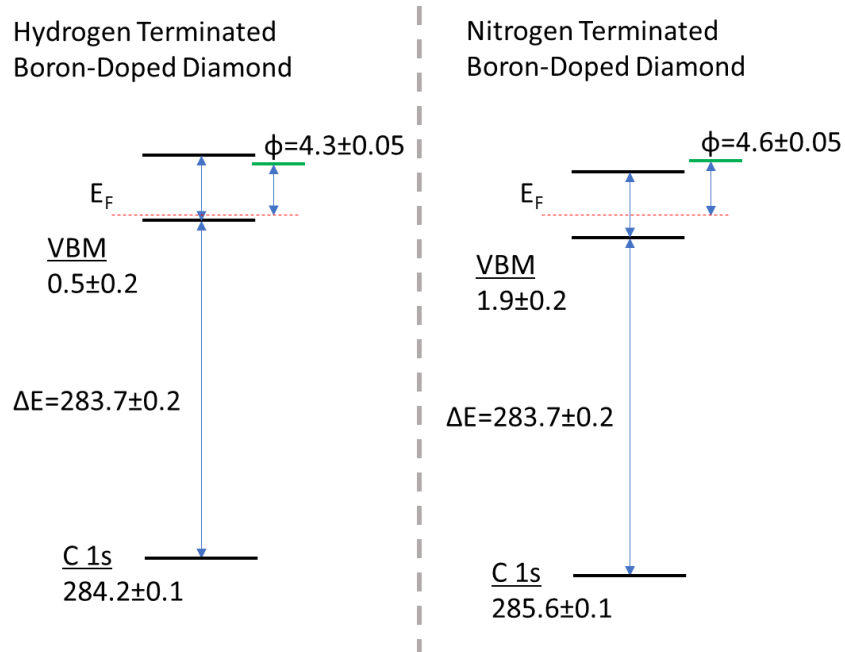


Figure 30 Energy level diagram of (left) hydrogen terminated boron-doped diamond, presented in Figure 28 scan (a) and Figure 29 scan (a). (right) Nitrogen terminated boron-doped diamond presented in Figure 28 scan (b) and Figure 29 scan (b)

For the 1.1 nm thick BN layer, the deconvoluted C 1s core levels in Figure 28 scan (d) positioned at 285.2 eV and 284.4 eV are effectively unchanged from Figure 28 scan (c). The thickness and the percentage of sp^2 bonding of this BN layer were determined to be 1.1 nm and 35% sp^2 by XPS and supported by TEM (Figure 32). For 35% sp^2 bonding, the majority of the film is inferred to be c-BN. The % sp^2 calculation is described in detail in Chapter 3.3. Also, silicon contamination was not observed by XPS for this sample. From the C 1s position the diamond VBM is determined to be 1.5 eV below the Fermi level after nucleation of c-BN. The B 1s and N 1s core levels have binding energies of 190.8 eV and 398.5 eV respectively.

Previous reports of the VBO of c-BN on nitrogen doped polycrystalline diamond report a difference of 189.0 eV and 396.8 eV between the B 1s core level and N 1s core level, with the c-BN VBM. [49] Using this difference in energy, the VBM of the c-BN is positioned at 1.8 eV below the Fermi level. The energy level diagram for the nucleation of 1.1 nm of c-BN on boron-doped diamond is shown in Figure 31.

The VBO (ΔE_V) of the interface can be deduced using the method presented by Waldrop, Kraut and Grant shown in equation 13. [68]

$$\Delta E_V = \Delta E_{CL} + (E_{CL} - E_V)_{Overlayer} + (E_{CL} - E_V)_{Substrate} \quad (13)$$

$$\Delta E_V = -0.3 \pm 0.24 = (94.4 \pm 0.1) + (189.0 \pm 0.1)_{c-BN} - (283.7 \pm 0.2)_{Diamond}$$

Where ΔE_{CL} is the difference between the C 1s core level, and the B 1s core level ($\Delta E_{CL} = E_{CL}(C\ 1s) - E_{CL}(B\ 1s)$). The result of ΔE_V shows the c-BN VBM to be within 0.3 eV of the diamond VBM. By comparison, the previously reported results of the VBO between c-BN and polycrystalline nitrogen-doped diamond was +0.8 eV, with the diamond VBM below the c-BN VBM [49]. The main difference between these two VBO measurements is the ΔE_{CL} . Results presented in this dissertation $\Delta E_{CL} = 94.4$ eV; Data presented by [Shammas et al.] $\Delta E_{CL} = 95.1$ eV

$$\Delta E_V = +0.8 \pm 0.17 = (95.1 \pm 0.1) + (189.0 \pm 0.1)_{c-BN} - (283.3 \pm 0.1)_{Diamond}$$

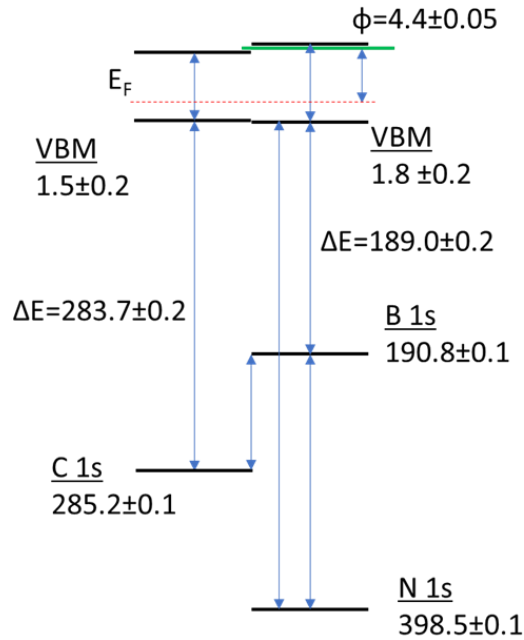


Figure 31 Energy band alignment of 1.1 nm of c-BN on (100) single crystal boron-doped diamond. Derived from data presented in Figure 28 scan (d) Figure 29 scan (c).

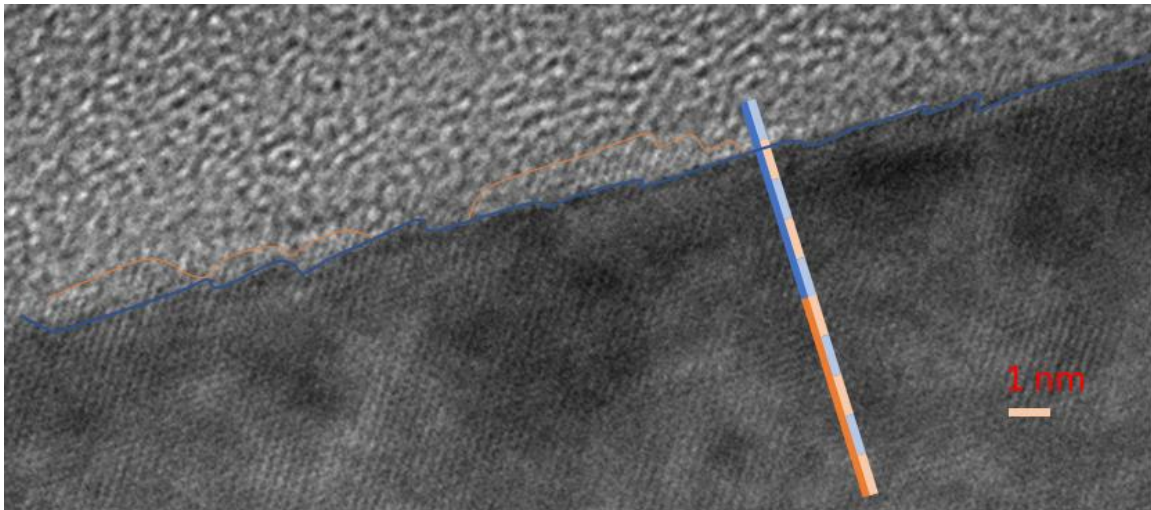


Figure 32 TEM of 1.1 nm of boron nitride on boron-doped diamond. Showing the nucleation of BN on the diamond surface, and the partial coverage of the substrate, also seen in the XPS peak analysis if Figure 28 scan (d), and Figure 29 scan (c).

TEM images were obtained after BN deposition and in-situ XPS/UPS measurements. The substrate surface shows a jagged interface (Figure 32). The nucleation of the c-BN appears to form within the corner of the diamond surface steps. The non-uniform coverage of the substrate evident in the deconvoluted C 1s core level peaks can also be seen in the TEM image Figure 32. The structure of this 1 nm layer appears to be epitaxial c-BN on (100) diamond.

For the 6.7 nm of BN on diamond, the BN VBM shifts further to ~ 2.8 eV, with no change in the C 1s, B 1s, or N 1s core level peaks, relative to the 1.1 nm of c-BN interface. The difference in VBM between Figure 28 scan (d) and (e) with no change in the core energy levels indicates that the two films have different chemical states. That is the 1.1 nm film in Figure 28 scan (d) is c-BN while the 6.7 nm film in Figure 28 scan (e) is h-BN. The percentage of h-BN was determined to be 86 % according to the B 1s π plasmon peak. A detailed description of the %h-BN calculations can be found in Chapter 3.3.

For the thick deposited BN film (14 - 17 nm), the VBM shifts further to 3.1 eV, and the C 1s peak is no longer visible. TEM images of the thick BN layer in Figure 34 indicate a disordered structure, often called turbostratic boron nitride. Silicon contamination is detected via XPS in this film with the Si 2p core level positioned at 102.5 eV. The XPS detection limit of a particular atomic species is $\sim 0.1\%$ of the total observable volume. For example, boron-doped diamond with a boron concentration of $1 \times 10^{20} \text{ cm}^{-3}$ the B 1s core level is not observable. Therefore, the observable silicon indicates that it is in concentrations greater than $1 \times 10^{20} \text{ (cm}^{-3}\text{)}$.

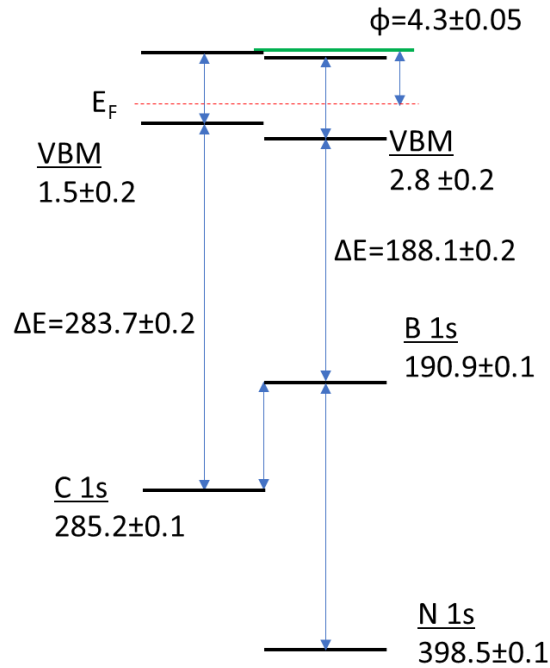


Figure 33 Energy level diagram for the 6.7 nm thick 86 % h-BN film deposited on (100) boron-doped diamond substrate.

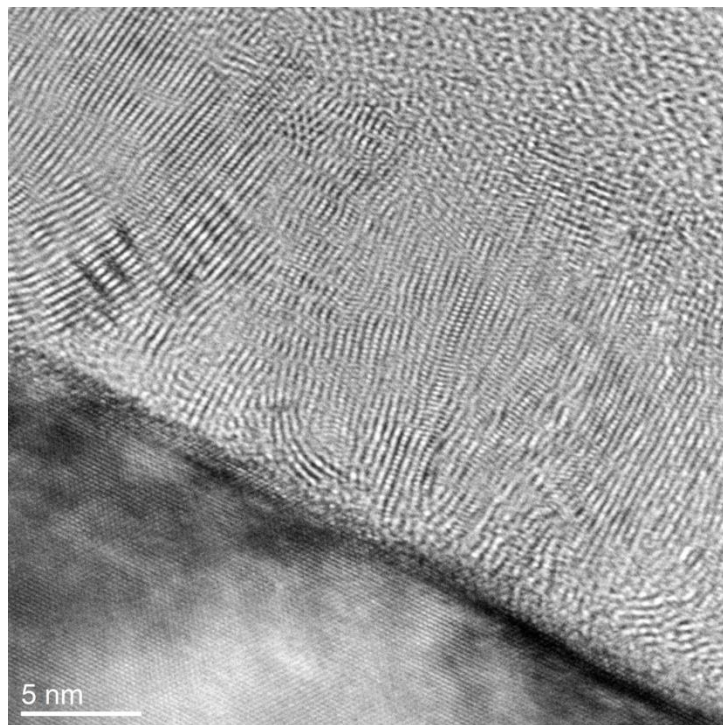


Figure 34 TEM of 14-17 nm thick BN on top of (100) boron-doped diamond surface. The BN layer seems to be in a disordered state of sp^2 often called turbostratic BN.

4.5 Discussion

Cubic BN is known to have an NEA for hydrogen terminated surfaces. [69] The results shown in Figure 28 scan (d) and Figure 29 scan (c) is of a 1.1 nm film consisting of 65 % sp^3 bonding, characteristic of c-BN. The measured VBM is 1.5 eV below the Fermi level and the effective work function is measured to be 4.4 eV above the Fermi level. The band gap of c-BN is 6.4 eV, and the separation of the VBM and effective work function is 5.9 eV. This value is less than the reported bandgap of c-BN and could be consistent with an NEA.

The BN layer shown in Figure 29 scan (d) and scan (e) have ~ 80 % sp^2 bonding and are therefore considered to be h-BN. The indirect band gap of h-BN is 5.2 eV, and the direct band gap is 5.9 eV. The separation between the VBM and work functions in Figure 29 scan (c) and scan (d) are 7.1 eV and 7.3 eV respectively, which is interpreted as a PEA of ~ 2 eV for both BN layers.

The VBO of c-BN deposited on (100) boron-doped diamond via ECR-PECVD is compared with previous experimental and theoretical results. The results of the XPS and UPS measurements of the heterojunction are used to deduce a VBO of -0.3 eV, with the diamond VBM above the c-BN VBM. This result is similar to the theoretical reports of the VBO of c-BN on diamond, with (100) surface orientation and C—N bonding across the interface (-0.13 eV). This is reasonable based on the initial nitrogen-terminated surface. Previous experimental results by [Shammas et al.] showed c-BN deposited on polycrystalline nitrogen-doped diamond with a VBO of +0.8 eV. Here the diamond VBM was below the c-BN VBM. This result is similar to the theoretical report of the VBO of c-

BN on diamond with (111) surface orientation and C—N bonding across the interface (+0.59 eV).

Orientation	Calculated VBO		Experimental VBO	Band Bending	
	C—B Interface	C—N Interface		Boron-Doped Diamond (Bulk VBM ~0.3 eV)	Nitrogen-Doped Diamond (Bulk VBM ~3.9 eV)
(100)	[65] VBO = -2.0 Dia VBM c-BN VBM	[65] VBO = -0.13 Dia VBM c-BN VBM	[This Work] VBO = -0.3 Dia VBM c-BN VBM	[32] H-Terminated Surface VBM = 0.6 	[32] H-Terminated Surface VBM = 2.2
(111)	[64] VBO = -0.05 Dia VBM c-BN VBM	[64] VBO = +0.59 Dia VBM c-BN VBM	[49] VBO = +0.8 Dia VBM c-BN VBM		
(110)	[62] VBO = -1.4 Dia VBM c-BN VBM				

Table 3 Previous reports of VBO between c-BN and Diamond. For different interface orientations (100), (111), and (110), there are different interface bonds possible. For (100), and (111) there can be either C—N or C—B, while for (110), there is both C—N and C—B at the interface. The diamond VBM is the reference point, and positive VBO is for c-BN VBM closer to the fermi level than the diamond VBM. Negative VBO is for c-BN VBM greater than diamond

The energy separation between the diamond C 1s and VBM should be a constant value for the same chemical state (Const. = $\Delta E = C\ 1s - VBM$). The previous experimental reports by [Shammas] measured $\Delta E = 283.3 \pm 0.1$ eV. However, the results presented in this article are measured $\Delta E = 283.7 \pm 0.2$. The larger error for the results presented in this paper are due to variations in the surface after processing that resulted in a range of VBM's (0.7 – 0.3 eV). The previous reported error of 0.1 is from instrument resolution, not from multiple measurements. Since ΔE should be a constant regardless of doping, if the average between these two is calculated and the error is increased accordingly the following two VBO's are calculated for the (100) boron-doped substrate:

$$\Delta E_V = -0.1 \pm 0.3 = (94.4 \pm 0.2) + (189.0 \pm 0.2)_{c-BN} - (283.5 \pm 0.3)_{Diamond}$$

And the polycrystalline nitrogen-doped substrate:

$$\Delta E_V = +0.6 \pm 0.3 = (95.1 \pm 0.2) + (189.0 \pm 0.2)_{c-BN} - (283.5 \pm 0.3)_{Diamond}$$

Using the averaged ΔE between the two measurements for diamond, the VBO's of the different measurements become closer to the theoretical values.

To be of use in the design of heterojunction devices a band offset must typically be known to an accuracy of ~ 0.1 eV or better. [59] Therefore, the associated errors in these measurements should be more accurately determined to be widely applicable for device design and simulation. To achieve an error of 0.1 eV or better for ΔE_V the error for XPS core level peak center needs to be 50 meV, and the VBM for the substrate and the thick c-BN film needs to be known to an accuracy of 30 meV or better. Each of the terms to the right-hand side of Equation 13 should have an uncertainty of less than 0.06

eV. According to Figure 8, using the VG Scientia R3000 analyzer, either a pass energy of 100 eV with a slit size of 0.2 mm or a pass energy of 50 eV with a slit size of 0.4 eV should be used to measure the XPS core levels to achieve this level of certainty. A pass energy of 50 eV with a slit size of 0.2 eV exceed the required uncertainty.

Increasing the precision of the XPS measurements will be important for determining the VBO with increased accuracy. Even more important is developing consistent repeatable, and reliable deposition processes. The largest error in the measurements for the VBO of c-BN on boron-doped diamond is the VBM of the boron doped diamond. Developing a process that can produce nearly identical VBM's across multiple diamond samples is one of the key points for reducing the uncertainty in the VBO measurements. Reproducible thick c-BN films will also be necessary to measure the core level to VBM separation with greater precision. Precise VBO's will enable accurate device designs that include c-BN/diamond heterojunctions.

4.6 Conclusion

In summary, the nucleation of epitaxial c-BN on 5° offcut (100) boron-doped diamond via ECR-PECVD was achieved. XPS and TEM images from this sample show that the nucleation was able to occur without evident interfacial h-BN. Unintentional silicon impurities were thought to be responsible for the disordered structures observed in TEM for the thicker h-BN films. The VBO of the 1.1 nm c-BN on (100) boron-doped diamond was measured to be -0.3 ± 0.24 eV, where the diamond VBM is above the c-BN VBM. The measured VBO is consistent with the theoretical VBO of the (100) surface with C—N interface bonding. Further studies, with accuracies of 0.1 eV or better for the

VBO of the diamond/c-BN interface on both (100) and (111) surface orientations with both boron-doping and nitrogen-doping would provide insight for potential applications of the diamond/c-BN heterojunction.

5 ELECTRONIC SURFACE STATES OF PHOSPHORUS-DOPED DIAMOND

5.1 Abstract

Phosphorus-doped diamond is an n-type ultra-wide bandgap semiconductor. It is key to the development of diamond for power electronics. Device performance is often sensitive to the surface termination of the phosphorus-doped diamond. Data presented in this chapter focuses on how the phosphorus-doped diamond electronic surface states are altered by two different hydrogen plasma processing procedures. In-situ XPS and UPS are used to measure the diamond C 1s core level energy, and the valence band spectra. The two hydrogen plasma procedures differ only in how the sample is cooled from 750°C to ambient temperature. One process cools the sample in vacuum after the hydrogen plasma. The other process cools the sample in the hydrogen plasma. The results presented indicate the phosphorus-doped diamond VBM is ~ 1.8 eV below the Fermi level when cooled in the vacuum. When the sample is cooled in the plasma, three C 1s core level peaks are clearly resolved, and the corresponding phosphorus-doped diamond VBM is ~ 3.4 eV, 4.8 eV, and 6.1 eV below the Fermi level. Surface state pinning is discussed to model the various diamond VBM's.

5.2 Introduction

Diamond as a wide band gap (5.5 eV) semiconductor is considered an ideal material for high power and high frequency power electronics, due to the high thermal conductivity, high carrier mobility and high breakdown electric field which are needed for these types of devices. While doping diamond p-type with boron has been well established, doping diamond n-type with phosphorus was first demonstrated in 1997 [70].

Phosphorus doped diamond is key to implement diamond in electronics, UV optoelectronic, and vacuum electronic applications.

In current silicon device technologies, surface preparation is an important aspect of device fabrication, and it is certainly key for the fabrication of diamond devices. Hydrogen terminated diamond is known to have a negative electron affinity (NEA), where the conduction band minimum is above the vacuum energy level. The NEA has been observed for both (100) and (111) surfaces, and for both boron-doped and phosphorus-doped diamond. In contrast, oxygen, or fluorine terminated diamond and reconstructed diamond surfaces have a positive electron affinity (PEA) surface. The surface termination of diamond can change the electron affinity from NEA to positive electron affinity (PEA) across a 4.5 eV range. [71], [72] Consequently, it has been proposed that controlled surface termination can affect the energy band alignment of a semiconductor heterojunction or metal-semiconductor Schottky barrier.

The phosphorus doped diamond metal junction model is of particular interest in one of the core components for diamond electronics; namely the P-I-N structure. The diamond PIN structure includes an intrinsic diamond layer (i-layer) in juxtaposition with a boron-doped layer (p-type), and a phosphorus-doped layer (n-type). Boron-doped diamond/metal interfaces have been well studied. The relative novelty of phosphorus doped diamond has created a need for more research on the junction of n-type phosphorus-doped diamond with metal contacts.

Surface preparation of the phosphorous-doped layer can affect the energy band alignment with metal contacts. Surface state pinning confines the Schottky barrier to a

small range of values over a large range of different metal work functions. However, if the interface alignment mechanism is dominated by vacuum level alignment, the semiconductor metal interface barrier height could be tuned based on the choice of metal. Controlled surface termination could allow selection of Ohmic band alignment or Schottky barrier. The vacuum level alignment is particularly of interest for the employment of NEA surfaces. Energy band alignment between the n-type phosphorus-doped diamond and metal contact is key for device design and modeling. Therefore, determining surface preparation methods that result surface state pinning or unpinning is of important.

A diamond surface state, positioned ~ 1.8 eV below the Fermi level has been reported for phosphorus doped diamond. The hydrogen terminated phosphorus-doped diamond surface is pinned to this surface state and ~ 3 eV of upward band bending has been observed. [73] Alternatively, downward band bending has been observed for the reconstructed surface of phosphorus-doped diamond [74]. The research in this report is focused on measuring the carbon core levels with XPS, the valence band and vacuum level positions using UPS. Analysis of the XPS/UPS spectra is used to understand how surface preparation modifies the diamond electronic surface state properties,

5.3 Experiment

A homoepitaxial P-doped diamond layer ~ 5 μm thick with a doping concentration of $[\text{P}] \sim 1\text{-}5\text{E}^{19}$ (cm^{-3}) was deposited on a single crystal (111) intrinsic diamond substrate from EDP corp. A 5° offcut (100) boron-doped diamond sample with a boron concentration of $\sim 1\text{-}2\text{E}^{20}$ (cm^{-3}) supplied by TISNCM was used for comparison. The

diamond samples were independently secured to a 25.4 mm diameter nichrome mounting plate with tantalum wires. Each sample was loaded into an integrated vacuum system, where samples can be transferred between process chambers and characterization chambers without exposure to atmosphere.

An electron cyclotron plasma enhanced chemical vapor deposition (ECR PECVD) system was used to expose the diamond surface to a hydrogen plasma. The ECR PECVD chamber has a base pressure of 3×10^{-9} Torr. The sample was heated to $\sim 750^\circ\text{C}$ using a toroidal tungsten filament that radiatively heats the sample. Hydrogen gas flow of 20 sccm was input into the chamber at a pressure of 2×10^{-4} Torr. The plasma was sustained for 10 minutes using a microwave power of 300W. This is the standard process described in Chapter 3 and 4 as well. Since the ECR PECVD process is a remote plasma, the plasma does not heat the sample.

Up to this point in the procedure the processes on all samples have been identical. Two processes are investigated that only differ in how the sample was cooled to ambient temperature (Figure 35). For **process A** the diamond was **cooled in vacuum**, while **process B** the diamond was **cooled in the plasma**. Both cool down times were approximately 7-9 minutes. By cooling in vacuum the surface is quenched, which is thought to prevent any further surface modifications. Alternatively, cooling in the plasma may allow surface modifications to occur during the cool down process.

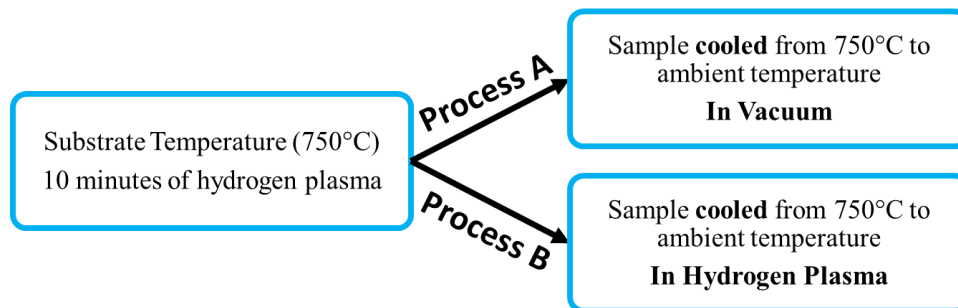


Figure 35 Experimental flow diagram showing the difference between process A and process B.

After each process the diamond sample was transferred in-situ to the XPS/UPS chamber, with base pressure 5×10^{-10} Torr. X-rays generated by an Al-K α source with monochromator have an energy of 1486.6 eV with a bandwidth of 0.2 eV. A hemispherical analyzer, operated in sweep mode, with a pass energy of 100 eV, a resolution of 150 meV, and energy step size of 100 meV was used to scan the diamond core energy levels.

In the same chamber, ultra-violet light for UPS was generated by a helium discharge lamp. The photons have energies of 21.2 eV, 23.1 eV, 40.8 eV, and 48.3 eV. The He I α line (21.2 eV) is used to measure the work function of the surface. The He II α line (40.8 eV) is used to measure the valence band spectrum. The hemispherical analyzer is operated in sweep mode, with a pass energy of 2 eV, with an energy resolution of less than 10 meV, and an energy step size of 20 meV. A bias of 1.5 eV is applied to the sample and an energy offset of 2.7 eV is applied to overcome the analyzer work function (~ 4.2 eV), and align the Fermi level of a gold reference sample to zero binding energy.

By using both He I α and He II α , the relative position of the vacuum level to the valence band maximum is deduced. The electron affinity is then calculated to infer a NEA or PEA.

5.4 Results

The phosphorus-doped diamond is exposed to the ECR-PECVD hydrogen plasma then, either cooled down in vacuum (process **A**) or cooled down in the plasma (process **B**). The resulting XPS and UPS scans are combined are shown in Figure 36 scan (b) and scan (c) respectively. For comparison, a (100) boron doped diamond, which followed an identical procedure as process **A** is presented in Figure 36 scan (a). The hydrogen terminated boron-doped diamond has an energy difference between the C 1s core level and VBM of $\Delta E = 283.9$ eV. The He I α spectra has two distinct cut offs, one at 5.3 eV and the other at 4.3 eV above the Fermi level. This is the distinct characteristics of the boron-doped diamond NEA surface. The vacuum level is thought to be positioned near the 4.3 eV feature, while the sharp cutoff at 5.3 eV is thought to be the CBM. The separation between the CBM at 5.3 eV and the VBM of 0.3 eV is approximately equal to the band gap (5.5 eV), which is another distinct characteristic of NEA surfaces.

The phosphorus doped diamond with process **A** has a C 1s core level of 285.7 eV. The VBM is difficult to confidently deduce using the linear fit method. However, by using the ΔE of the boron-doped diamond, the VBM of the phosphorus-doped diamond can be estimated to be approximately 1.8 eV below the Fermi level. The work function cut off is located at 3.9 eV above the Fermi level. While there is some uncertainty, the work

function and VBM values indicate that the vacuum level is 0.2 eV above the CBM. Which could indicate a small positive electron affinity.

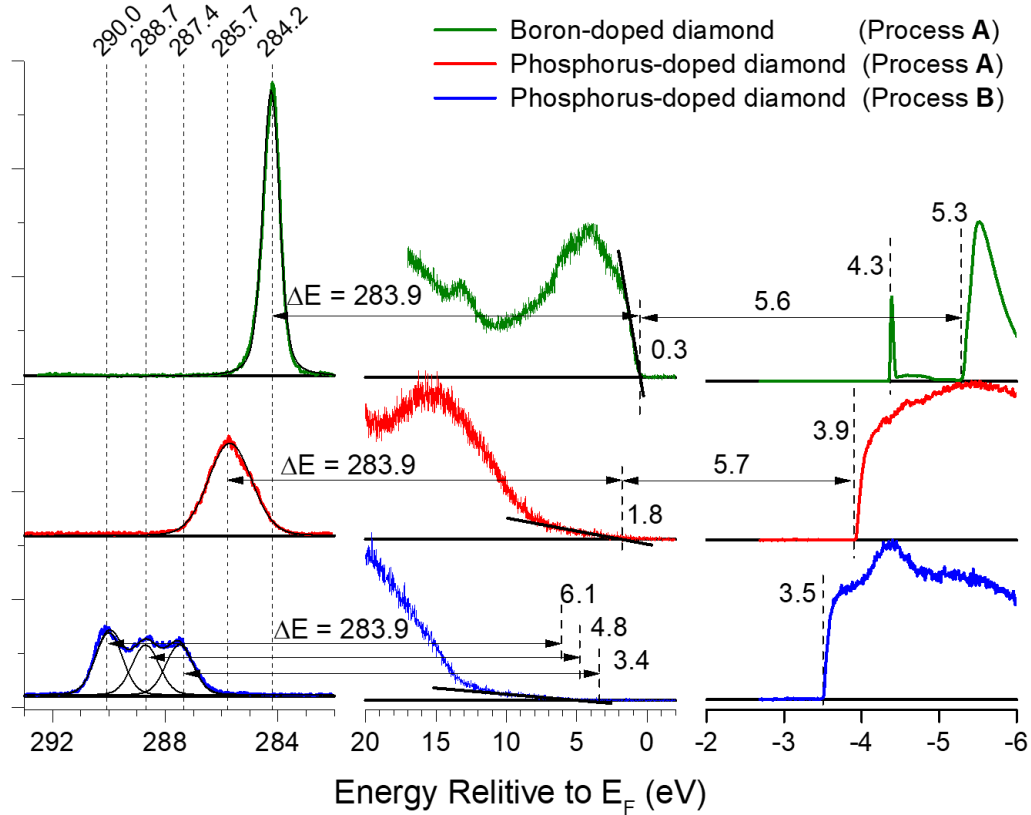


Figure 36 XPS and UPS of top: (a) hydrogen-terminated boron-doped diamond, middle: (b) hydrogen-terminated phosphorus-doped diamond, bottom: (c) modified surface of phosphorus-doped diamond

The phosphorus doped diamond with process **B** displays an interesting C 1s core level spectrum. The C 1s core level spectrum has three distinct peaks at 287.4 eV, 288.7 eV, and 290.0 eV. Using the core level energies and $\Delta E = 283.9$ eV, indicates a VBM at 3.4 eV, 4.8 eV, and 6.1 eV respectively. The He II spectrum for process **B** is slightly more conclusive as to the position of the VBM at 4.9 eV below the Fermi level using the

linear fit method. The linear fit VBM is within the range of VBM according to the energy difference of $\Delta E = 283.9$ eV with C 1s core level. A work function of 3.5 eV above the Fermi level was deduced from the He I spectra for process **B**. Combining the work function and VBM (4.8 eV) values indicate the vacuum level is 2.8 eV above the CBM.

5.5 Discussion

The phosphorus-doped diamond with process **A**, has a C 1s core energy of 285.7 eV, which is similar to the C 1s core level position for H-terminated nitrogen-doped diamond (286.2 eV) [Diedirich]. The H-terminated nitrogen-doped diamond is reported to have a VBM of 2.2 eV. The reported boron-doped diamond C 1s core level and diamond VBM difference is $\Delta E(\text{B-doped}) = 283.4$ eV, and the nitrogen-doped diamond C 1s core level and diamond VBM difference is $\Delta E(\text{N-doped}) = 284.0$ eV. which is close to our value for $\Delta E(\text{P-doped}) = 283.9$ eV.

There is a distinct difference in the photoelectron spectrum for the phosphorus-doped diamond surface prepared using process **A** and **B**. Which only differ in how the sample was cooled to ambient temperature, either in vacuum, or in a plasma. Cooling in the vacuum (process **A**) is thought to leave the surface hydrogen terminated. The hydrogen termination of phosphorus-doped diamond is thought to exhibit surface state pinning at 1.8 eV, causing upward band bending in the P-doped diamond. [73] Hydrogen terminated boron-doped diamond is thought to exhibit downward band bending due to the pinning by the same surface state.

Process **B**, which is cooled in the plasma has a range of possible VBM's but all of which are greater than the mid-gap of diamond (2.75 eV) which indicates this surface has n-type characteristics. This is unusual, as even for nitrogen-doped diamond, which is n-type, is known to have a surface VBM of ~1.3-2.5 eV for hydrogen termination or reconstructed surface [32] [66] The bulk VBM of phosphorus-doped diamond is ~ 4.8 eV below the Fermi level. Therefore, a surface VBM of 3.4 eV implies a relatively small amount of upward band bending (~1.4 eV of band bending), flat bands (VBM = 4.8 eV), or even downward band bending (VBM = 6.1 eV). A VBM of 6.1 eV would put the CBM below the Fermi level since the band gap of diamond is 5.5 eV.

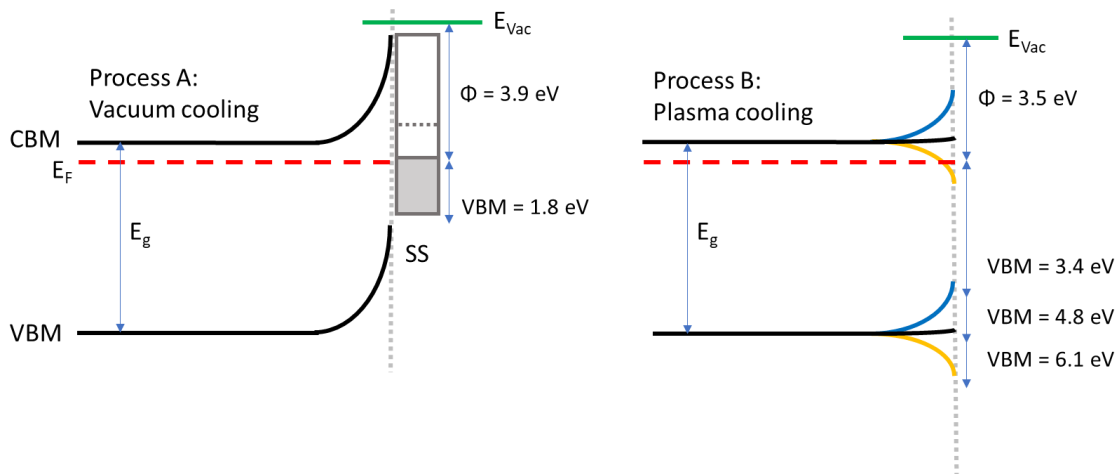


Figure 37 Band alignment diagram for P-doped diamond for Process A (left) showing the surface state pinning causing the upward band bending. For process B (right) the triple core level, and subsequent triple VBM are shown in different colors. The VBM ranges from upward band bending to flat bands, to downward band bending depending on which peak the VBM is deduced from.

5.6 Conclusion

The electronic surface states of (111) phosphorus doped diamond after two separate surface preparation methods were studied via in-situ XPS and UPS. The hydrogen termination was observed when the samples were cooled down to ambient temperature in a vacuum. Surface state pinning at 1.8 eV was observed after this surface preparation method. When the phosphorus-doped diamond sample was cooled to ambient temperature in a ECR PECVD hydrogen plasma, the surface VBM of 3.4 eV, 4.8 eV or 6.1 eV was measured using the C 1s core level peaks. Using the linear fit method of the He II α valence band spectra, the VBM was determined to be approximately 4.8 eV. These VBM values display n-type characteristics. These two surface preparation methods may have applications in diamond device design and engineering of the diamond metal interface.

6 SUMMARY AND FUTURE WORK

The research presented in this dissertation focused on the nucleation and growth of cubic boron nitride on boron doped diamond. Freestanding polycrystalline boron-doped substrates are used to study the surface chemistry during the nucleation and growth of boron nitride. Results presented in Chapter 3 focus on the role hydrogen plays during ECR-PECVD deposition of boron nitride. In-situ photoelectron spectroscopy (PES) was used to characterize the thickness and ratio of sp^2/sp^3 bonding of the deposited boron nitride films. PES results show that the concentration of hydrogen can control the growth rate, and the sp^2/sp^3 bonding of the BN film.

Increasing the hydrogen concentration increases the growth rate and decreasing the hydrogen concentration decreases the growth rate. When hydrogen is the limiting reactant, c-BN nucleation and growth is more favorable. For example, an excess of hydrogen is more favorable to the growth of h-BN.

Future studies address questions related to the effects of hydrogen flow further. Most notably, can limited H_2 flow be used for the c-BN nucleation, then increase the H_2 flow to increase the growth rate to produce thicker c-BN films? Another question that would be useful for device fabrication processes is: by optimizing the surface chemistry, favorable for c-BN nucleation and growth, can the substrate temperature be reduced?

The tuning of the hydrogen concentration to control the BN film growth rate was particularly useful for the fabrication of a diamond PIN neutron detector with a boron nitride neutron conversion layer [41]. For example, a 0.5-1 μ m thick BN layer was deposited on a PIN diamond structure which provided a sufficiently large neutron

conversion volume. The sp^2/sp^3 ratio was less important for the neutron conversion layer. Consequently, a thick BN layer was grown by increasing the hydrogen flow to 20 sccm. This level of excess hydrogen produced a majority h-BN in the film and a high growth rate of ~ 4 nm/min. Conversely the results presented in Chapter 4 explore using the limited hydrogen flow, in an attempt to obtain an ideal c-BN/diamond interface. The limited hydrogen reaction growth rate (~ 0.03 nm/min) was used to measure the valence band offset (VBO) of the c-BN/boron-doped diamond interface.

Free standing single crystal 5° offcut (100) boron-doped diamond substrates were used to measure the VBO of the c-BN/boron-doped diamond interface. The VBO was determined to be -0.3 ± 0.24 eV for a 1.1 nm thick c-BN epitaxial layer on the (100) boron-doped diamond surface. This agrees with theoretical calculations for the (100) c-BN/diamond junction with C—N bonding at the interface. The results presented in this dissertation are compared with previous experimental reports of c-BN/diamond VBO measurements [49]. A consistency between both experimental results and theory is discussed. The conclusions and new hypothesis made are that the interface orientation is more influential to the VBO than the doping of the diamond substrate.

Future research on the valence band offset of the c-BN/diamond heterojunction should focus on the various surface orientations of doped diamond. To form a robust and thorough investigation of band alignment of the c-BN/diamond the following single crystal substrates should be used to deposit c-BN: (111) boron-doped diamond, (111) nitrogen-doped diamond, and (111) phosphorus-doped diamond epitaxial layer (since freestanding phosphorus-doped diamond is not yet available). Additionally, (100)

nitrogen-doped diamond and (100) phosphorus-doped diamond, as well as repeating the (100) boron-doped diamond results presented in this dissertation.

For greater confidence in the c-BN/diamond band alignment measurement, multiple nearly identical diamond substrates and c-BN films should be carefully studied to form a statistical basis of the error of the VBO. This will also give insight into possible variations on the surface preparation of the diamond, and the variations in the growth of c-BN. The results should establish if the doping or crystal face has a larger effect on the VBO.

It should be noted that unintentional incorporation of silicon during the deposition of BN may cause disorder in the film and prevent the formation of c-BN at the interface. Reducing the amount of silicon in the growth chamber may improve future deposition efforts. The main concern is the quartz microwave window near the ECR plasma zone. A material that is inert to fluorine etching, like c-BN, would be an ideal coating on the quartz window.

To fully realize c-BN as an ultra-wide bandgap semiconductor the c-BN/metal interface energy alignment will be key. Characterization of the c-BN/metal Schottky barrier of various metals would ideally be performed using an integrated vacuum transfer line like the one employed in this dissertation. Currently, diamond Schottky diodes can be used as an alpha particle detector. Also as mentioned previously, boron nitride acted as a neutron to alpha particle converter for a diamond NIP neutron detector. Consider instead, a boron-doped diamond substrate with a thick heteroepitaxial layer of c-BN ($> 1 \mu\text{m}$), and a Schottky metal contact on top. This structure would combine the neutron to

alpha conversion layer with the active detector region. Creating a Schottky barrier at the c-BN/metal interface will create a built-in electric field, like what is observed in diamond, which would allow for lower operating voltages.

The current neutron detector structure (BN/metal/NIP diamond/metal), [41] requires the alpha particles generated in the BN layer to cross the metal and n-type diamond layer before the energy of the alpha is collected in the intrinsic diamond layer. By converting the neutron to an alpha particle and collecting the energy from the alpha particle in the same material more alpha particles would be detected due to the geometry of the detector. Also, the thicker layer of BN will increase the number of neutrons converted to alphas. These two features will increase the efficiency of the c-BN Schottky diode neutron detector relative to the current neutron detector structure.

The surface preparation processes for phosphorus-doped diamond were studied using in-situ photoelectron spectroscopy. An epitaxial (111) phosphorus-doped diamond sample were heated to 750°C in vacuum and exposed to an ECR-PECVD hydrogen plasma process for 10 minutes. The sample was then cooled to ambient temperature either in a vacuum, or in the hydrogen plasma. After the sample was cooled in the vacuum a single C 1s core level peak at 285.7 eV is observed. The diamond VBM was measured to be 1.8 eV below the fermi level when cooled in the vacuum. This is thought to be due to surface state pinning the Fermi level. Conversely, after the sample was cooled in the plasma, the C 1s core level split into three distinct peaks, separated by ~1.3eV. Consequently, three distinct VBM's of 3.4 eV, 4.8 eV, and 6.1 eV are deduced based on the separation of the core level and the VBM being a constant. The diamond

VBM was measured to be 4.8 eV below the Fermi level using UPS. This was a surprising result and is not fully understood at this time. One possible explanation for the multiple C 1s peaks could be a non-uniform surface termination. The downward band bending for the VBM at 6.1 eV could be due to Fermi level pinning to the normally unoccupied surface states.

Future studies on the surface preparation process of phosphorus doped diamond would be greatly enhanced by the employment of a Monochromatic UV source, and Angle resolved UPS of the suspected surface states. The R3000 hemispherical analyzer is capable of mapping the energy dispersion of the surface states. The calibration and optimized operation of the angle resolved mode of the analyzer, along with the rotation of the sample to vary the probe depth may provide conclusive evidence for the analysis of the surface states of the diamond and cubic boron nitride surfaces. In-situ photoemission is extremely important to preserve the as-prepared surfaces of interest and has been absolutely critical in the characterization of boron nitride and semiconducting diamond interfaces and surface states.

REFERENCES

- [1] A. A. Giardini, Boron Nitride, United States Department of the Interior, 1953.
- [2] L. F. Dobrzhinetskaya, R. Wirth, J. Yang, H. W. Green, I. D. Hutcheon, P. K. Weber and E. S. Grew, "Qingsongite, natural cubic boron nitride: The first boron mineral from the Earth's mantle," *American Mineralogist*, vol. 99, p. 764–772, 2014.
- [3] R. H. Wentorf, "Cubic Form of Boron Nitride," *The Journal of Chemical Physics*, vol. 26, p. 956–956, April 1957.
- [4] R. H. Wentorf, "Preparation of Semiconducting Cubic Boron Nitride," vol. 36, p. 1990, 1962.
- [5] M. J. Rand and J. F. Roberts, "Preparation and Properties of Thin Film Boron Nitride," *Journal of The Electrochemical Society*, vol. 115, p. 423, 1968.
- [6] W. Baronian, "The optical properties of thin boron nitride films," *Materials Research Bulletin*, vol. 7, p. 119–124, 1972.
- [7] R. M. Chrenko, "Ultraviolet and infrared spectra of cubic boron nitride," *Solid State Communications*, vol. 14, p. 511–515, March 1974.
- [8] J.-C. Zheng, L. Zhang, A. V. Kretinin, S. V. Morozov, Y. B. Wang, T. Wang, X. Li, F. Ren, J. Zhang, C.-Y. Lu, J.-C. Chen, M. Lu, H.-Q. Wang, A. K. Geim and K. S. Novoselov, "High thermal conductivity of hexagonal boron nitride laminates," *2D Materials*, vol. 3, p. 011004, January 2016.
- [9] K. Chen, B. Song, N. K. Ravichandran, Q. Zheng, X. Chen, H. Lee, H. Sun, S. Li, G. A. G. Udalamatta Gamage, F. Tian, Z. Ding, Q. Song, A. Rai, H. Wu, P. Koirala, A. J. Schmidt, K. Watanabe, B. Lv, Z. Ren, L. Shi, D. G. Cahill, T. Taniguchi, D. Broido and G. Chen, "Ultra-high thermal conductivity in isotope-enriched cubic boron nitride," *Science*, vol. 367, p. 555–559, January 2020.
- [10] J. R. Olson and R. O. Pohl, "Thermal conductivity of diamond between 170 and 1200 K and the isotope effect," *AND*. . . , p. 7.
- [11] N. García, P. Esquinazi, J. Barzola-Quiquia and S. Dusari, "Evidence for semiconducting behavior with a narrow band gap of Bernal graphite," *New Journal of Physics*, vol. 14, p. 053015, May 2012.

- [12] Y. Hattori, T. Taniguchi, K. Watanabe and K. Nagashio, "Layer-by-Layer Dielectric Breakdown of Hexagonal Boron Nitride," *ACS Nano*, vol. 9, p. 916–921, January 2015.
- [13] D. M. Goebel, "High Voltage Breakdown Limits of Molybdenum and Carbon-based Grids for Ion Thrusters," p. 17.
- [14] T. Taniguchi and S. Yamaoka, "Spontaneous nucleation of cubic boron nitride single crystal by temperature gradient method under high pressure," *Journal of Crystal Growth*, vol. 222, p. 549–557, 2001.
- [15] M. Lv, B. Xu, L. Cai, X. Guo and X. Yuan, "Auger electron spectroscopy analysis for growth interface of cubic boron nitride single crystals synthesized under high pressure and high temperature," *Applied Surface Science*, vol. 439, p. 780–783, May 2018.
- [16] O. Mishima, J. Tanaka, S. Yamaoka and O. Fukunaga, "High-Temperature Cubic Boron Nitride P-N Junction Diode Made at High Pressure," *Science*, vol. 238, p. 181–183, October 1987.
- [17] W. J. Zhang, Y. M. Chong, I. Bello and S. T. Lee, "Nucleation, growth and characterization of cubic boron nitride (cBN) films," *Journal of Physics D: Applied Physics*, vol. 40, p. 6159–6174, October 2007.
- [18] K. Hirama, Y. Taniyasu, H. Yamamoto and K. Kumakura, "Structural analysis of cubic boron nitride (111) films heteroepitaxially grown on diamond (111) substrates," *Journal of Applied Physics*, vol. 125, p. 115303, 2019.
- [19] S. P. S. Arya and A. D'Amico, "Preparation, properties and applications of boron nitride thin films," *Thin Solid Films*, vol. 157, p. 267–282, 1988.
- [20] I. Konyashin, B. Joachim and F. Aldinger, "Plasma-Assisted CVD of Cubic Boron Nitride," p. 17, 1997.
- [21] W. J. Zhang, C. Y. Chan, X. M. Meng, M. K. Fung, I. Bello, Y. Lifshitz, S. T. Lee and X. Jiang, "The Mechanism of Chemical Vapor Deposition of Cubic Boron Nitride Films from Fluorine-Containing Species," *Angewandte Chemie International Edition*, vol. 44, p. 4749–4753, July 2005.
- [22] C. Chan, W. J. Zhang, X. M. Meng, K. M. Chan, I. Bello, Y. Lifshitz and S. T. Lee, "The growth of thick cBN films employing fluorine chemistry and ECR deposition," *Diamond and Related Materials*, vol. 12, p. 1162–1168, July 2003.

- [23] W. J. Zhang and S. Matsumoto, "The roles of hydrogen and fluorine in the deposition of cBN films with the Ar\N2\BF3\H2 system," *Chemical Physics Letters*, 2000.
- [24] J. Shammass, "Characterization of Cubic Boron Nitride Interfaces with in situ Photoelectron Spectroscopy," p. 150, April 2016.
- [25] W. E. Spicer, "Photoemissive, Photoconductive, and Optical Absorption Studies of Alkali-Antimony Compounds," *Physical Review*, vol. 112, p. 114–122, October 1958.
- [26] F. A. Stevie and C. L. Donley, "Introduction to x-ray photoelectron spectroscopy," *Journal of Vacuum Science & Technology A*, vol. 38, p. 063204, December 2020.
- [27] A. Jablonski and J. Zemek, "Overlayer thickness determination by XPS using the multiline approach: Overlayer thickness determination by XPS using the multiline approach," *Surface and Interface Analysis*, vol. 41, p. 193–204, March 2009.
- [28] C. D. Wagner, L. E. Davis, M. V. Zeller, J. A. Taylor, R. H. Raymond and L. H. Gale, "Empirical atomic sensitivity factors for quantitative analysis by electron spectroscopy for chemical analysis," *Surface and Interface Analysis*, vol. 3, p. 211–225, October 1981.
- [29] A. Alanazi, "Ultraviolet Light Generation from a Helium Plasma as a Function of Radio Frequency Power and Gas Pressure," 2017.
- [30] T. Barr, *Modern ESCA: The Principles and Practice of X-Ray Photoelectron Spectroscopy*, CRC press, 1994.
- [31] Z. Zhang and J. T. Yates, "Band Bending in Semiconductors: Chemical and Physical Consequences at Surfaces and Interfaces," *Chemical Reviews*, vol. 112, p. 5520–5551, October 2012.
- [32] L. Diederich, O. M. Küttel, P. Ruffieux, T. Pillo, P. Aebi and L. Schlapbach, "Photoelectron emission from nitrogen- and boron-doped diamond (100) surfaces," *Surface Science*, vol. 417, p. 41–52, November 1998.
- [33] E. A. Kraut, R. W. Grant, J. R. Waldrop and S. P. Kowalczyk, "Semiconductor core-level to valence-band maximum binding-energy differences: Precise determination by x-ray photoelectron spectroscopy," *Physical Review B*, vol. 28, p. 1965–1977, August 1983.
- [34] W. Zhang, Y. M. Chong, B. He, I. Bello and S.-T. Lee, "Cubic Boron Nitride Films," in *Comprehensive Hard Materials*, Elsevier, 2014, p. 607–639.

- [35] X. Zhang and J. Meng, "Recent progress of boron nitrides," in *Ultra-Wide Bandgap Semiconductor Materials*, Elsevier, 2019, p. 347–419.
- [36] J. Shammass, T. Sun, F. A. M. Koeck, A. Rezikyan and R. J. Nemanich, "In situ photoelectron spectroscopic characterization of c-BN films deposited via plasma enhanced chemical vapor deposition employing fluorine chemistry," *Diamond and Related Materials*, vol. 56, p. 13–22, June 2015.
- [37] Y. Yang, T. Sun, J. Shammass, M. Kaur, M. Hao and R. J. Nemanich, "Electron affinity of cubic boron nitride terminated with vanadium oxide," *Journal of Applied Physics*, vol. 118, p. 165310, October 2015.
- [38] M. J. Powers, M. C. Benjamin, L. M. Porter, R. J. Nemanich, R. F. Davis, J. J. Cuomo, G. L. Doll and S. J. Harris, "Observation of a negative electron affinity for boron nitride," p. 4.
- [39] W. J. Zhang, I. Bello, Y. Lifshitz and S. T. Lee, "Recent Advances in Cubic Boron Nitride Deposition," *MRS Bulletin*, vol. 28, p. 184–188, March 2003.
- [40] Y. Kumashiro, *Electric Refractory Materials*, CRC Press, 2000.
- [41] J. Holmes, J. Brown, F. A. Koeck, H. Johnson, M. K. Benipal, P. Kandlakunta, A. Zaniewski, R. Alarcon, R. Cao, S. M. Goodnick and R. J. Nemanich, "Performance of 5- μ m PIN diamond diodes as thermal neutron detectors," *Nuclear Instruments and Methods in Physics Research Section A: Accelerators, Spectrometers, Detectors and Associated Equipment*, vol. 961, p. 163601, May 2020.
- [42] J. Holmes, M. Dutta, F. A. Koeck, M. Benipal, J. Brown, B. Fox, R. Hathwar, H. Johnson, M. Malakoutian, M. Saremi, A. Zaniewski, R. Alarcon, S. Chowdhury, S. M. Goodnick and R. J. Nemanich, "A 4.5 μ m PIN diamond diode for detecting slow neutrons.pdf," *Nuclear Instruments and Methods in Physics Research Section A: Accelerators, Spectrometers, Detectors and Associated Equipment*, vol. 903, p. 297–301, 2018.
- [43] G. Knoll, "Radiation Detection and Measurement, 3rd ed - Glenn F.pdf," in *Radiation Detection and Measurement, 3rd ed - Glenn F.pdf*, 3rd ed., John Wiley & Sons, Inc., 2000.
- [44] T.-H. Yang, J. Brown, K. Fu, J. Zhou, K. Hatch, C. Yang, J. Montes, X. Qi, H. Fu, R. J. Nemanich and Y. Zhao, "AlGaIn/GaN metal–insulator–semiconductor high electron mobility transistors (MISHEMTs) using plasma deposited BN as gate dielectric," *Applied Physics Letters*, vol. 118, p. 072102, February 2021.

- [45] K. Hirama, Y. Taniyasu, S.-I. Karimoto, Y. Krockenberger and H. Yamamoto, "Single-crystal cubic boron nitride thin films grown by ion-beam-assisted molecular beam epitaxy," *Applied Physics Letters*, vol. 104, p. 092113, 2014.
- [46] W. J. Zhang, I. Bello, Y. Lifshitz, K. M. Chan, Y. Wu, C. Y. Chan, X. M. Meng and S. T. Lee, "Thick and adherent cubic boron nitride films grown on diamond interlayers by fluorine-assisted chemical vapor deposition," *Applied Physics Letters*, vol. 85, p. 1344–1346, August 2004.
- [47] D. Han, X.-B. Li, Y. Y. Sun, S. B. Zhang, S.-Y. Xie, S. Limpijumnong, Z.-G. Chen and H.-B. Sun, "Role of hydrogen in the growth of boron nitride: Cubic phase versus hexagonal phase," *Computational Materials Science*, vol. 82, p. 310–313, February 2014.
- [48] H. Shinotsuka, S. Tanuma, C. J. Powell and D. R. Penn, "Calculations of electron inelastic mean free paths. XII. Data for 42 inorganic compounds over the 50 eV to 200 keV range with the full Penn algorithm," *Surface and Interface Analysis*, vol. 51, p. 427–457, April 2019.
- [49] J. Shammass, Y. Yang, X. Wang, F. A. M. Koeck, M. R. McCartney, D. J. Smith and R. J. Nemanich, "Band offsets of epitaxial cubic boron nitride deposited on polycrystalline diamond via plasma-enhanced chemical vapor deposition," *Applied Physics Letters*, vol. 111, p. 171604, October 2017.
- [50] A. Denisenko, A. Romanyuk, L. A. Kibler and E. Kohn, "Surface structure and electrochemical characteristics of boron-doped diamond exposed to rf N₂-plasma," *Journal of Electroanalytical Chemistry*, vol. 657, p. 164–171, July 2011.
- [51] S. Ghodbane, D. Ballutaud, A. Deneuville and C. Baron, "Influence of boron concentration on the XPS spectra of the (100) surface of homoepitaxial boron-doped diamond films," *physica status solidi (a)*, vol. 203, p. 3147–3151, September 2006.
- [52] M. Attrash, M. K. Kuntumalla and A. Hoffman, "Bonding, structural properties and thermal stability of low damage RF (N₂) plasma treated diamond (100) surfaces studied by XPS, LEED, and TPD," *Surface Science*, vol. 681, p. 95–103, March 2019.
- [53] E. K. Sichel, R. E. Miller, M. S. Abrahams and C. J. Buiocchi, "Heat capacity and thermal conductivity of hexagonal pyrolytic boron nitride," *Physical Review B*, vol. 13, p. 4607–4611, May 1976.
- [54] M. Girolami, L. Criante, F. Di Fonzo, S. Lo Turco, A. Mezzetti, A. Notargiacomo, M. Pea, A. Bellucci, P. Calvani, V. Valentini and D. M. Trucchi, "Graphite

- distributed electrodes for diamond-based photon-enhanced thermionic emission solar cells," *Carbon*, vol. 111, p. 48–53, January 2017.
- [55] E. Alemanno, M. Martino, A. P. Caricato, M. Corrado, C. Pinto, S. Spagnolo, G. Chiodini, R. Perrino and G. Fiore, "Laser induced nano-graphite electrical contacts on synthetic polycrystalline CVD diamond for nuclear radiation detection," *Diamond and Related Materials*, vol. 38, p. 32–35, September 2013.
- [56] K. Watanabe, T. Taniguchi and H. Kanda, "Direct-bandgap properties and evidence for ultraviolet lasing of hexagonal boron nitride single crystal," *Nature Materials*, vol. 3, p. 404–409, June 2004.
- [57] C.-X. Wang, G.-W. Yang, T.-C. Zhang, H.-W. Liu, Y.-H. Han, J.-F. Luo, C.-X. Gao and G.-T. Zou, "High-quality heterojunction between -type diamond single-crystal film and -type cubic boron nitride bulk single crystal," *Applied Physics Letters*, vol. 83, p. 4854–4856, December 2003.
- [58] Y. Sasama, K. Komatsu, S. Moriyama, M. Imura, T. Teraji, K. Watanabe, T. Taniguchi, T. Uchihashi and Y. Takahide, "High-mobility diamond field effect transistor with a monocrystalline h-BN gate dielectric," *APL Materials*, vol. 6, p. 111105, November 2018.
- [59] H. Ehrenreich and D. Turnbull, *Solid state physics: advances in research and applications*, New York: Academic Press, 1992.
- [60] W. E. Pickett and S. C. Erwin, "Electronic structure and band lineups at the diamond/boron nitride and diamond/nickel interfaces," *Superlattices and Microstructures*, vol. 7, p. 335–339, January 1990.
- [61] W. R. L. Lambrecht and B. Segall, "Electronic structure of (diamond C)/(sphalerite BN) (110) interfaces and superlattices," *Physical Review B*, vol. 40, p. 9909–9919, November 1989.
- [62] W. E. Pickett, "Thin superlattices and band-gap discontinuities: The (110) diamond – boron nitride interface," *Physical Review B*, vol. 38, p. 1316–1322, July 1988.
- [63] K. Yamamoto, K. Kobayashi, T. Ando, M. Nishitani-Gamo, R. Souda and I. Sakaguchi, "Electronic structures of the diamond/boron-nitride interface," *Diamond and Related Materials*, vol. 7, p. 1021–1024, July 1998.
- [64] D. Zhao, W. Gao, Y. Li, Y. Zhang and H. Yin, "The electronic properties and band-gap discontinuities at the cubic boron nitride/diamond hetero-interface," *RSC Advances*, vol. 9, p. 8435–8443, 2019.

- [65] H. Guo-min, Z. Yong-mei, W. Ren-zhi and L. Shu-ping, "Stability and electronic structures of the polar diamond/boron-nitride(001) interface," *Solid State Communications*, vol. 118, p. 287–290, May 2001.
- [66] L. Diederich, O. M. Küttel, P. Aebi and L. Schlapbach, "Electron affinity and work function of differently oriented and doped diamond surfaces determined by photoelectron spectroscopy," *Surface Science*, vol. 418, p. 219–239, November 1998.
- [67] M. Gong, Q. Wang, N. Gao and H. Li, "Structural and electronic properties of nitrogen-terminated diamond (100) surfaces," *Diamond and Related Materials*, vol. 120, p. 108601, December 2021.
- [68] J. R. Waldrop, R. W. Grant and E. A. Kraut, "Measurement of GaAs/InP and InAs/InP heterojunction band offsets by x-ray photoemission spectroscopy," *Applied Physics Letters*, vol. 54, p. 1878–1880, May 1989.
- [69] M. J. Powers, M. C. Benjamin, L. M. Porter, R. J. Nemanich, R. F. Davis, J. J. Cuomo, G. L. Doll and S. J. Harris, "Observation of a negative electron affinity for boron nitride," *Applied Physics Letters*, vol. 67, p. 3912–3914, December 1995.
- [70] S. Koizumi, M. Kamo, Y. Sato, H. Ozaki and T. Inuzuka, "Growth and characterization of phosphorous doped {111} homoepitaxial diamond thin films," *Applied Physics Letters*, vol. 71, p. 1065–1067, August 1997.
- [71] J. Barkl, A. M. Zaniewski, F. Koeck and R. J. Nemanich, "Diamond photochemistry with visible light," *Diamond and Related Materials*, vol. 96, p. 195–197, June 2019.
- [72] K. J. Rietwyk, S. L. Wong, L. Cao, K. M. O'Donnell, L. Ley, A. T. S. Wee and C. I. Pakes, "Work function and electron affinity of the fluorine-terminated (100) diamond surface," *Applied Physics Letters*, vol. 102, p. 091604, March 2013.
- [73] S. Kono, K. Mizuochi, G. Takyō, T. Goto, T. Abukawa and T. Aoyama, "Energy Band Diagram of a H-Terminated P-Doped n-Type Diamond (111) Surface," *New Diamond and Frontier Carbon Technology*, vol. 17, p. 12, 2007.
- [74] T. Yamada, K. Somu, C. E. Nebel and S.-i. Shikata, "Effect of vacuum annealing on field emission from heavily phosphorus doped homoepitaxial (111) diamond," *Diamond and Related Materials*, vol. 17, p. 745–748, April 2008.
- [75] R. H. Wentorf, "Synthesis of the Cubic Form of Boron Nitride," *The Journal of Chemical Physics*, vol. 34, p. 809–812, March 1961.

- [76] S. R. Steele and R. J. Briggs, "Layered Media as High Power Microwave Absorbers," 1962.
- [77] H. Saitoh and W. A. Yarbrough, "Growth of cubic boron nitride on diamond particles by microwave plasma enhanced chemical vapor deposition," *Applied Physics Letters*, vol. 58, p. 2482–2484, June 1991.
- [78] P. Popper, "Paper 8: Recent Developments in Engineering Ceramics," *Proceedings of the Institution of Mechanical Engineers, Conference Proceedings*, vol. 180, p. 181–192, 1965.
- [79] H. O. Pierson, "Boron Nitride Composites By Chemical Vapor Deposition," *Journal of Composite Materials*, vol. 9, p. 228–240, 1975.
- [80] R. S. Pease, "An X-ray study of boron nitride," vol. 5, p. 356–361, 1952.
- [81] V. A. Fomichev and M. A. Rumsh, "Investigation of X-ray spectra of hexagonal and cubic boron nitride," *Journal of Physics and Chemistry of Solids*, vol. 29, p. 1015–1024, 1968.
- [82] L. F. Dobrzhinetskaya and S. W. Faryad, "Frontiers of Ultrahigh-Pressure Metamorphism," in *Ultrahigh-Pressure Metamorphism*, Elsevier, 2011, p. 1–39.
- [83] J. Wang, F. Ma and M. Sun, "Graphene, hexagonal boron nitride, and their heterostructures: properties and applications," *RSC Advances*, vol. 7, p. 16801–16822, 2017.
- [84] A. Laturia, M. L. Van De Put and W. G. Vandenberghe, "Dielectric properties of hexagonal boron nitride and transition metal dichalcogenides: from monolayer to bulk," *npj 2D Materials and Applications*, vol. 2, 2018.
- [85] M. Grimsditch, E. S. Zouboulis and A. Polian, "Elastic constants of boron nitride," *Journal of Applied Physics*, vol. 76, p. 832–834, July 1994.
- [86] L. Cai, B. Xu, M. Lv, F. Jia and X. Yuan, "Analysis of Cubic Boron Nitride Single Crystal Defects Growth under High Temperature and High Pressure," *Journal of Chemistry*, vol. 2020, p. 1–6, 2020.
- [87] S. T. Manson, "Atomic Photoelectron Spectroscopy, Part I," in *Advances in Electronics and Electron Physics*, vol. 41, Elsevier, 1976, p. 73–111.
- [88] J. Thomas, N. E. Weston and T. E. O'Connor, "Turbostratic Boron Nitride, Thermal Transformation to Ordered-layer-lattice Boron Nitride," *Journal of the American Chemical Society*, vol. 84, p. 4619–4622, December 1962.

- [89] D. R. Wiff and R. Keown, "Energy Bands in Cubic Boron Nitride," p. 8.
- [90] R. T. Tung and L. Kronik, "Fermi level pinning for zinc-blende semiconductors explained with interface bonds," *Physical Review B*, vol. 103, p. 085301, February 2021.
- [91] K. P. Loh, I. Sakaguchi, M. Nishitani-Gamo, T. Taniguchi and T. Ando, "Negative electron affinity of cubic boron nitride," *Diamond and Related Materials*, vol. 8, p. 781–784, March 1999.
- [92] Z. Lin, X. Peng, C. Huang, T. Fu and Z. Wang, "Atomic structure, electronic properties and generalized stacking fault energy of diamond/c-BN multilayer," *RSC Advances*, vol. 7, p. 29599–29605, 2017.
- [93] C. Chen, Z. Wang, T. Kato, N. Shibata, T. Taniguchi and Y. Ikuhara, "Misfit accommodation mechanism at the heterointerface between diamond and cubic boron nitride," *Nature Communications*, vol. 6, p. 6327, 2015.
- [94] J. Yang, B. S. Eller and R. J. Nemanich, "Surface band bending and band alignment of plasma enhanced atomic layer deposited dielectrics on Ga- and N-face gallium nitride," *Journal of Applied Physics*, vol. 116, p. 123702, September 2014.
- [95] P. Widmayer, P. Ziemann and H.-G. Boyen, "Electron energy loss spectroscopy—An additional tool to characterize thin films of cubic boron nitride," *Diamond and Related Materials*, vol. 7, p. 385–390, February 1998.
- [96] M. Sznajder, N. Hrushka and J. A. Majewski, "Morphology and Stability of the Diamond/BN (001) and (111) Interfaces Based on Ab Initio Studies," *Acta Physica Polonica A*, vol. 130, p. 1220–1223, November 2016.
- [97] Y. Sasama, T. Kageura, K. Komatsu, S. Moriyama, J.-i. Inoue, M. Imura, K. Watanabe, T. Taniguchi, T. Uchihashi and Y. Takahide, "Charge-carrier mobility in hydrogen-terminated diamond field-effect transistors," *Journal of Applied Physics*, vol. 127, p. 185707, May 2020.
- [98] H. Park, G. H. Shin, K. J. Lee and S.-Y. Choi, "Atomic-scale etching of hexagonal boron nitride for device integration based on two-dimensional materials," *Nanoscale*, vol. 10, p. 15205–15212, 2018.
- [99] S. Noor Mohammad, "Electrical characteristics of thin film cubic boron nitride," *Solid-State Electronics*, vol. 46, p. 203–222, February 2002.

- [100] J. Narayan, A. Bhaumik and W. Xu, "Direct conversion of h-BN into c-BN and formation of epitaxial c-BN/diamond heterostructures," *Journal of Applied Physics*, vol. 119, p. 185302, May 2016.
- [101] J. Li, H. Li and H. Yin, "Structural evolution, tunable electronic and magnetic properties of bare and semi-hydrogenated two-dimensional cubic boron nitride nanosheets," *Chemical Physics Letters*, Vols. 610-611, p. 198–203, August 2014.
- [102] E. A. Kraut, R. W. Grant, J. R. Waldrop and S. P. Kowalczyk, "Semiconductor core-level to valence-band maximum binding-energy differences: Precise determination by x-ray photoelectron spectroscopy," *Physical Review B*, vol. 28, p. 1965–1977, August 1983.
- [103] C. Kimura, T. Yamamoto and T. Sugino, "Study on electrical characteristics of metalboron nitridemetal and boron nitridersilicon structures," p. 4, 2001.
- [104] S. K. Jang, J. Youn, Y. J. Song and S. Lee, "Synthesis and Characterization of Hexagonal Boron Nitride as a Gate Dielectric," *Scientific Reports*, vol. 6, p. 30449, July 2016.
- [105] P. D. Esquinazi, C. E. Precker, M. Stiller, T. R. S. Cordeiro, J. Barzola-Quiquia, A. Setzer and W. Böhlmann, "Evidence for room temperature superconductivity at graphite interfaces," *Quantum Studies: Mathematics and Foundations*, vol. 5, p. 41–53, April 2018.
- [106] K. G. Crawford, I. Maini, D. A. Macdonald and D. A. J. Moran, "Surface transfer doping of diamond: A review," *Progress in Surface Science*, vol. 96, p. 100613, February 2021.
- [107] V. N. Brudnyi, A. V. Kosobutsky and N. G. Kolin, "The charge neutrality level and the fermi level pinning in A₃N (BN, AlN, GaN, InN) nitrides," *Russian Physics Journal*, vol. 51, p. 1270–1278, December 2008.
- [108] D. Zhao, Z. Liu, J. Wang, Y. Liang, M. Nauman, J. Fu, Y.-F. Wang, S. Fan, W. Wang and H.-X. Wang, "Fabrication of dual-termination Schottky barrier diode by using oxygen-/fluorine-terminated diamond," *Applied Surface Science*, vol. 457, p. 411–416, November 2018.
- [109] C. Yamaguchi, K. Natsui, S. Iizuka, Y. Tateyama and Y. Einaga, "Electrochemical properties of fluorinated boron-doped diamond electrodes fluorine-containing plasma treatment," *Physical Chemistry Chemical Physics*, vol. 21, p. 13788–13794, 2019.

- [110] T. Yamada, T. Masuzawa, H. Mimura and K. Okano, "Field emission spectroscopy measurements of graphene/n-type diamond heterojunction," *Applied Physics Letters*, vol. 114, p. 231601, June 2019.
- [111] T. Yamada, C. E. Nebel, K. Somu, H. Uetsuka, H. Yamaguchi, Y. Kudo, K. Okano and S.-i. Shikata, "Field emission from surface-modified heavily phosphorus-doped homoepitaxial (111) diamond: Field emission from surface-modified heavily phosphorus-doped (111) diamond," *physica status solidi (a)*, vol. 204, p. 2957–2964, September 2007.
- [112] T. Yamada, T. Masuzawa, H. Mimura and K. Okano, "Electron emission from conduction band of heavily phosphorus doped diamond negative electron affinity surface," *Journal of Physics D: Applied Physics*, vol. 49, p. 045102, February 2016.
- [113] J. van der Weide and R. J. Nemanich, "Argon and hydrogen plasma interactions on diamond (111) surfaces: Electronic states and structure," *Applied Physics Letters*, vol. 62, p. 1878–1880, April 1993.
- [114] P. Strobel, M. Riedel, J. Ristein and L. Ley, "Surface transfer doping of diamond," vol. 430, p. 3, 2004.
- [115] A. Stacey, K. M. O'Donnell, J.-P. Chou, A. Schenk, A. Tadich, N. Dontschuk, J. Cervenka, C. Pakes, A. Gali, A. Hoffman and S. Prawer, "Nitrogen Terminated Diamond," *Advanced Materials Interfaces*, vol. 2, p. 1500079, July 2015.
- [116] W. Shen, S. Shen, S. Liu, H. Li, S. Nie, Y. Pan, Z. Tian and Q. Li, "Binding of hydrogen to phosphorus dopant in phosphorus-doped diamond surfaces: A density functional theory study," *Applied Surface Science*, vol. 471, p. 309–317, March 2019.
- [117] M. C. Salvadori, W. W. R. Araújo, F. S. Teixeira, M. Cattani, A. Pasquarelli, E. M. Oks and I. G. Brown, "Termination of diamond surfaces with hydrogen, oxygen and fluorine using a small, simple plasma gun," *Diamond and Related Materials*, vol. 19, p. 324–328, April 2010.
- [118] B. B. Pate, P. M. Stefan, C. Binns, P. J. Jupiter, M. L. Shek, I. Lindau and W. E. Spicer, "Formation of surface states on the (111) surface of diamond," *Journal of Vacuum Science and Technology*, vol. 19, p. 349–354, September 1981.
- [119] B. B. Pate, W. E. Spicer, T. Ohta and I. Lindau, "Electronic structure of the diamond (111) 1×1 surface: Valence-band structure, band bending, and band gap states," *Journal of Vacuum Science and Technology*, vol. 17, p. 1087–1093, September 1980.

- [120] L. Mayrhofer, G. Moras, N. Mulakaluri, S. Rajagopalan, P. A. Stevens and M. Moseler, "Fluorine-Terminated Diamond Surfaces as Dense Dipole Lattices: The Electrostatic Origin of Polar Hydrophobicity," *Journal of the American Chemical Society*, vol. 138, p. 4018–4028, March 2016.
- [121] T. Masuzawa, Y. Neo, H. Mimura, K. Okano and T. Yamada, "Electron Emission Mechanism of Heavily Phosphorus-Doped Diamond with Oxidized Surface," *physica status solidi (a)*, vol. 216, p. 1801025, April 2019.
- [122] T. Y. Leung, W. F. Man, P. K. Lim, W. C. Chan, F. Gaspari and S. Zukotynski, "Determination of the sp^3/sp^2 ratio of a-C:H by XPS and XAES," *Journal of Non-Crystalline Solids*, vol. 254, p. 156–160, September 1999.
- [123] K. Larsson, "The Combined Influence of Dopant Species and Surface Termination on the Electronic Properties of Diamond Surfaces," *C — Journal of Carbon Research*, vol. 6, p. 22, April 2020.
- [124] S. Kumaragurubaran, T. Yamada and S. Shikata, "Vacuum-annealing induced band bending in phosphorus-doped (111) diamond," *Diamond and Related Materials*, vol. 17, p. 1969–1971, November 2008.
- [125] S. Kumaragurubaran, T. Yamada and S. Shikata, "Annealing effects in H- and O-terminated P-doped diamond (111) surfaces," *Diamond and Related Materials*, vol. 17, p. 472–475, April 2008.
- [126] F. A. Koeck, M. Benipal and R. J. Nemanich, "Electrical contact considerations for diamond electron emission diodes," *Diamond and Related Materials*, vol. 101, p. 107607, January 2020.
- [127] R. Hathwar, M. Dutta, F. A. M. Koeck, R. J. Nemanich, S. Chowdhury and S. M. Goodnick, "Temperature dependent simulation of diamond depleted Schottky PIN diodes," *Journal of Applied Physics*, vol. 119, p. 225703, June 2016.
- [128] A. Freedman, "Halogenation of diamond (100) and (111) surfaces by atomic beams," *Journal of Applied Physics*, vol. 75, p. 3112–3120, March 1994.
- [129] S. Cui and E. L. Hu, "Increased negatively charged nitrogen-vacancy centers in fluorinated diamond," *Applied Physics Letters*, vol. 103, p. 051603, July 2013.
- [130] J. B. Cui, J. Ristein and L. Ley, "Electron Affinity of the Bare and Hydrogen Covered Single Crystal Diamond (111) Surface," *Physical Review Letters*, vol. 81, p. 429–432, July 1998.

- [131] J. B. Cui, R. Graupner, J. Ristein and L. Ley, "Electron affinity and band bending of single crystal diamond (111) surface," *Diamond and Related Materials*, vol. 8, p. 748–753, March 1999.
- [132] C. R. Crowell and G. I. Roberts, "Surface State and Interface Effects on the Capacitance-Voltage Relationship in Schottky Barriers," *Journal of Applied Physics*, vol. 40, p. 3726–3730, August 1969.
- [133] B. Ozpineci, L. M. Tolbert, S. K. Islam and M. Chinthavali, "COMPARISON OF WIDE BANDGAP SEMICONDUCTORS FOR POWER APPLICATIONS," p. 7.
- [134] S. Davison and J. Levine, "Surface States".